

Dissertation
submitted to the
Combined Faculties of the Natural Sciences and Mathematics
of the Ruperto-Carola-University of Heidelberg, Germany
for the degree of
Doctor of Natural Sciences

Put forward by
Giovanna Pedaletti
born in: Fano, Italy
Oral examination: 22nd October, 2009

Very High Energy Emission from Passive Supermassive Black Holes

Referees: Prof. Dr. Stefan J. Wagner

Prof. Dr. John G. Kirk

Abstract

The H.E.S.S. experiment, an array of four Imaging Cherenkov Telescopes, widened the horizon of Very High Energy (VHE) astronomy. Its unprecedented sensitivity is well suited for the study of new classes of expected VHE emitters, such as passive galactic nuclei that are the main focus of the work presented in this thesis. Acceleration of particles up to Ultra High Energies is expected in the magnetosphere of supermassive black holes (SMBH). The radiation losses of these accelerated particles are expected to reach the VHE regime in which H.E.S.S. operates. Predicted fluxes exceed the sensitivity of the array. However, strong photon fields in the surrounding of the acceleration region might absorb the produced radiation. Therefore observations focus on those galactic nuclei that are underluminous at lower photon energies. This work presents data collected by the H.E.S.S. telescopes on the test candidate NGC 1399 and their interpretation. While no detection has been achieved, important constraints can be derived from the obtained upper limits on the maximum energy attainable by the accelerated particles and on the magnetic field strength in the acceleration region. A limit on the magnetic field of $B < 74$ Gauss is given. The limit is model dependent and a scaling of the result with the assumptions is given. This is the tightest empirical constraint to date. Because of the lack of signal from the test candidate, a stacking analysis has been performed on similar sources in three cluster fields. A search for signal from classes of active galactic nuclei has also been made in the same three fields. None of the analyzed samples revealed a significant signal. Also presented are the expectations for the next generation of Cherenkov Telescopes and an outlook on the relativistic effects expected on the VHE emission close to SMBH.

Kurzfassung

Das H.E.S.S. Experiment, eine Anordnung von vier abbildenden atmosphärischen Cherenkov-Teleskopen, erweiterte den Horizont der hochenergetischen Gamma-Astronomie. Seine unerhörte Sensitivität erlaubt neue Klassen von hochenergetischen Strahlungsquellen zu studieren. Die Quellen, die in dieser Doktorarbeit untersucht werden, sind passive supermassereiche Schwarze Löcher (SMBH, Supermassive Black Holes). Man erwartet die Beschleunigung von Teilchen zu ultra-hohen Energien in der Magnetosphäre von SMBH. Die Strahlungsverluste dieser Teilchen kann sehr hohe Energien (VHE, Very High Energy) erreichen, die im Arbeitsbereich des H.E.S.S.-Experiments liegen. Der erwartete Fluss übersteigt die Sensitivität von H.E.S.S. Allerdings könnte die Strahlung durch Strahlungsfelder, die in der Nähe der Beschleunigungsregion sind, abgeschwächt werden. Deswegen muss man galaktische Kerne beobachten, die eine niedrige Leuchtdichte aufweisen. Das erste mit den H.E.S.S. Teleskopen untersuchte Objekt ist der Spitzenkandidat NGC 1399. Obwohl keine Signal detektiert wurde, kann man wichtige Schlussfolgerungen aus diesen Daten ableiten, zum Beispiel über die maximal erreichbare Energie der Teilchen und über die Magnetfeldstärke. Das Magnetfeldstärkelimit ist $B < 74$ Gauss. Das Limit ist modellabhängig und das Ergebnis unter diesen Annahmen skaliert. Dies ist gleichwohl die strikteste empirische Rahmenbedingung. Da kein Signal gefunden wurde, wurde eine neue Technik benutzt: drei Felder von Galaxienhaufen wurden aufaddiert und dann analysiert. Auch wurde in allen drei Beobachtungsfeldern nach aktiven galaktischen Kernen gesucht; die Suche lieferte keinen Fund. Unter diesen Annahmen werden die Möglichkeiten des zukünftigen CTA Observatoriums vorgestellt. Zum Abschluß werden kurz die erwarteten relativistischen Effekte auf die Emission von VHE-Strahlung in der Nähe eines supermassereichen Schwarzen Loches diskutiert.

Contents

Introduction	I
1 The H.E.S.S. Experiment	1
1.1 The Imaging Cherenkov Technique	2
1.1.1 The H.E.S.S. Array	2
1.2 Data Analysis	3
1.2.1 Event Reconstruction and Excess Determination	3
1.2.2 Background Estimation	5
1.2.3 Spectral Analysis and Upper Limits	7
1.2.4 Weather Influence on Data Quality	9
2 Extreme Accelerators and Radiation Losses	11
2.1 Cosmic Rays	11
2.1.1 Ultra High Energy Cosmic Rays and the Hillas Criterion	12
2.1.2 Candidates for UHECR Accelerators	14
2.2 The Magnetosphere of SMBH	16
2.2.1 Acceleration in Gaps in the Magnetosphere	18
2.2.2 Centrifugal Acceleration	19
2.3 Radiation Losses	19
2.3.1 Synchrotron and Curvature Emission	20
2.3.2 Inverse Compton Scattering	21
2.3.3 Proton-Proton Interaction	22
2.4 The Role of Absorption	22
2.4.1 The Extension of the VHE Universe	23

2.4.2	Absorption from Internal Fields	23
2.5	The Importance of Passive SMBH	26
3	The Passive SMBH in NGC 1399	29
3.1	Estimate of NGC 1399 VHE γ -ray Luminosity	29
3.1.1	Acceleration Mechanism	30
3.1.2	Emission Processes and Expected VHE γ -ray Luminosity	32
3.1.3	Impact of the SMBH Mass Assumption	35
3.2	Analysis of VHE Data taken with the H.E.S.S. Array	36
3.2.1	Standard Analysis	36
3.2.2	Analysis of Bad Weather Data	37
3.3	Radiation fields of NGC 1399	38
3.3.1	Absorption	42
3.4	Constraints from NGC 1399 Observations	43
3.4.1	Magnetic Field	43
3.4.2	Maximum Particle Energy	44
3.5	Conclusions on NGC 1399	45
4	Stacking Analysis of Passive Systems	47
4.1	The Motivation for Stacking	47
4.2	Sample Selection Criteria	49
4.3	Excess, Significance and Upper Limits	49
4.4	The Virgo Sample of Low Accreting SMBH	50
4.5	The Cluster Fields of Large Ellipticals: Virgo, Fornax and Coma	52
4.5.1	The Binggeli Sample in the Virgo Cluster	52
4.5.2	The Pierini Sample in the Coma Cluster	53
4.5.3	The Ferguson Sample in the Fornax Cluster	54
4.6	Checks on Statistics of the Fields	54
4.7	Implications for UHECR	58
4.8	Conclusions	59

5	Detailed Estimate of VHE Emission from Passive SMBH	63
5.1	Estimating the Magnetic Field Intensity from the Disk-Magnetosphere Connection	63
5.1.1	The Relation between Magnetic Field and Angular Momentum	64
5.1.2	The Dependency on the Mass Accretion Rate and Jet Power .	66
5.2	Flux Predictions	68
5.2.1	Curvature Emission and Synchrotron Emission Spectrum from Accelerated Protons and Electrons	68
5.3	Impact for the Next Generation of γ -ray Observatories	72
5.3.1	Examples: NGC 1399, M87, SgrA*	72
6	Stacking Analysis of Different AGN Classes	77
6.1	VHE Emission from Active Galactic Nuclei	77
6.2	Seyfert Galaxies	79
6.3	Quasars	80
6.4	Faranoff-Riley Radio Galaxies	82
6.5	Implications for UHECR	84
7	Outlook & Conclusions	87
7.1	Outlook: Relativistic Effects on VHE Emission from the Vicinity of SMBH	87
7.1.1	Example: Effects on Triangular Pulses	89
7.1.2	Example: PKS 2155-304	91
7.2	Thesis Conclusions	94
	Bibliography	I

Introduction

This thesis presents the search for emission from a new class of potential VHE sources. Galactic nuclei hosting passive supermassive black holes (SMBH) are investigated with the H.E.S.S. experiment, the most sensitive array of Cherenkov telescopes to date.

Spheroidal systems (such as elliptical galaxies, lenticular galaxies, and early-type spiral galaxies with massive bulges) are commonly believed to host in the central region supermassive black holes with masses in the range $M_{\text{BH}} = 10^6 - 10^9 M_{\odot}$ (Richstone et al., 1998). These SMBH cause emission in all wavelengths, from radio to HE γ -rays (~ 1 GeV). It is in addition widely accepted that SMBH are related to the production of jets and associated to VHE emission through several processes. In blazar-type objects, where the jet is pointing towards the observer, VHE emission is observed in many sources (Schlickeiser, 1996). These VHE sources exhibit usually a double humped Spectral Energy Distribution (SED). The low energy hump can be modelled as synchrotron emission from accelerated electrons, while the high energy hump is due to the energetic accelerated electrons upscattering either their own synchrotron radiation or upscattering an external photon field. A hadronic origin of the VHE emission is also proposed (e.g. Mücke & Protheroe, 2001). VHE emission can also be related to SMBH through the annihilation of particles that are candidates for Dark Matter (Berezinsky et al., 1994). In this scenario the presence of a SMBH steepens the density profile of dark matter and can result in a higher rate of interaction and enhanced emission.

Correlations involving the SMBH masses and properties of their host galaxies have been investigated by many authors. In particular M_{BH} is found to be linked to

the central stellar velocity dispersion (e.g. Gebhardt et al., 2000) and to the mass of the host galaxy bulge (e.g. Magorrian et al., 1998). These observational scaling laws, in addition to confirming the ubiquity of SMBH, have suggested that their activity cycle is tightly linked to the evolution of their host galaxies (e.g. Ferrarese & Merrit, 2000). During the early stages of galaxy evolution SMBH accrete matter at high rates and are observed as bright QSO (Quasi-Stellar Objects). The average radiative output at low energy (e.g. optical) decays from redshift $z>3$ to $z=0$ by almost 2 orders of magnitude. The majority of SMBH in the local universe are hosted in such non-active systems and therefore not embedded in dense radiation fields. In passive systems (i.e. SMBH hosted in nuclei without signatures of broad-band activity, with very low luminosity in all longer wavelengths) VHE γ -rays, if generated, can escape from the nuclear region without suffering from strong absorption via photon-photon pair absorption.

Several models for the production of γ -ray emission in the vicinity of SMBH have been proposed (see e.g. Kafatos & Leiter, 1979; Sikora et al., 1987; Atoyan & Nahapetian, 1989; Mastichiadis & Protheroe, 1990; Slane & Wagh, 1990; Boldt & Gosh, 1999; Levinson, 2000; Neronov et al., 2004; Neronov & Aharonian, 2007; Rieger & Aharonian, 2008; Istomin & Sol, 2009). The predictions from some of these models are tested in this work. Details of the investigated models are given in Chapter 2. The same mechanisms might also be responsible for acceleration of cosmic rays from energies $E > 10^{14}$ eV up to $E \sim 10^{19}$ eV if the particles are able to tap into a significant fraction of the acceleration potential (e.g. Boldt & Gosh, 1999). In order to avoid attenuation on circumnuclear fields, such radiation could escape only if the SMBH does not produce too much low energy radiation. The SMBH would have to be passive at low energies, i. e. most of the radiative losses would have to occur at high energies. In all cases a large mass of the central object is an important characteristic for generating a high VHE flux.

While the detection of VHE gamma-rays in blazar-type systems is facilitated by the superluminal motion (the apparent luminosity is boosted and the optical depth related to photon-photon absorption is reduced, see Schlickeiser (1996)), this is not the case for non-blazar system. Hence, proximity and low luminosity in the

IR/optical domain increase the possibility of a detection. Passive systems, if detected, will contribute to our understanding of the physics and properties of galactic nuclei. In addition they might give us an insight on Ultra High Energy Cosmic Ray (UHECR; $E > 10^{18}$ eV) sources.

Furthermore, VHE emission has been proven to be associated with radiogalaxies in which the jet is misaligned with respect to the observer line of sight. Radiogalaxies are established VHE emitters since M87 (Aharonian et al., 2006a) and CenA (Aharonian et al., 2009a) were detected by the H.E.S.S. telescopes. Moreover, the MAGIC collaboration claimed the detection of signal from the position of the radiogalaxy 3C66B (Aliu et al., 2009). Interestingly, the radiogalaxy M87 also shows fast variability in the VHE domain of the order of few days (Aharonian et al., 2006a), constraining the size of a non-relativistically moving emitting region down to few Schwarzschild radii (R_S).

Local SMBH in non-blazar Active Galactic Nuclei (AGN) can therefore be regarded as a prime candidate for VHE emission and the H.E.S.S. system of Cherenkov Telescopes can be used in order to probe such emission thanks to its good sensitivity.

The main properties of H.E.S.S. and of the related data analysis process are summarized in Chapter 1. The VHE signatures associated with extreme accelerators are recalled in Chapter 2. In such framework, emission is estimated to be detectable in the specific case of NGC 1399. The relative data are analyzed in Chapter 3. No detection was unfortunately obtained, but constraints on the physical parameters of the system are given. In order to obtain deeper exposure, a stacking analysis of several classes was performed. The stacking analysis procedure is described with its application to the case of passive system (Chapter 4) and other classes (Chapter 6). Motivated by the discordancy between the classical prediction of fluxes and the non-detection resulting from H.E.S.S. observations, a detailed estimation of the expected emission from passive SMBH is given in Chapter 5 along with the implication for the next generation of γ -ray facilities. To conclude, in Section 7.1, is presented a work in progress on the study of relativistic effects on VHE emission.

Chapter 1

The H.E.S.S. Experiment

Very High Energy (VHE, $E > 100\text{GeV}$) emission is expected from the vicinity of SMBH. This emission can be studied with ground based facilities thanks to the Cherenkov Technique. The H.E.S.S. experiment is one of the facilities of latest generation that exploits the Cherenkov Technique. The H.E.S.S. system will be described in this chapter with attention to the main characteristics needed for the work presented in the thesis, such as its sensitivity and the superior background rejection. The analysis data process is described in detail in a number of works (see e.g. Berge (2006) and Aharonian et al. (2006b)).



Figure 1.1: The H.E.S.S. array of Cherenkov telescopes on the Khomas Highlands in Namibia. (©2006, picture by Philippe Plailly)



Figure 1.2: One of the four H.E.S.S. telescopes.

1.1 The Imaging Cherenkov Technique

VHE γ -rays will interact with the atmosphere in their way to the ground and this will lead to a particle cascade. Photons will produce pairs that will then emit via bremsstrahlung. Velocities in the cascades are larger than the speed of light in the medium, therefore Cherenkov emission will take place. Particle cascades can also be initiated by hadrons. In this case also strong interactions take place and subshowers will be initiated, thus making the showers broader than the photon initiated ones. The showers will reach the maximum at a height of approximately 10 km, to then illuminate a pool of ~ 120 meters at the ground level. The showers will produce flashes of Cherenkov light that can be imaged by Imaging Atmospheric Cherenkov Telescopes (IACT). From the camera images, properties of the shower and of the primary photon can be reconstructed.

1.1.1 The H.E.S.S. Array

The H.E.S.S. system is an array of four IACTs. It is located in the region of the Khomas Highlands in Namibia at a height of 1800 meters above the sea level. Each

telescope is equipped with a tessellated mirror of 13 meters diameter and a camera with 960 PMTs. The field of view for each PMT is of 0.16° , leading to a total field of view of $\sim 5^\circ$. The telescopes are placed at the corner of a squared configuration with a distance of 120 meters between each other. This enables the system to cover a larger fraction of the light pool from a same event. From a stereoscopic view of the same event in several cameras, the reconstruction of the direction of the primary photon is indeed more precise.

The system was designed to maximize the sensitivity in the energy domain 100GeV-100TeV. The system is capable of detecting a source one hundred times fainter than the Crab Nebula in 25 hours (at a significance level of 5 standard deviations (σ)). The angular resolution is $\sim 0.1^\circ$.

1.2 Data Analysis

The main framework of the data analysis adopted to reduce the H.E.S.S. data is described in several publication (see e.g Aharonian et al. (2006b)). Here only the main steps will be described. The H.E.S.S. observations are conducted in *runs*, where a run correspond to a 28 minutes long observation.

1.2.1 Event Reconstruction and Excess Determination

Images of the events from the particle shower are registered by the camera. In order to reconstruct the information of the primary photon, several steps have to be taken. Only events triggering at least two telescopes simultaneously are considered.

First of all, only pixels with more than 10 p.e. (photoelectrons) and a neighboring pixel with more than 5 p.e. will be kept. This is done in order to reduce the impact of the noise from the PMT themselves. After calibration and cleaning of instrumental noise the raw data is stored.

The following step is a parameterization of the reconstructed image following an “*Hillas-type*” analysis. This analysis was introduced in Hillas (1985). It is based on a geometrical reconstruction in order to discriminate between gamma-ray like

events and hadron events. The intensity of the image will give the information on the energy of the event. The image axis reconstruction will provide the direction of the shower. The gamma-hadron separation is critical in photon-limited very high energy astronomy. Indeed, on average, the detected hadron generated showers are 10^3 times more numerous than the gamma initiated ones. In order to achieve a good gamma-hadron separation, a set of cuts have been defined on the geometrical parameters of the event, whose values are summarized in Table 1.1. The Mean Reduced Scaled Length (MRSL) and Mean Reduced Scaled Width (MRSW) are a measure of the major and minor axis respectively of the elliptical reconstructed image. The θ^2 cut is a cut on the angular distance between the event reconstructed direction and the source location. The distance cut refers to the angular distance between the center of gravity of the reconstructed event and the center of the field of view.

cut	MRSL	MRSL	MRSW	MRSW	θ^2	Size	Distance
	min	max	min	max	max °	min p.e.	max °
standard	-2.0	2.0	-2.0	0.9	0.0125	80	2.0
hard	-2.0	2.0	-2.0	0.7	0.01	200	2.0

Table 1.1: Cuts on the geometrical reconstructed Hillas parameters.

Once the events are safely reconstructed, in order to estimate an underlying excess due to astrophysical sources, it is crucial to reliably estimate the remaining background of gamma-ray like events in the region of interest. The procedure adopted in the present work is described in the next section. The excess will then be

$$N_\gamma = N_{\text{ON}} - \alpha N_{\text{OFF}}, \quad (1.1)$$

where N_{ON} is the number of events detected in the ON region, N_{OFF} in the OFF region and the parameter α is the ratio between exposure in the ON and OFF region. The ON region is taken to be a circular region of the same size of the adopted θ^2 cut around the position of interest. The properties of the OFF region(s)

will be described in the following section together with the background estimation procedure. The significance of an excess is then assessed by the application of the Li-Ma approach. From Eq. 17 in Li & Ma (1983):

$$S = \sqrt{2} \left\{ N_{\text{ON}} \ln \left[\frac{1 + \alpha}{\alpha} \left(\frac{N_{\text{ON}}}{N_{\text{ON}} + N_{\text{OFF}}} \right) \right] + N_{\text{OFF}} \ln \left[(1 + \alpha) \left(\frac{N_{\text{ON}}}{N_{\text{ON}} + N_{\text{OFF}}} \right) \right] \right\}^{1/2}. \quad (1.2)$$

The parameter $\alpha = \text{Exposure}_{\text{ON}} / \text{Exposure}_{\text{OFF}}$ depends on the acceptance of the system for a gamma-ray like event with energy E at a given position (r, ϕ) in the field of view. Indeed the exposure is defined as

$$\text{Exposure} = \int_{\Omega} dS \int_0^T dt \int_0^{\infty} dE A_{\gamma}(E, r, \phi), \quad (1.3)$$

or the number of expected gamma-ray events during a time T in a region Ω of the field of view. An example for a radial profile of acceptance in a field is shown in Fig. 1.3.

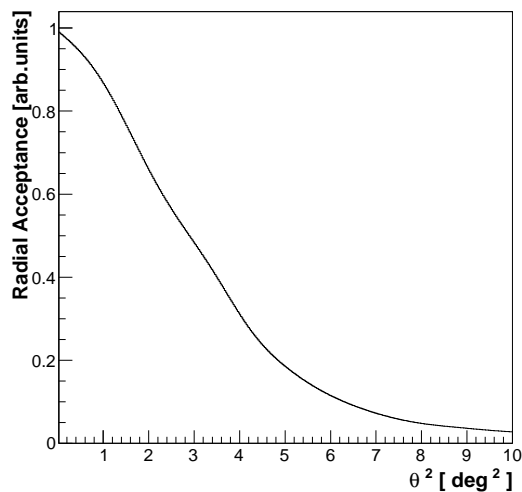


Figure 1.3: Example of radial acceptance for an H.E.S.S. field.

1.2.2 Background Estimation

Thanks to the large field of view of the H.E.S.S. system, the background rejection technique could be improved with respect with the classical approach. As said

before, even after a thorough cleaning and strict cut application, a fraction of hadron initiated events remains. Such events will constitute the background of gamma-ray like events. In the first generation of Cherenkov telescopes this background had to be estimated with the so-called ON-OFF procedure. This means that the OFF events were estimated pointing the telescope in an empty field in the sky with similar characteristics (i.e. same zenith angle and close in time). This is obviously very time consuming.

In the H.E.S.S. large field of view, the events in the OFF region can be estimated in the same pointing. This is achieved thanks to the "wobble" mode, pioneered by the HEGRA Collaboration. The method consists in keeping the source inside the field of view, but with a slight offset from the center of the field of view. Therefore the OFF counts can be taken from the opposite side of the field of view. The offset is then alternated in declination so to smooth gradients in the field of view.

The main background estimation can be divided in:

- *Ring Method.* A ring shaped region around the ON region is used to estimate the background, the configuration is shown in Fig. 1.4 (left). The parameter α corresponds to the ratio of areas of the ON and OFF region and it is typically $\alpha \sim 1/7$. The main advantage of this method is the strength in canceling linear gradients across the field of view. But one has to be careful and apply a correction for the change in acceptance along the ring.
- *Reflected-Region Method.* In this method a number N of OFF region is considered, all of which have the same offset from the center of the field of view that the ON region has. The configuration is shown in Fig. 1.4 (right). The OFF regions have all the same size as the ON region, so $\alpha = 1/N$. This ensure that the acceptance is the same in all the ON and OFF regions, thus making this method well suited for spectrum determination.
- *Template Method.* This method does not estimate the background from a different portion of the sky, but from a different portion of the parameter space of MSRW. So all the informations are extracted from the ON region. As

can be seen from Fig. 1.5, the distribution of MRSW of gamma ray and of cosmic ray is quite distinct.

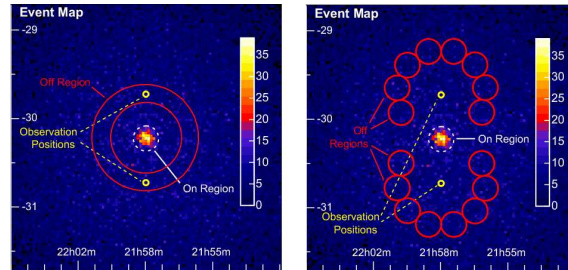


Figure 1.4: Example of background estimations. **Left:** ring method. **Right:** reflected-region method. Figure taken from Berge et al. (2007).

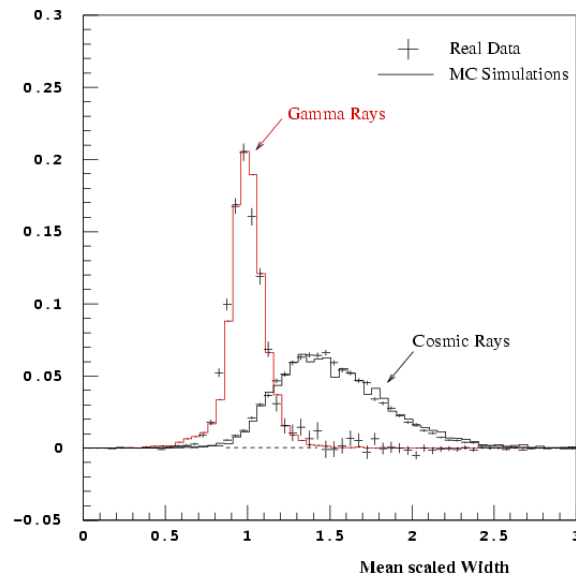


Figure 1.5: Figure taken from Rowell (2003). In the template background is exploited the fact that the distribution of MSRW is distinct for gamma events and for hadron events.

1.2.3 Spectral Analysis and Upper Limits

The sequent step after shape recognition and background subtractions is energy determination, that is directly related to the size of the event image registered by the

camera. In order to determine the spectrum of a source, only events with an energy above a safe energy threshold are considered. The energy threshold is defined as the peak of the distribution of the gamma-rays differential rate. It depends primarily on the configuration cuts used and on the zenith angle and offset of the observation. The spectrum will then be:

$$F(E) = \frac{1}{A_{\text{eff}}} \frac{dN_{\gamma}}{dE dt}, \quad (1.4)$$

where A_{eff} is the effective area of the system. This quantity depends on the reconstructed energy of the event. It ranges from $\sim 10^3 \text{m}^2$ at 100 GeV to more than 10^5m^2 at 1 TeV for an observational zenith angle of 20° (see Fig. 1.6).

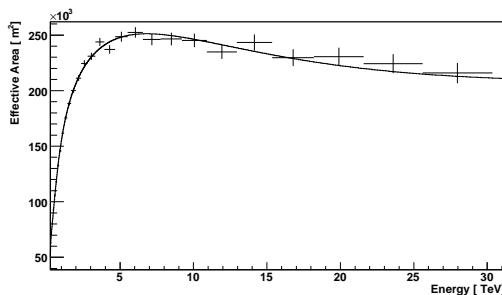


Figure 1.6: Example of effective area for the H.E.S.S. system. The points represent the Monte Carlo simulation, while the fine binned histogram represents the function used in the actual calculation.

Upper Limits

In case of no excess detection, an upper limit would be calculated. This is done assuming a spectral index Γ for the power-law distribution of the differential spectrum

$$\left(\frac{dN}{dE}\right) = I_0 \left(\frac{E}{1 \text{ TeV}}\right)^{-\Gamma}. \quad (1.5)$$

Only events with a reconstructed energy above the energy threshold are considered. A belt of confidence intervals is constructed following the approach of Feldman & Cousins (1998) in order to determine the maximum excess possible for given $N_{\text{ON}}, N_{\text{OFF}}$ and α . The confidence interval is therefore $[\text{Exc}(\text{min}), \text{Exc}(\text{max})]$, where $\text{Exc}(\text{min})=0$.

The maximum excess is then used to calculate the normalization $I_0 = \text{Exc}(\min)/A_{\text{eff,tot}}$ that will be then substituted in Eq. 1.5.

1.2.4 Weather Influence on Data Quality

One important point in data quality selection and subsequent calibration is the influence of weather condition. Indeed the presence of clouds will reduce the number of detected events absorbing the emitted Cherenkov light. In order to cut those observation that are too affected by weather conditions, three parameters can be used. They all rely on the trigger rate recorded by the instrument.

- *Mean system trigger rate of the run.* The run is rejected if this value is less than 70% of the optimal value.
- *Relative change of the trigger rate over the run, δ_1 .* The run is rejected if $\delta_1 > \tan(30^\circ)$.
- *R.m.s variation of the trigger rate over the best fit of the rate, δ_2 .* The run is rejected if $\delta_2 > 10\%$.

If one of the conditions above is fulfilled, then the run is rejected. The influence of the atmosphere is very difficult to reconstruct, but one can assume that it affects in a similar amount showers that are hadron-initiated and gamma-initiated ones. The effect would be to reduce the number of reconstructed events, that can be seen as similar to a reduction of the livetime of the observation. To quantify this reduction a proper study has to be conducted (see e.g. Nolan et al. (2008) and in progress).

In Chapter 3, whenever the term "*cloudy data*" is used, then this refers to runs that failed quality selection only because of a low trigger rate, while the cuts on δ_1 and δ_2 are still applied. Indeed, as said above, a reduction on the trigger rate can be seen as a reduction in the livetime in the observation. On the other end, variations on δ_1 and δ_2 can be due to very unstable weather conditions, whose effect is difficult to predict, or to an improper hardware functioning.

Chapter 2

Extreme Accelerators and Radiation Losses

In this chapter acceleration models relevant for the present work are described. The radiative losses for the accelerated particles are also briefly introduced.

2.1 Cosmic Rays

The study of cosmic rays dates back to the famous work of Viktor Hess in the beginning of the twentieth century (see e.g. Hess, 1912) where he discovered penetrating cosmic radiation. It is now known that the cosmic rays are charged particles entering the earth atmosphere. Their spectrum, observed along 10 orders of magnitude, exhibits an almost featureless power-law distribution, see Fig. 2.1. The only two noticeable features are the so-called knee and ankle, at 10^{15} eV and $10^{18.5}$ eV respectively. Below the knee the index of the power-law spectrum is $\alpha \sim 2.7$ and it then steepens reaching $\alpha \sim 3$, for then hardening again at the ankle with an index $\alpha \sim 2.6$. The spectrum of these energetic charged particles has been studied in detail and it is still source of intense research. In the present paradigm for the origin of cosmic rays, galactic sources are responsible for cosmic rays with energies up to the knee, while the highly energetic cosmic rays are of extragalactic origin. This division comes from the fact that the galactic magnetic field is not strong enough to confine

particles of the higher energies. It has to be kept in mind that the intergalactic and intragalactic magnetic field will deviate the trajectory of a charged particle. This effect is reduced for the more energetic particles, but it is nevertheless important enough to prevent tracing the particle back to its source. For a complete review on cosmic ray physics see e.g. Schlickeiser (2002).

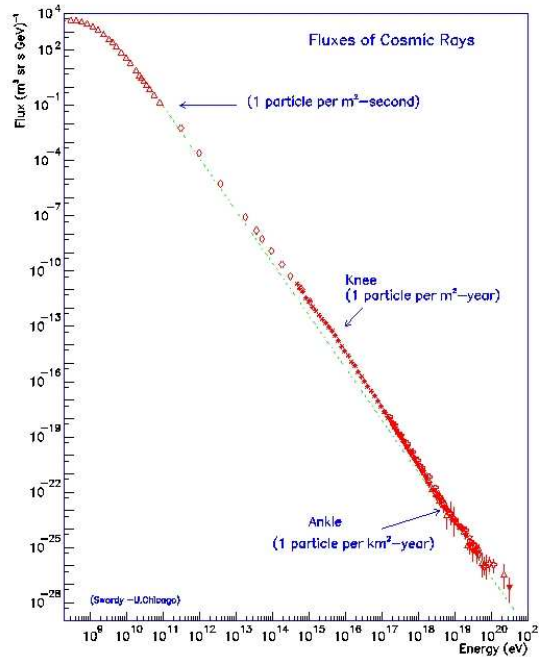


Figure 2.1: Cosmic ray spectrum. Data collected in Swordy (2001).

2.1.1 Ultra High Energy Cosmic Rays and the Hillas Criterion

UHECR ($E > 10^{18.5} \text{eV}$) are believed to be accelerated in extragalactic astrophysical sources. Indeed, the galactic magnetic field is not strong enough to confine such energetic particles. Moreover, if the particles were accelerated in our galaxy we should see a definite anisotropy in their arrival direction along the galactic plane unless there are sources in the halo of the galaxy that are able to accelerate particles to UHE.

However, the observed distribution of the highly energetic cosmic ray is not

isotropic (Abraham et al, 2007b). An investigation of the UHECR detected by the Pierre Auger Observatory (PAO) allowed the Pierre Auger Collaboration to reject the isotropy assumption at a 99% confidence level. The correlation study has been done in two steps. First a correlation between UHECR arrival directions and the location of AGN in the Veron-Cetty Veron Catalog (12th edition, VCV, Veron-Cetty & Veron (2006)) has been studied for an “exploratory scan” (a set of UHECR events). Then the parameters that maximize the correlation (redshift, angular distance and energy) have been applied to an independent set of events in order to test if the correlation would hold. Following this study, the Pierre Auger Collaboration claimed a correlation between the arrival direction of UHECR and the AGN present in the VCV Catalog. They also state that the catalog could be merely a tracer for the actual accelerators of UHECR (Abraham et al, 2007a). A direct connection between AGN and UHECR is however controversial up to date. It has to be kept in mind that nothing is known about UHECR sources, but the fact that they have to satisfy the so-called “Hillas criterion”: the particles have to be confined in the acceleration region long enough for being able to reach UHE, Hillas (1984). The acceleration of particles is there assumed to happen gradually while the particles cross a shock surface several times. Confining a particle in the acceleration region means that the gyroradius of the particle has to be smaller than the size of the acceleration region:

$$L > \frac{E}{qBc} \quad (2.1)$$

where L is the size of the acceleration region, E and q the energy and charge of the particle respectively and B is the value of the magnetic field in the acceleration region. This condition is shown in Fig. 2.2, where are indicated also some astrophysical objects capable of accelerating UHECR. Galactic nuclei are considered among the possibilities because of the expected high magnetic field in their compact nuclear region; several authors explored already this possibility (see e.g. Boldt & Gosh (1999)). Indeed an equipartition magnetic field for a SMBH of $M_{\text{BH}} = 10^9 M_{\odot}$ is of the order of $B = 10^4$ Gauss (Rees, 1984) and its gravitational radius is of the order of $r_g = 10^{15}$. Another site related to SMBH that can accelerate UHECR, is the extended radio lobe of a radio galaxy, that presents lower magnetic fields ($B \sim \mu\text{G}$)

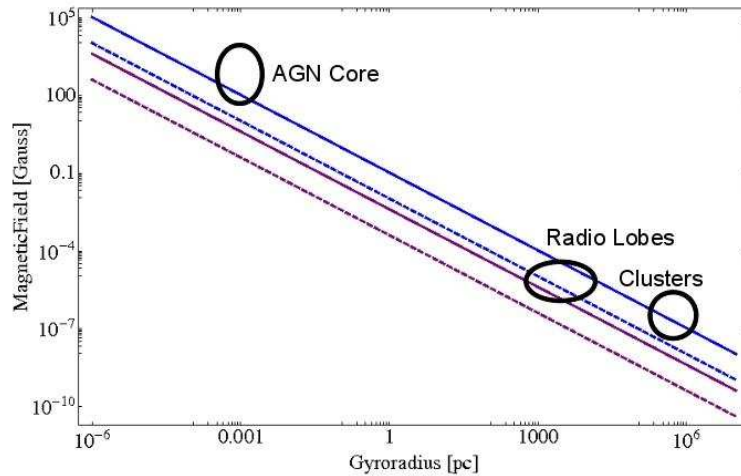


Figure 2.2: Adapted from the Hillas plot, cf Eq. 2.1. The blue lines are for protons of $E = (10^{20}, 10^{19})$ eV (solid, dashed), while the violet lines are for iron nuclei of the same energies.

but sizes of the order of 50 Mpc (Hardcastle et al., 2009). Galaxy clusters also have typical magnetic fields of $B \sim \mu\text{G}$ and extend for several Mpc (Aharonian et al., 2009b).

The systems that are sources of UHECR, will have VHE γ -ray emission associated (see Section 2.3), the detection of which would uniquely pinpoint the source.

2.1.2 Candidates for UHECR Accelerators

Why would the claim of a correlation between AGN location and the arrival direction of UHECR be controversial? In Fig 2.3, the distribution of events with energies $E > 57$ EeV is shown superimposed on the galaxies selected from the Veron-Cetty Veron (VCV, Veron-Cetty & Veron (2006)) catalog. The catalog is highly inhomogeneous and incomplete as the authors themselves say. The only cut made in the study of the PAO data is for the redshift of the source, required to be $z < 0.017$. This value comes from the optimization of parameters from the “exploratory scan” as described in the previous section. In order to explore the claimed association of the

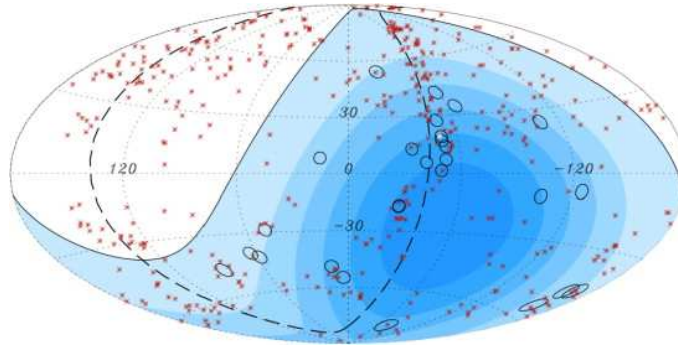


Figure 2.3: Sky map showing the distribution of the galaxies selected in the VCV (Veron-Cetty & Veron, 2006). Overplotted are the arrival direction of the UHECR events as detected by the PAO. The color shading reflects the exposure. (Abraham et al, 2007a).

distribution of UHECR with the Veron-Cetty Veron Catalog, a little exercise can be carried out. In the following, no detailed correlation study has been made, but a visual inspection will suffice.

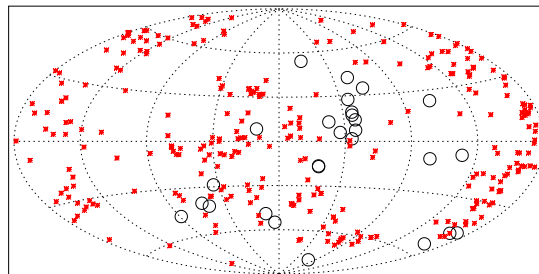


Figure 2.4: Distribution of objects in the 7th edition of the VCV Catalog (Veron-Cetty & Veron, 1996) in galactic coordinates. Superimposed are the Auger events as in Fig. 2.3.

First of all, one can easily demonstrate that the catalog is not homogeneous nor complete. Indeed, the distribution of the objects traces the most observed fields (e.g. the SLOAN sky survey that focuses on fields observable from the northern

hemisphere, Schneider (2007)). This can be seen from Fig. 2.4, where the Auger events are superimposed on the galaxies present in the 7th Edition of the catalog (pre-SLOAN, Veron-Cetty & Veron (1996)). Moreover, if one goes further out in

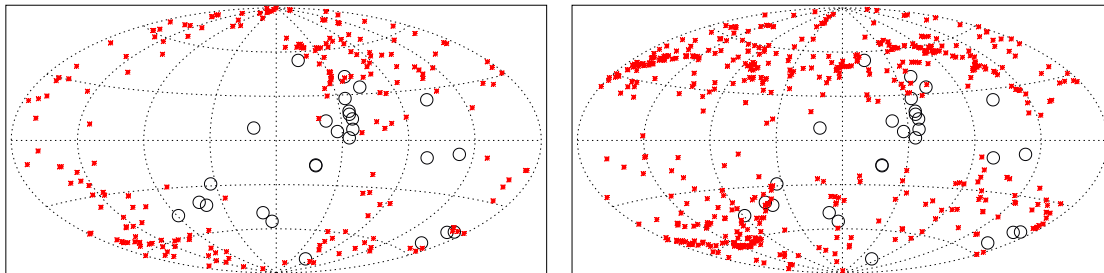


Figure 2.5: Distribution of objects selected from the VCV in different redshift ranges. **Left:** $0.017 < z < 0.024$. **Right:** $0.04 < z < 0.05$. Superimposed are the Auger events.

redshift, one can see how the distribution of galaxies gets more isotropic, see Fig. 2.5. In addition, one can attempt to select from the catalog a “physically selected” sample. Indeed, not every kind of AGN are expected to accelerate UHECR. As was discussed before from the Hillas condition, only the ones that present a strong magnetic field in the central region, or present large scale lobes can be considered. Especially in the later case, these objects will present a high radio luminosity. If one tries to select the objects in the catalog that are radio-loud, the correlation vanishes, as can be seen from Fig. 2.6.

2.2 The Magnetosphere of SMBH

A super-massive black hole, as every non-charged black hole, cannot sustain a magnetosphere on its own. Charged black holes in astrophysical environments, if formed, are expected to quickly accrete matter of opposite charge and be electrically neutralized (Thorne, Price & Macdonald, 1986). However, the SMBH will accrete plasma that carries a magnetic flux. An externally supported magnetosphere will then be

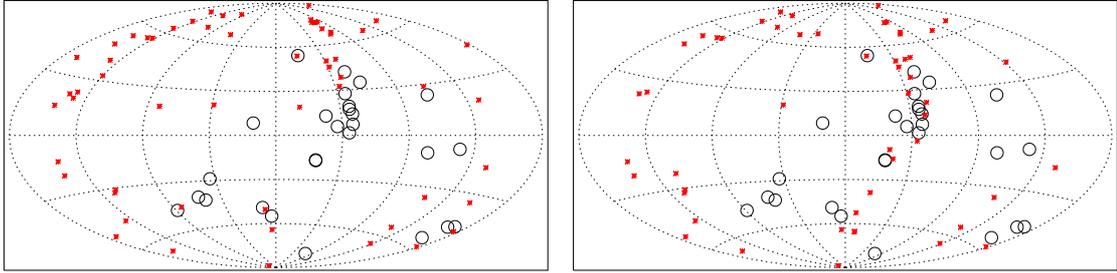


Figure 2.6: Distribution of objects selected from the VCV based on their radio flux (and $z < 0.017$). **Left:** $F_{20\text{cm}} > 0.1$ Jy. **Right:** $F_{6\text{cm}} > 0.1$ Jy. Superimposed are the Auger events.

created, but its topology it is still under investigation (see e.g. Hirose et al (2004)). There are several ways for the disk magnetic field to be linked to the magnetosphere, examples are shown in Fig. 2.7. Intensity and configuration of the magnetic field

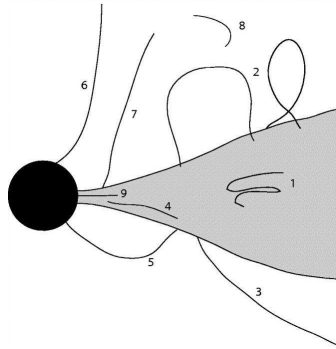


Figure 2.7: From Hirose et al (2004), possible magnetic field configurations.

will depend principally on the plasma density and on the geometry of the accreting flow and ultimately the magnetic field energy will originate from the energy of the accreting flow.

2.2.1 Acceleration in Gaps in the Magnetosphere

It is possible to have gaps in the field potential and a non-zero component of the electric field \mathbf{E} parallel to the magnetic field \mathbf{B} . In these gaps particles will be linearly accelerated by the voltage drop (see e.g. Neronov & Aharonian (2007)). Gaps are present whenever the charge density is smaller than the Goldreich-Julian value (Goldreich & Julian, 1969):

$$\rho_{GJ} = \frac{\nabla \cdot \mathbf{E}}{4\pi} = -\frac{\Omega \cdot \mathbf{B}}{2\pi c} \left[1 - \left(\frac{\Omega r}{c} \right)^2 \sin^2 \theta \right]^{-1}, \quad (2.2)$$

where Ω is the angular velocity of the black hole and (r, θ, ϕ) are polar coordinates with θ measured from the rotation axis. For maximum rotational frequency and for the aligned magnetic and rotational axis, one can write:

$$n_{q,GJ} = \frac{\Omega B}{2\pi c q}, \quad (2.3)$$

or a number density of particles with charge q of $n_q = 0.022 \text{cm}^{-3}$ for a mass $M_{\text{BH}} = 10^9 M_{\odot}$ and a magnetic field of $B = 10^4$ Gauss (Neronov et al., 2007). The scaling with mass comes from the angular velocity Ω .

Typical densities in the surrounding of SMBH are much larger than the Goldreich-Julian value. But the charge distribution in the magnetosphere of a rotating black hole is non-static, therefore gaps can be created even if the plasma density is relatively higher than $n_{q,GJ}$. Indeed, one can imagine a situation in which charges are lost via magnetohydrodynamical outflows and not replenished immediately because the accretion of plasma happens in a perpendicular plane. Examples of gap configurations dependent on the inclination of the magnetic field are described in e.g. (Neronov & Aharonian, 2007) & (Neronov et al., 2007). However, it has to be noted that the size of the gap considered in (Neronov & Aharonian, 2007) is of the order of the Schwarzschild radius of the central black hole, while it is pretty improbable that such a big gap can be formed (see e.g. Hirotani & Okamoto (1998)).

2.2.2 Centrifugal Acceleration

Acceleration of particles can take place in the surroundings of a SMBH independently from the presence of the field gaps described in the previous section. Indeed, particle can be corotating with the magnetic field lines. They will therefore experience “bead-on-wire” acceleration assuming that the magnetosphere is rotating with a fraction of the rotational velocity of the black hole. The particle will experience not only the centrifugal force, but also the Lorentz force, leading to acceleration along the field line. This model is investigated by e.g. Rieger & Mannheim (2000). Ideally the particle is accelerated until it interacts with the surrounding photon field through inverse Compton scattering. This means that the particles are accelerated up to energies dictated by $t_{\text{acc}} = t_{\text{IC}}$, where $t_{\text{acc}} \propto \gamma_0^{1/2} \gamma^{-1/2}$ with γ_0 the initial Lorentz factor of the particle. t_{IC} is the compton cooling timescale scale given below in Eq. 2.10. In the case of an underluminous system, however, the acceleration will not be limited by inverse Compton losses, but by break down of the “bead-on-wire” configuration at the light cylinder. Still the particle can reach a Lorentz factor of the order $\gamma_L \sim 10^8$, in the case of the underluminous system M 87, (Rieger & Aharonian, 2008).

2.3 Radiation Losses

Particles accelerated in astrophysical objects will be detected at earth, but, as described in the previous sections, the intragalactic magnetic field will deviate them from a straight line trajectory. Therefore the only way of pinpointing the location of the source is to trace the radiation losses that particles undergo while accelerated. Radiation losses due to matter or photon field encountered by the particle once left the accelerator system are not considered here. The characteristics of relevant radiation losses are summarized in the following. All equations given in the following are expressed in cgs units.

2.3.1 Synchrotron and Curvature Emission

In a magnetized system, one can expect relativistic particles of energy E_{part} and charge q to lose their energy by synchrotron emission. The component of the magnetic field of interest is B_{\perp} . The timescale of the cooling process is (Rybicki & Lightman, 1979):

$$t_{\text{sync}} = \frac{3m_{\text{part}}^3 c^5}{2qB_{\perp}^2} \gamma_{\text{part}}^{-1}, \quad (2.4)$$

and the emission will be at the typical frequency of

$$\nu_{\text{syn}} = 0.29 \frac{4}{3} \frac{q}{m_{\text{part}} c} B_{\perp} \gamma_{\text{part}}^2, \quad (2.5)$$

where $\gamma_{\text{part}} = (m_{\text{part}} c^2 / E)$ is the Lorentz factor of the particle. For linearly accelerated particles, there is an intrinsic cut-off in the photon energy spectra at

$$E_{\text{part, cut-off}} = \frac{9}{4\alpha_f \eta} m_{\text{part}} c^2, \quad (2.6)$$

where α_f is the fine structure constant and m_{part} is the particle mass (Aharonian, 2000). This translates for electrons to $E_{e, \text{cutoff}} \simeq 0.16$ GeV and $E_{p, \text{cutoff}} \simeq 300$ GeV for protons.

If the electrons are accelerated along the field lines, then the synchrotron losses are not important, while the dominant losses will be due to curvature emission. In this case the cooling timescale is:

$$t_{\text{curv}} = \frac{1}{2} \frac{R_{\text{curv}}^2 m_{\text{part}}}{q^2} \gamma_{\text{part}}^{-3}, \quad (2.7)$$

where R_{curv} is the curvature radius of the magnetic field lines (Berezinskii et al, 1990). Equating the maximum energy gain from acceleration ($\dot{E}_{\text{gain}} = \eta q B c$, with η the efficiency of the acceleration mechanism (see e.g. Aharonian et al., 2002)), and the energy loss for curvature (see Berezinskii et al (1990)), the maximum energy attained by the particle is:

$$E_{\text{part, curv}} = \left(\frac{3\eta B R_{\text{curv}}^2}{2q} \right)^{1/4} m_{\text{part}} c^2, \quad (2.8)$$

that, substituted in the typical frequency

$$\nu_{\text{curv}} = \frac{3}{4\pi} \frac{c}{R_{\text{curv}}} \left(\frac{E_{\text{part}}}{m_{\text{part}} c^2} \right)^3, \quad (2.9)$$

leads to an energy of the emitted photon that is independent of the particle mass. It is interesting to see that, scaling the curvature radius to the Schwarzschild radius of a SMBH with $M_{\text{BH}} = 10^9 M_{\odot}$ and the magnetic field to $B = 10^4$ Gauss, then the emitted photons can reach VHE ($E_{\gamma} \sim 5$ TeV), but, more importantly, protons can be accelerated to UHE $E_{\text{p,curv}} \sim 3 \times 10^{19}$ eV.

A more detailed treatment of the emerging radiation spectrum from both synchrotron and curvature processes will be given in Section 5.2.1.

2.3.2 Inverse Compton Scattering

Inverse Compton Scattering can be divided in Thomson and Klein-Nishina regimes. The only parameter that regulates the transition is the product of the energies of the incident electron E_e and of the up-scattered photon E_{γ} . In the limiting case in which $E_e E_{\gamma} \ll (m_e c^2)^2$ (Thomson regime), the Compton cross section can be approximated by the Thompson cross section and it is independent of the energy of the photon. In the case in which $E_e E_{\gamma} \gg (m_e c^2)^2$ (Klein-Nishina regime), the cross section depends inversely on the energy of the photon.

It can be shown that (Rybicki & Lightman, 1979):

- $E_e E_{\gamma} \ll (m_e c^2)^2$ Thomson regime $E_{\gamma, \text{IC}} \approx 5 \left[\frac{\epsilon}{10^{-2} \text{eV}} \right] \left[\frac{E_e}{10 \text{TeV}} \right]^2 \text{TeV}$;
- $E_e E_{\gamma} \gg (m_e c^2)^2$ Klein-Nishina regime $E_{\gamma, \text{IC}} = E_e$.

The cooling time in the Thompson regime is

$$t_{\text{IC}} = \frac{3}{16\pi c} \frac{(m_e c^2)^3}{q^4} \gamma^{-1} U_{\text{ph}}^{-1}, \quad (2.10)$$

where U_{ph} is the energy density of the soft photon field, decreases for increasing energies of the electron. It has to be noted that in the Klein-Nishina regime the cooling time $t_{\text{IC}} \propto E_e (\ln E_e)^{-1}$ increases with the energy of the electron. However, the electron loses a small fraction of its energy in each Compton scattering in the Thompson regime, while loses a sizeable fraction of its energy in the Klein-Nishina regime.

2.3.3 Proton-Proton Interaction

Protons can lose their energy by interacting with matter (Berezinskii et al, 1990). In particular, proton-proton interaction will lead to the creation of charged π^\pm and neutral pions π^0 . Indeed, one can have:

$$p + p \rightarrow \pi^\pm + X \qquad \pi^\pm \rightarrow \mu^\pm \rightarrow e^\pm \gamma \nu \bar{\nu} \qquad (2.11)$$

$$p + p \rightarrow \pi^0 + X \qquad \pi^0 \rightarrow \gamma + \gamma \qquad (2.12)$$

where X are the number of protons (p) or neutrons (n) that are needed in order to assure charge conservation. For example a possible nuclear interaction is $p + p \rightarrow p + n + \pi^+ + a(\pi^+ + \pi^-) + b\pi^0$, with a and b integers (other examples in Table 5.1 in Schlickeiser, 2002). All the channels will eventually produce photons, but the main amount will come from the “neutral” channel in Eq. 2.12. An interesting part about the decays described in Eq. 2.11 is that they lead to the production of high energy neutrino from the decay of charged pions. The threshold for pp interaction is of the order of $E_{\text{th}} = 2m_\pi c^2(1 + m_\pi/4m_p) \sim 280$ MeV. The cross section of the process depends weakly from energy and can be estimated as $\sigma_{pp} = 40$ mb. The dependency on energy is so weak that the losses of energy via proton-proton interaction will not affect the spectrum of the parent particle population. The associated cooling time is (Aharonian, 2004):

$$t_{\text{pp}} \simeq \frac{1}{\sigma_{\text{pp}} n_{\text{max}} c} \simeq \left(\frac{n_{\text{max}}}{10^7 \text{cm}^{-3}} \right)^{-1} 15 \text{ yr.} \qquad (2.13)$$

The energy of the emitted photon is (Berezinskii et al, 1990):

$$E_\gamma = \frac{1}{2} m_{\pi^0} c^2 [1 + (v/c) \cos\theta] \gamma_{\pi^0}^{-1}, \qquad (2.14)$$

where γ_{π^0} is the Lorentz factor of the neutral pion, v its velocity and θ is the angle between the particle velocity and the photon momentum.

2.4 The Role of Absorption

In the previous section it was shown how the radiation losses of accelerated particles could reach the VHE domain and that cooling generally becomes more efficient with

increasing energies. However, photon fields internal or external to the system can absorb the putative VHE emission. In the case of photons of energy E , the most effective interaction at the peak of the cross section is with background photons of energy:

$$\epsilon \approx 1 (E/1\text{TeV})^{-1} \text{ eV}. \quad (2.15)$$

Therefore, for VHE photons, the most effective interaction is with infrared photons.

2.4.1 The Extension of the VHE Universe

Any VHE emission will interact with Extragalactic Background Light (EBL, Aharonian et al. (2006c)). The effect will be to reduce the detected flux of the source by $F_{\text{obs}} = F_{\text{em}} e^{-\tau}$, where τ is the opacity of the process. Plotting the attenuation $e^{-\tau}$ as a function of VHE photon energy (see Fig. 2.8), one could expect the attenuation to be not critical for detecting sources in the VHE regime when $z \lesssim 0.3$. However, the detection of the source 3C279 at a redshift of $z=0.53$ was claimed in Albert et al. (2008). A direct product of the EBL attenuation will be to soften the spectra of VHE sources.

2.4.2 Absorption from Internal Fields

Spherical Absorbing Field

Photon photon pair absorption can also be due to fields internal to the source. These fields are related to the central black hole itself. Indeed, in addition to the particles accelerated to UHE that are of interest for this work, one can expect populations of low energetic particles to create soft photon fields via synchrotron emission, but also via non-thermal bremsstrahlung. This fields will be in addition to the thermal emission from the stellar population. The luminosity of a soft photon field that would absorb the VHE photon field, spherically distributed, in a source of luminosity L and radius R , has to be

$$L(\epsilon) \leq \frac{4\pi R\epsilon c}{\sigma_{\gamma\gamma}}, \quad (2.16)$$

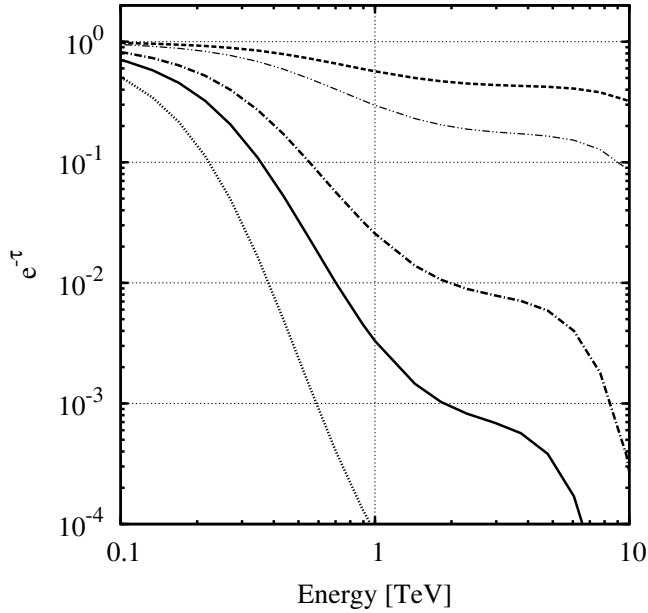


Figure 2.8: Attenuation as a function of VHE photon energy assuming the EBL model in (Aharonian et al., 2006c). Adapted from (Behera & Wagner, 2009); curves are for (from top to bottom) $z = 0.05, 0.1, 0.25, 0.35$ and 0.5

in order for the opacity $\tau < 1$. The energy of the soft photon field ϵ is given by Eq. 2.15 and $\sigma_{\gamma\gamma} \sim 1.3 \times 10^{-25} \text{cm}^2$ at the maximum (Neronov & Aharonian, 2007).

Absorption from Synchrotron Emission of Created Pairs

Absorption can be related also to the production of VHE emission itself. In this scenario (Stawarz & Kirk, 2007), a magnetized system can sustain pair production on its own. From a photon field with photon energy $\epsilon \equiv \epsilon m_e c^2 \gg 1$ pairs are created and they emit synchrotron radiation, producing a soft photon field with photon energy $\epsilon_0 \equiv \epsilon_0 m_e c^2 \ll 1$. This will happen for the value of magnetic fields and energies

$$B = 6B_{\text{cr}}\epsilon^{-3}, \quad (2.17)$$

where $B_{\text{cr}} = 4.4 \times 10^{13}$ Gauss is the magnetic field at which quantum effects start to become important. The allowed parameter space is shown in Fig. 2.9.

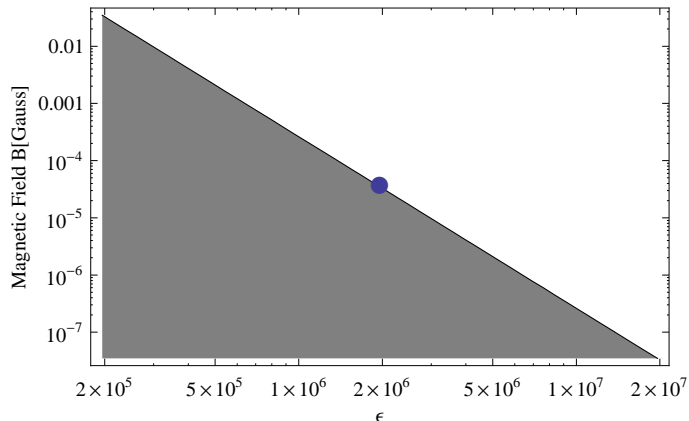


Figure 2.9: Dependency of the magnetic field on the photon energy from Eq. 2.17. The non-shaded area represent the part of the parameter space in which pair production will happen and the point represent $\varepsilon = 1$ TeV.

In Stawarz & Kirk (2007) is derived that, in order to avoid absorption

$$l_{\text{inj}} = \frac{\varepsilon L_{\text{inj}} \sigma_T}{4\pi m_e c^3 R} < 3, \quad (2.18)$$

where L_{inj} is the luminosity per unit energy of the hard photon field injected in the system.

Also, absorption can be avoided whenever the magnetic field is low. This is regulated by the parameter

$$l_B = \frac{\varepsilon U_B R \sigma_T}{m_e c^2}, \quad (2.19)$$

where U_B is the energy density of the magnetic field.

A signature of absorption from synchrotron radiation due to runaway pair production, would be to detect the soft photon field in which the injected luminosity would be degraded. The peak of the synchrotron emission would be at:

$$\nu_{\text{syn}} = 0.29 \frac{4}{3} \frac{q}{m_e c} B \gamma^2.$$

It is expected that the electron (or positron) of the created pair to have roughly the half of the energy of the progenitor photon. So for a 500 GeV electron ($\gamma = 9.7 \times 10^5$) and a magnetic field of $B=100$ Gauss, the peak would be at $E_{\text{peak}} \sim 2.7$ MeV.

Absorption due to Magnetic Pair Production

An electromagnetic conversion process as pair production can happen in systems with a high value of the magnetic field and high characteristic energy. From Erber (1966), the transition probability for a VHE photon of energy $h\nu$ in a system with a magnetic field B , can be thought as being an increasing function of the parameter

$$\xi = \frac{1}{2} \frac{h\nu}{mc^2} \frac{B}{B_{\text{cr}}}, \quad (2.20)$$

where $B_{\text{cr}} = 4.4 \times 10^{13}$ Gauss is the quantum mechanics limit to the magnetic field strength. For pair production to happen the condition $\xi > 0.1$ has to be satisfied. The non-shaded area in Fig. 2.10 shows the part of the parameters space that would

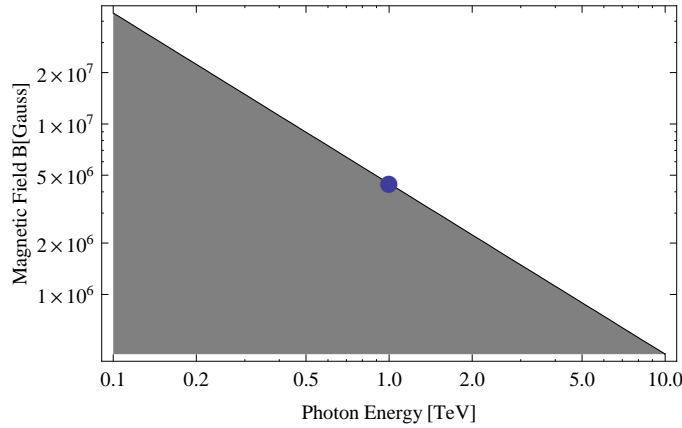


Figure 2.10: Magnetic pair production from the condition $\xi > 0.1$. The non-shaded area describes the part of parameter space in which magnetic pair production can take place. The point indicates the pair of value $E, B=1\text{TeV}, 4.4 \times 10^6$ Gauss.

allow magnetic pair production.

2.5 The Importance of Passive SMBH

It has been seen from the literature presented above that acceleration of particles in the vicinity of a super massive black hole is not only possible, but is crucial in order to understand the physical properties of these systems. It is however important to keep in mind that the objects to be observed have to satisfy the following criteria:

- (1) hosting a very massive SMBH;
- (2) not surrounded by strong photon fields, i.e. passive;
- (3) located in the nearby universe.

Condition (1) comes from the fact that the maximum energy reached by particles and the related radiation scales in many cases with the mass of the black hole (see e.g. Eq. 2.8). Moreover, will be shown in the following chapters that also the expected luminosity of the objects in the VHE regime depends on the mass of the central object ($L_\gamma \propto M_{\text{BH}}^2 B^2$). Condition (2) comes from the fact that if a VHE emission is produced, absorption by photon fields in the galactic nuclei has to be avoided. The strength of photon fields in AGN is high enough to lead to absorption (cf. Eq. 2.16), so one needs to concentrate observational efforts on passive systems. Condition (3) comes from the fact that, in the sources considered here, there is no boosting effect on the luminosity, therefore one may expect lower luminosity than the ones of typically VHE detected blazars. Moreover, concentrating on the nearby universe, one can exclude the effect of the EBL on the VHE radiation.

Passive systems, if detected, will contribute to our understanding of galactic nuclei and give us an insight on whether they are really UHECR sources while enabling us to test the strength of the magnetic field in these sources. In the following chapters the models presented here will be tested via H.E.S.S. observations of several objects.

Chapter 3

The Passive SMBH in NGC 1399

In order to test particle acceleration in the vicinity of SMBH, observations of the passive SMBH in the core of NGC 1399, the central galaxy of the Fornax cluster, were conducted with the H.E.S.S. Cherenkov telescope array.

As will be shown later, given the low photon density at low energies, the high mass of the central SMBH, the proximity and location in the southern sky, NGC 1399 emerged as the best candidate for the study of passive SMBH.

The expected luminosity in the VHE regime is estimated to exceed the sensitivity threshold of the H.E.S.S. array.

In this chapter, the analysis of the H.E.S.S. data is presented and the results are discussed in a multiwavelength perspective. Finally, constraints on the physical parameters of the system are derived.

3.1 Estimate of NGC 1399 VHE γ -ray Luminosity

As already mentioned in Section 2.5, in order to maximize the probability of detection of passive galactic nuclei, observations have to be focused on objects with massive black holes and in the nearby universe. The most massive black holes can be found in the large ellipticals at the center of galaxy clusters. Indeed, the nearest SMBH, that can be observed by H.E.S.S. thanks to their position in the southern sky, reside in the giant radio galaxy CentaurusA and in the central region of the Virgo

cluster, especially in M87. Also to be considered is SgrA*, in the galactic center, that, despite the low mass of the black hole of $M_{\text{BH}} \sim 3 \times 10^6 M_{\odot}$, would obviously be a good candidate thanks to its proximity. These galactic nuclei are already observed and detected by the H.E.S.S. experiment. However, the signal detected from the galactic center is not yet associated with the central SMBH (Aharonian et al., 2009c). Concerning the radiogalaxies CenA and M87, the detected VHE emission might be associated with features of the powerful inner jets (Aharonian et al., 2006a, 2009a). Excluding the Centaurus and Virgo cluster for the argument given above, one of the closest clusters visible from the southern hemisphere is the Fornax cluster. The giant elliptical galaxy NGC 1399 is located in the central region of the Fornax cluster at a distance of 20.3 Mpc. An SMBH of $M_{\text{BH}} = 1 \times 10^9 M_{\odot}$ resides in the central region (O'Connell et al., 2005). The nucleus of this galaxy is well known for its low emissivity at all wavelengths (O'Connell et al. (2005) and references therein). More details on the characteristic and on multiwavelength observations of the system are given in Section 3.3. This galaxy therefore emerged as the best candidate for the study of passive SMBH.

The expected luminosity and energy range of VHE γ -ray emission from the passive SMBH in NGC 1399 are estimated in the following.

3.1.1 Acceleration Mechanism

If the central black hole is accreting matter that carries magnetic flux, it will develop a magnetosphere. The resulting magnetosphere may be similar to those of neutron stars, even though it has to be kept in mind that the topology of the magnetosphere of a spinning SMBH depends on the mutual inclination of rotation and magnetic axes.

Particle acceleration can be expected in the magnetosphere of SMBH. One example of such a configuration is described in Rieger & Aharonian (2008), where centrifugal acceleration is explored. Moreover acceleration could happen in vacuum gaps, that can occur also in high density environments since the magnetosphere of a rotating black hole is a non-static object (see Neronov & Aharonian, 2007). Those

two models have already been described in Sections 2.2.2 and 2.2.1.

The acceleration potential supplied from a spinning SMBH is $\Delta V \sim 10^{20} a M_9 B_4$ V (Thorne, Price & Macdonald, 1986), leading to a power of :

$$W_{\max} \sim 10^{45} a^2 (M_9)^2 (B_4)^2 \text{ erg s}^{-1}, \quad (3.1)$$

where $M_9 = M_{\text{BH}}/(10^9 M_\odot)$, $B_4 = (B/10^4 \text{ G})$ and $a = J/J_{\max}$ ($J_{\max} = GM/c$ is the maximum angular momentum per unit mass). The higher the value of the magnetic field, the higher will be the associated power.

The magnetic field B near the horizon can be estimated from energy conservation, assuming equipartition with the accretion energy density

$$\frac{B^2}{8\pi} = \frac{1}{2} \rho(r_0) v_r^2(r_0), \quad (3.2)$$

where ρ is the mass density and v_r is the radial infall velocity of the accreting matter. Both quantities are described as functions of r_0 (this being the radius of the inner edge of the disk for disk models, or the Schwarzschild radius in case of spherical models).

For a SMBH with mass $M_{\text{BH}} \sim 10^9 M_\odot$, whose mass accretion rate \dot{M}_a is close to the Eddington value, estimating the value of the magnetic field at R_S through Eq. 3.2 would give a value of the order of $B \sim 10^4$ G. This comes from the fact that the density of the accretion flow $\rho \propto \dot{M}_a$. However the nucleus of NGC 1399 presents a sub-Eddington accretion flow (Pellegrini, 2005). In the case of NGC 1399, a free-fall profile is assumed for the accreting flow, $\rho(r) \propto r^{-3/2}$. The value of plasma density at the accretion radius $n(r_{\text{acc}}) = 0.23 \text{ cm}^{-3}$ (Pellegrini, 2005) is obtained from Chandra observations. The plasma density is then extrapolated from the value at the accretion radius to a value at R_S of $n_{\max} \sim 6 \times 10^7 \text{ cm}^{-3}$. Therefore a value of

$$B_{\text{eq}} \simeq 600 (n(R_S)/10^7)^{1/2} \text{ G} \simeq 1280 \text{ G} \quad (3.3)$$

is obtained.

3.1.2 Emission Processes and Expected VHE γ -ray Luminosity

The determination of the behavior of the spectrum requires a detailed calculation of particle trajectories and interactions that can be done through extensive numerical simulations. For a more detailed model see Neronov & Aharonian (2007). In addition, it is possible to see there how the slope of the resulting spectra depends on the mutual inclination of the magnetic field and the rotational axis of the SMBH, as well as on the viewing angle of the source. In particular is shown how acceleration of particles to energie $E \sim 10^{20}$ eV is possible when the magnetic axis is almost parallel to the rotational axis of the system.

It is however possible to estimate a VHE luminosity for this kind of sources using the radiative power given by Eq. 3.1 as a proxy for the luminosity and deriving the intensity of the magnetic field from energy conservation arguments (see Eq. 3.3). If all the power given by Eq. 3.1 is radiated in the VHE domain and the magnetic field is in equipartition with the plasma energy density:

$$L_\gamma \sim 4 \times 10^{42} a^2 M_9^2 \left(\frac{n(R_S)}{10^7} \right) \text{ erg s}^{-1}. \quad (3.4)$$

The conversion into VHE luminosity can be related to several radiation losses (an overview is given in Section 2.3).

In analogy with the model of Slane & Wagh (1990), particles can radiate via hadronic processes. Protons are accelerated in the outer part of the black hole magnetosphere and collide with other protons present in the accretion disk producing pions, which eventually decay into VHE γ -rays (see details in Section 2.3.3). The available power in this model is assumed to be the same as in Eq. 3.1. With

$$t_{pp} \simeq \frac{1}{\sigma_{pp} n_{\max} c} \simeq 15 \text{ yr}, \quad (3.5)$$

where t_{pp} and $\sigma_{pp} \sim 4 \cdot 10^{-26} \text{ cm}^2$ are the timescale and the cross-section of proton-proton collision, variability is not expected on timescales shorter than a few years.

In other models (Levinson, 2000; Neronov et al., 2004; Neronov & Aharonian, 2007) VHE γ -rays originate from electromagnetic processes, i.e. synchrotron or curvature emission.

Let it be reminded that in the VHE range considered here, synchrotron emission is not feasible, because of an intrinsic cut-off in the photon energy spectra at $E_{p,\text{cutoff}} \simeq 300$ GeV and $E_{e,\text{cutoff}} \simeq 0.16$ GeV, for protons and electrons respectively (see Eq. 2.6). If beaming is relevant, these cut-offs can be higher by a factor of δ , which is the Doppler factor of the moving source.

The energy of curvature photons does not depend on the mass of the particle and is identical for photons emitted by electrons or protons. Equating the maximum energy gain from acceleration ($\dot{E}_{\text{gain}} = \eta q B c$, with η the efficiency of the acceleration mechanism (see e.g. Aharonian et al., 2002)), and the energy loss for curvature (see Berezhinskii et al (1990)), the maximum energy attained by the particle is is:

$$E_{\text{part,curv}} = \left(\frac{3\eta B R_{\text{curv}}^2}{2q} \right)^{1/4} m_{\text{part}} c^2. \quad (3.6)$$

Consequently, the maximum energy attained by photons is:

$$E_{\gamma,\text{curv}} \simeq 4.8\eta \left(\frac{R_{\text{curv}}}{R_{\text{S}}} \right)^{1/2} (M_9)^{1/2} (B_4)^{3/4} \text{TeV}, \quad (3.7)$$

where R_{curv} , the curvature radius of the magnetic field lines, has been scaled to the Schwarzschild radius of the black hole. When curvature losses are the dominant ones, the emission spectrum from curvature radiation can extend up to VHE energies for maximum efficiency of the acceleration process. In particular, in the case of NGC 1399, if protons are accelerated with maximum efficiency through an equipartition magnetic field it would lead to $E_{p,\text{curv}} \simeq 1.65 \times 10^{19}$ eV and $E_{\gamma,\text{curv}} \simeq 1$ TeV.

In the frame of a model in which the particles are accelerated in a vacuum gap in the magnetosphere, the Schwarzschild radius is supposably also the size of the gap. However, it seems rather difficult that the system can sustain such large gaps. Indeed $n_{\text{max}} \gg n_{\text{GJ}} = 2 \times 10^{-3} \text{cm}^{-3}$, where n_{GJ} is the Goldreich-Julian plasma density (see Goldreich & Julian (1969) and Section 2.2.1), calculated from the magnetic field strength derived in Eq. 3.3. Nevertheless, being the magnetosphere of a rotating black hole a non-static object, gaps can be created even if the plasma density is relatively high as described in Section 2.2.1 and 2.2.2.

The power of the gap would be

$$W_{\text{gap}} = N_{\text{part}} \times \left(\frac{dE}{dt} \right)_{\text{curv}} = \frac{2}{3} n_{\text{GJ}} V \frac{q^2 c}{R_{\text{curv}}^2} \left(\frac{E}{mc^2} \right)^4, \quad (3.8)$$

where $V = 4/3\pi R_{\text{g}}^3$ is the volume of the gap (here a sphere, for example) filled with a plasma with a n_{GJ} density. The dependency of the power as a function of the size of the gap is plotted in Fig. 3.1 for different values of the acceleration efficiency. The distribution of particles is assumed to be a δ -function centered on the energy given by 3.6. This power estimate can be reconciled with the one from Eq. 3.1 for a size of the gap of $R_{\text{gap}} \sim 1/3R_{\text{S}}$. As the topology of the gap is unknown, Eq. 3.1 will be used as estimation of the power from now on.

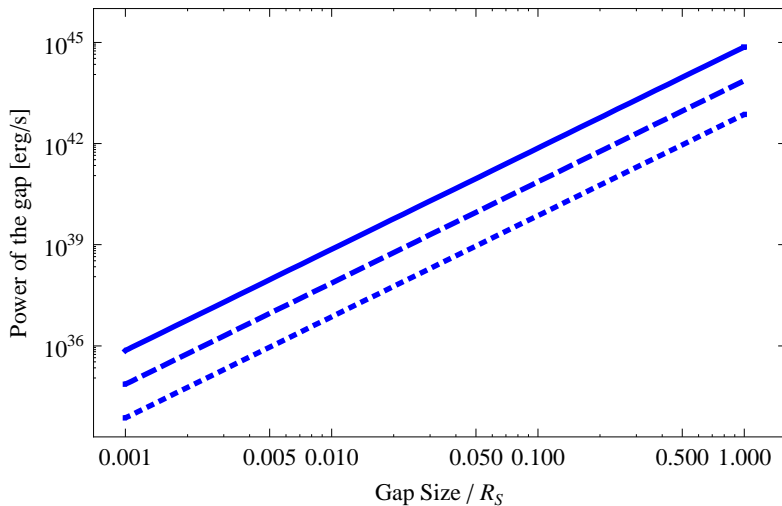


Figure 3.1: Power available from gap with density of particles equal to the Goldreich Julian value for an equipartition magnetic field. The power is plotted against the size of the gap. Different values of acceleration efficiency are represented: $\eta = 1$, solid line; $\eta = 0.1$, dashed line; $\eta = 0.01$, dotted line.

Another energy loss mechanism that might not be negligible for the accelerated particles is due to Inverse Compton (IC) collision with a low-energy photon field. Being $L_{\text{IR}}, R_{\text{IR}}, \epsilon_{\text{IR}}$ respectively the luminosity, radius of the region and energy of the infrared soft photon field, it is possible to calculate the maximum energy attainable by the electrons in the case of maximum efficiency of the acceleration process

(Rybicki & Lightman, 1979):

$$\begin{aligned} E_{e,\max} &\simeq \left(\frac{3m^4c^9}{4e^3}\right)^{1/2} \left(\frac{B}{L_{\text{IR}}}\right)^{1/2} R_{\text{IR}} \\ &\simeq 280 B_4^{1/2} M_9 \left(\frac{R_{\text{IR}}}{R_S}\right) \left(\frac{10^{41}\text{erg s}^{-1}}{L_{\text{IR}}}\right)^{1/2} \text{TeV}. \end{aligned} \quad (3.9)$$

It is then possible to calculate:

- the average energy of a Compton upscattered photon (Thomson regime)(Blumenthal & Gould, 1970)

$$E_{\gamma,\text{IC}} \simeq 5 \left[\frac{\epsilon}{10^{-2}\text{eV}}\right] \left[\frac{E_e}{10\text{TeV}}\right]^2 \text{TeV}; \quad (3.10)$$

- the average energy of a Compton upscattered photon (KN regime)(Blumenthal & Gould, 1970)

$$E_{\gamma,\text{IC}} = E_e. \quad (3.11)$$

3.1.3 Impact of the SMBH Mass Assumption

In all the previous sections, it has been assumed that the estimation of the mass of the SMBH in the center of NGC 1399, $M_{\text{BH}} = 1 \times 10^9 M_{\odot}$, was solid. It is indeed the best estimate up to date, based on the relation $M_{\text{BH}} \propto \sigma^{4.72}$ Merrit & Ferrarese (2001), where σ is the velocity dispersion, leading to the value $M_{\text{BH}} = 1.06 \times 10^9 M_{\odot}$. Kinematic studies in Houghton et al (2006) lead to a slightly higher value of $M_{\text{BH}} = 1.2_{-0.6}^{+0.5} \times 10^9 M_{\odot}$. One drawback of the dynamical studies conducted so far is that the contribution of the dark matter halo was never included in the modeling of the density profile of the galaxy. The additional dark matter component was although considered in the modeling of the M87 density profile in Gebhardt & Thomas (2009) and the estimate on the mass resulted higher than the canonical estimates by a factor 2.

Because of the degeneracy between mass-to-light ratio and black hole mass, a similar effect can be expected in NGC 1399 as the light profile is similar to the one in M87 (cf Fig. 3.2). If the mass of the black hole is indeed underestimated, then the expected VHE luminosity would be even higher.

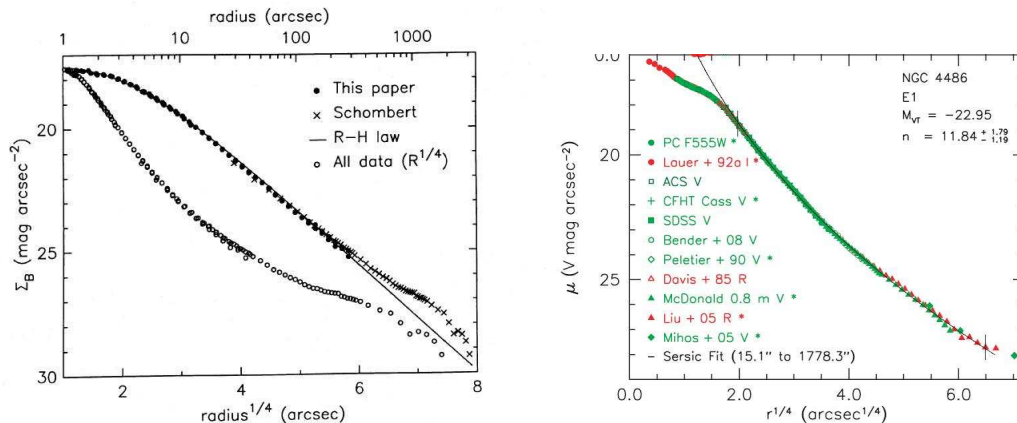


Figure 3.2: Light profile of the galaxy NGC 1399 (left, Killeen & Bicknell (1988)) and M 87 (right, Kormendy et al. (1988)).

3.2 Analysis of VHE Data taken with the H.E.S.S. Array

3.2.1 Standard Analysis

NGC 1399 was observed with the H.E.S.S. array of imaging atmospheric-Cherenkov telescopes in 2005 and 2007 for a total of 38 h exposure (88 runs of ~ 28 min each). After applying the standard H.E.S.S. data-quality selection criteria (Aharonian et al., 2006b) a total of 18 hours live time remain. The mean zenith angle is $Z_{\text{mean}} = 19.6^\circ$ and the mean offset is $\Psi_{\text{mean}} = 0.85^\circ$. The data were reduced using standard analysis tools and selection cuts (standard cuts, Aharonian et al., 2006b) and the Reflected-Region method (Berge et al., 2007) for the estimation of the background. A point source analysis was performed with an angular cut of $\theta^2 = 0.0125$ and a size cut of 80 photo-electrons (details in Aharonian et al., 2006b). This leads to a post-analysis threshold of 260 GeV at Z_{mean} . No significant excess (-26 events, -1.1 standard deviations) is detected from NGC 1399 (see Fig. 3.3).

Assuming a photon index of $\Gamma=2.6$, the upper limit (99.9% confidence level; Feldman & Cousins, 1998) on the integral flux above 260 GeV is:

$$I(> 260\text{GeV}) < 1.1 \times 10^{-12} \text{ cm}^{-2}\text{s}^{-1}, \quad (3.12)$$

or 0.7% of the Crab Nebula flux (CF) above the same threshold. Changing the assumed value of Γ does not change the upper limit by much; it can vary from 0.53% CF (hard spectrum, $\Gamma = 2.0$) to 0.94% CF (soft spectrum, $\Gamma = 4.0$).

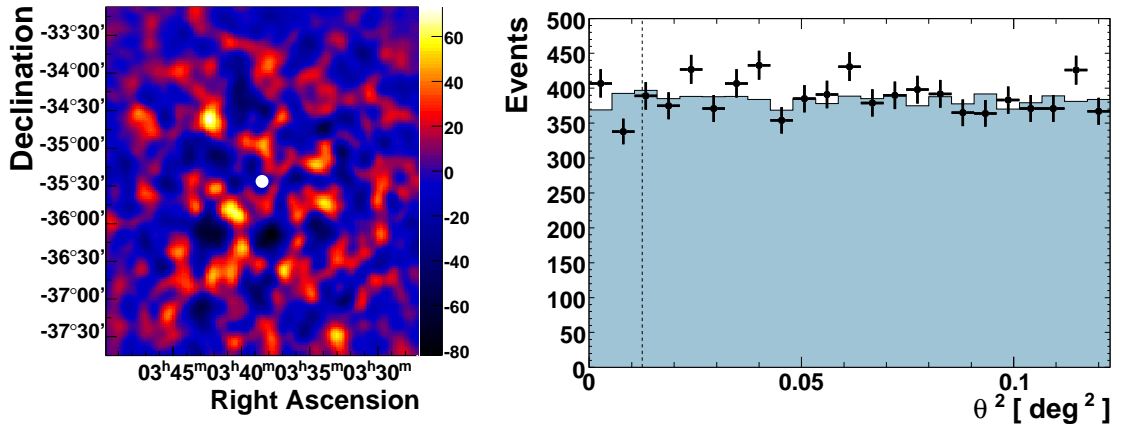


Figure 3.3: **Left:** The smoothed (smoothing radius $r=0.09^\circ$) VHE excess in the region centered on NGC 1399. The central white dot indicates the position of the optical center of NGC 1399. There is no significant excess at any point in the sky map. **Right:** Distribution of events as a function of squared angular distance from NGC 1399 for gamma-ray-like events in the ON region (points) and in the OFF region (filled area, normalized). The dotted line represents the cut for point-like sources.

3.2.2 Analysis of Bad Weather Data

After applying the standard H.E.S.S. data-quality selection criteria (Aharonian et al., 2006b) a total of 18 hours live time remain. Many of the rejected data (~ 16 hours) were taken during light cloud coverage or hazy atmospheric conditions. The remaining ~ 4 hours of observations are rejected because of technical problems. The effect of bad weather conditions would be to lower the trigger rate of the telescope and make it fall below the allowed threshold. The cut is usually at 70% of the "clear sky" trigger rate. This will lead to a reduction of γ -ray like events detection and a shift in the reconstructed energy spectrum. Indeed, a nominally 500 GeV

event can be reconstructed as a, say, 200 GeV event. Therefore, in order to properly reconstruct a spectrum, effective areas have to be calculated on a run by run basis after reconstructing the atmospheric conditions. For a work-in-progress on a similar analysis to H.E.S.S. data with atmospheric simulations and effective area reconstruction, see Nolan et al. (2008).

Nevertheless, an analysis can be conducted concentrating only on excess reconstruction. Results are summarized in Table 3.1 for observations in which all 4 telescopes were used. In the "cloudy data", despite the similar livetime, roughly half of the events are reconstructed in comparison to the good data run. This does not change the outcome of the VHE analysis at the NGC 1399 position. Still no detection would have been obtained.

DATA	N _{ON}	N _{OFF}	α	EXCESS	SIGNIFICANCE	LIVETIME (hrs)
GOOD	731	14407	0.052	-15	-0.55	14.73
CLOUDY	344	8670	0.036	33	1.81	14.21
SUM	1075	23077	0.045	18	0.53	28.94

Table 3.1: Results for 4 telescope data with different selection in the data quality selection. Good data were selected following the standard H.E.S.S. data-quality selection criteria (Aharonian et al., 2006b). "Cloudy data" were selected from those run in the database that would have failed standard selection only because of the trigger value cut. The difference in livetime between the good data presented here and the one presented in Section 3.2.1 comes from the 3.3 hours of 3 telescope data.

3.3 Radiation fields of NGC 1399

The galaxy presents low power antiparallel jets, whose luminosity is $\sim 10^{39} \text{erg s}^{-1}$ between 10^7 Hz and 10^{10} Hz (Killeen et al., 1988). The outflows are confined in projection within the optical extension of the galaxy (see Fig. 3.4). The jets are initially transonic, then decelerate in the inter-stellar medium and end in lobe-like diffuse structure at $\sim 9 \text{ Kpc}$ from the center (Killeen et al., 1988). In the

X-ray imaging is moreover possible to distinguish cavities suggesting that the radio-emitting plasma is producing shocks in the hot X-ray emitting gas (see Fig. 3.5). The estimated power is $P_{\text{jet}} \sim 10^{42} \text{ erg s}^{-1}$ (Shurkin et al., 2008).

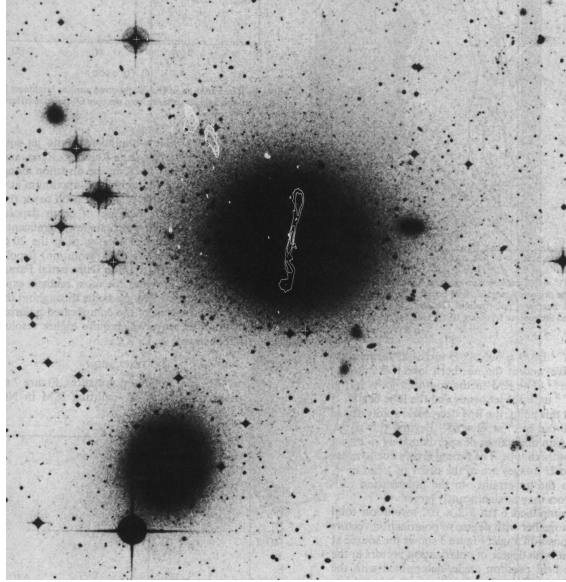


Figure 3.4: Figure taken from Killeen et al. (1988). In NGC 1399 the radio outflows are contained inside the optical extension of the galaxy. Visible are the radio countours from 6cm VLA measurements superimposed on the SRC-J optical survey field. Details in Killeen et al. (1988).

In the X-ray domain, in the central region ($< 50''$, see e.g. Paolillo et al. (2002)), it presents a classical β -profile for the hot gas: $\Sigma \propto [1 + (r/r_0)^2]^{-3\beta+0.5}$, where r is the distance from the center. The profile is concentrated enough to allow an estimate of the central density of $4.6 \times 10^{-25} \text{ g cm}^{-3}$ (Loewenstein et al., 2001).

The weak radio source in the nuclear region was detected with the VLA at 6cm ($\sim 4.9 \text{ GHz}$) with a flux $f(\nu)$ of 10 mJy (Sadler et al., 1989), translating to a luminosity of $L_{\text{radio}} = 2.39 \times 10^{37} \text{ erg s}^{-1}$. The source is slightly more luminous in the optical/UV with a luminosity of $L_{\text{UV}} \sim 1.2 \times 10^{39} \text{ erg s}^{-1}$ (HST data, O'Connell et al. (2005)). Observation taken with the X-ray satellite *Chandra* led only to an upper limit of $L(2 - 10 \text{ KeV}) = 9.7 \times 10^{38} \text{ erg s}^{-1}$.

In Fig. 3.6 ISO IR data and 2MASS-J band observations are showed. These

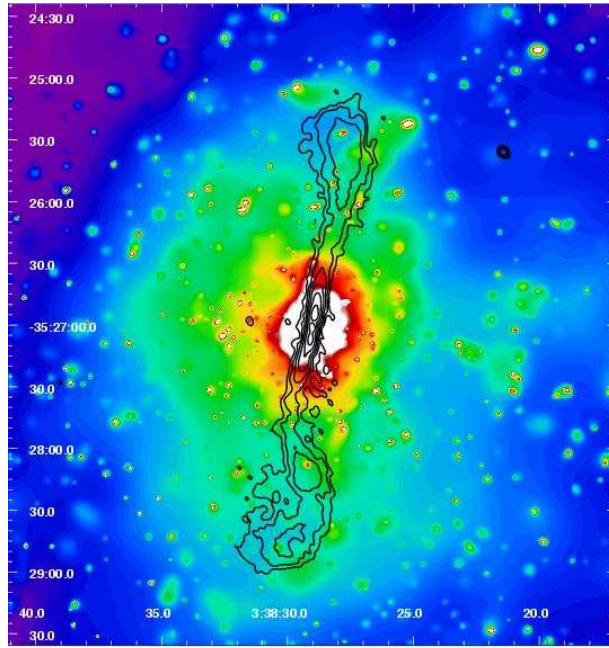


Figure 3.5: Figure taken from Shurkin et al. (2008). It is possible to see how the radio contours coincide with X-ray cavities. Shown are the 1.4GHz VLA measurements superimposed on Chandra X-ray data. Details in Shurkin et al. (2008).

infrared observations are only available with apertures much greater than the ones used for other bands and the resulting fluxes are possibly contaminated strongly by starlight. Assuming a simple Reynolds-Hubble profile for the surface brightness of the galaxy, the infrared luminosity at 1 eV in an aperture of $0.2''$ is $L_{\text{IR}} = 1.74 \times 10^{41} \text{ erg s}^{-1}$.

The nuclear emission is however extremely low in all energy bands. In constructing the spectral energy distribution (SED) of NGC 1399, the observations were selected in order to consider only the nuclear region. To achieve this, only observations taken with the smallest aperture possible were considered (see Fig. 3.6 and its caption) or, in the case of infrared emission, the flux in an aperture comparable to the ones of other band was extrapolated from the available observations.

Regarding VHE data, here it is assumed that the γ -ray emission originates solely from the nucleus, even though the entire galaxy is point-like with the angular resolution of H.E.S.S. (the angular size of the host galaxy is ~ 3 arcmin, (SIMBAD,

2008)). The H.E.S.S. limit on the isotropic VHE γ -ray luminosity is:

$$L_\gamma < 6.2 \times 10^{40} \text{ erg s}^{-1}. \quad (3.13)$$

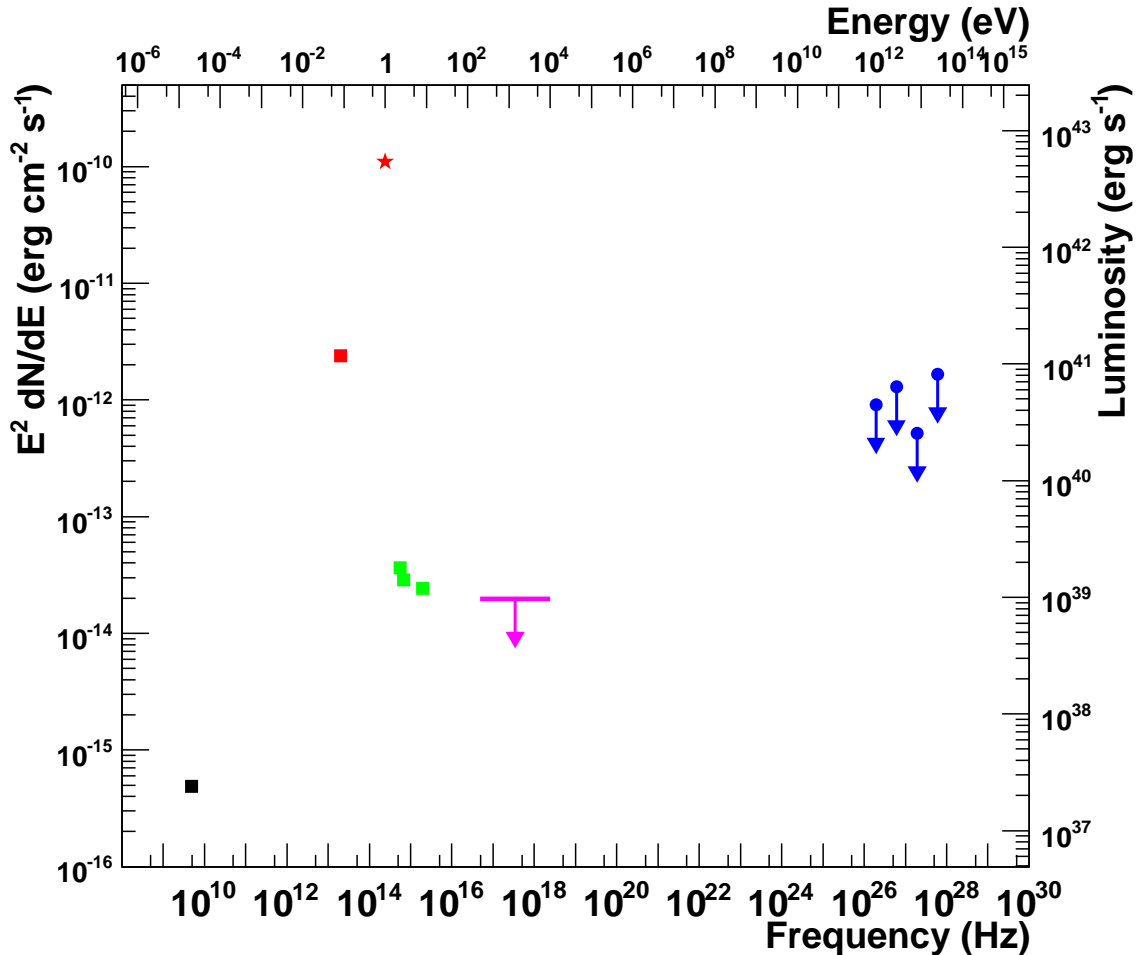


Figure 3.6: The SED of NGC 1399. All archival data are for the core region. The archival points are: VLA radio data (black; Sadler et al. (1989); core component $<0.4''$); $15\mu\text{m}$ ISO IR data (red square; Temi et al. (2005); $5''$ aperture, no host subtraction); 2MASS J-band data (red star; Skrutskie et al. (2006); $4''$ aperture, no host subtraction); HST optical data (green; O'Connell et al. (2005); $0.2''$ aperture), and Chandra X-ray upper limit (solid line; Loewenstein et al. (2001); $3''$ aperture). The blue dots are the H.E.S.S. spectrum 2σ upper limit.

3.3.1 Absorption

In the case of NGC 1399 photon-photon pair absorption is low and should not significantly affect any VHE emission. The optical depth resulting from this absorption, in a source of luminosity L and radius R , is given by:

$$\tau(E, R) = \frac{L(\epsilon) \sigma_{\gamma\gamma}}{4\pi R \epsilon c}. \quad (3.14)$$

In the NGC 1399 system, the visibility of a 200 GeV photon requires $L(\epsilon = 5\text{eV}) < 2.83 \times 10^{42} \text{ erg s}^{-1}$, if the region containing the soft photon field is of the order of 100 times the Schwarzschild radius R_S of the black hole. This condition seems to be satisfied (Fig. 3.6) looking at the very low luminosity detected by HST. Even if more energetic photons are considered, $E > 1\text{TeV}$, the assumed near infrared luminosity allows the size of the emitting region to be as small as $\sim 10R_S$. Hence, VHE photons can escape. An additional photon field that might interact with any VHE γ -rays produced near the SMBH is provided by synchrotron radiation emitted by pairs (Stawarz & Kirk, 2007). This process leads to a $\tau_{\gamma\gamma} > 1$ if the intrinsic luminosity of the system with radius R is higher than $L_{\text{crit}} = \left(10^{-6} \left(\frac{\epsilon}{1\text{GeV}}\right)^4 + 4.4 \times 10^5 \frac{R}{1\text{pc}} \left(\frac{\epsilon}{1\text{GeV}}\right)^{-1}\right) \times 10^{40} \text{ erg s}^{-1}$. This condition translates to $L_{\text{crit}} = 10^{46} \text{ erg s}^{-1}$ for photon energies $\epsilon = 1\text{TeV}$, and to only $L_{\text{crit}} \sim 4 \times 10^{43} \text{ erg s}^{-1}$ in case of $\epsilon = 250\text{GeV}$. Such luminosity would then be observable as synchrotron radiation of the pair plasma and result in a peak in the infrared domain. The observed upper limits in this domain are lower (cf. Fig. 3.6), demonstrating the transparency of VHE γ -rays even in the vicinity of the SMBH. Moreover, one can compute the parameters l_{inj} and l_B described in Section 2.4.2. It can be seen from Fig. 3.7 that the absorption can be avoided as the values of l_{inj} and l_B fall in the optically thin part of the parameter space.

Last, absorption of the produced VHE photons could be also due to the existence of a very high magnetic field. In such case magnetic pair production would take place. In order to avoid this process $B_{\text{abs}} < 4.4 \times 10^6 \text{ Gauss}$, in the case of a photon of 1TeV energy (cf. 2.4.2). One can safely assume that the process is not taking place as B_{abs} is higher than the equipartition value presented in 3.3. In the case of a non-charged black hole whose magnetosphere is sustained accretion, the energy

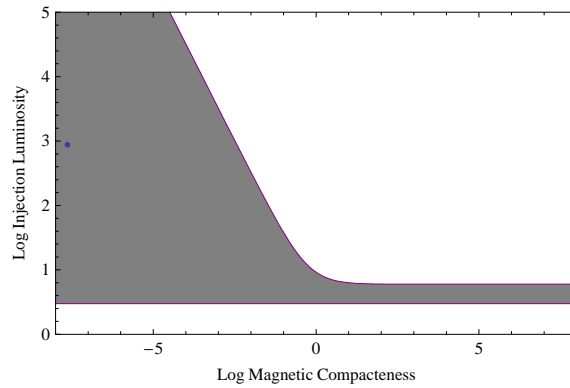


Figure 3.7: Comparison to Fig. 1 in Stawarz & Kirk (2007). The red line divides regions with opacity $\tau < 1$ from $\tau > 1$. The blue point comes from the upper limit derived from H.E.S.S. observations (Eq. 3.13) and the magnetic field relative to 1 Tev (cf. Eq. 2.17).

density of the magnetic field cannot exceed the one of the plasma. A value of the magnetic field higher than equipartition is thus not possible.

3.4 Constraints from NGC 1399 Observations

It is assumed in the following that the acceleration process allows a maximum energy gain with $\dot{E}_{\text{gain}} = \eta q B c$, with $\eta=1$. Moreover the black hole is assumed to be maximally spinning with $J/J_{\text{max}} = a = 1$.

3.4.1 Magnetic Field

With these assumptions, the photon flux for NGC 1399 should be detectable by H.E.S.S. with an isotropic flux $F_{\gamma} \sim 8 \times 10^{-11} a^2 M_9^2 (n(R_S)/10^7) \text{ erg s}^{-1} \text{ cm}^{-2}$ (cf. Eq. 3.4). The non-detection of NGC 1399 shows that, unless one of the assumption is violated, equipartition for the magnetic field is not accurate. The upper limit derived from the observation of NGC 1399 allows to set an upper limit on the value of the magnetic field, assuming the scenarios discussed above.

From Eq. 3.1 it can be written

$$L_\gamma = \xi W_{\max} \sim 10^{45} a^2 (M_9)^2 (B_4)^2 \text{ erg s}^{-1} \quad (3.15)$$

Assuming that all the available power is radiated in the VHE domain ($\xi = 1$), the following limit for a homogeneous magnetic field is obtained from the H.E.S.S. result:

$$B < 74.0 a^{-1} \text{ G}. \quad (3.16)$$

Of course, the hypothesis of maximum efficiency of power-to luminosity conversion is quite extreme. But being the SMBH passive at low energies, most of the radiative losses would have to occur at high energies.

Reconciling the H.E.S.S. upper limit on the magnetic field and canonical equipartition estimates would require to relax the assumption on the efficiency of the accelerator or of the emission mechanism. The dependency of the magnetic field from the efficiency is shown in Fig. 3.8.

Note that also the assumption $a = 1$ may be violated. This assumption depends on the formation history of the black hole. If its growth is dominated by gas accretion and the accreted mass is of the order of the initial mass of the black hole, then it is possible to reach $a = 1$, see Volonteri et al. (2007). This is believed to be true for the SMBH hosted in elliptical galaxies in the nearby universe, but may be violated, for example by chaotic accretion scenarios (Rees, 1984). Then a value of $a \approx 0.01$ may allow equipartition magnetic field and maximum efficiency.

Hence, is interesting to keep all three parameters as free. The mutual dependence is shown in Fig. 3.9.

3.4.2 Maximum Particle Energy

If the intensity of the magnetic field is indeed the one given in Eq. 3.16, then it is possible to calculate the maximum energy reached by the accelerated particles.

If the dominant radiation loss is curvature emission, then the maximum energy is $E_{p,\text{curv}} < 8 \times 10^{18}$ eV for protons and $E_{e,\text{curv}} < 4 \times 10^{15}$ eV. The energy of the associated radiation would not reach the H.E.S.S. energy domain, $E_\gamma < 0.12$ TeV.

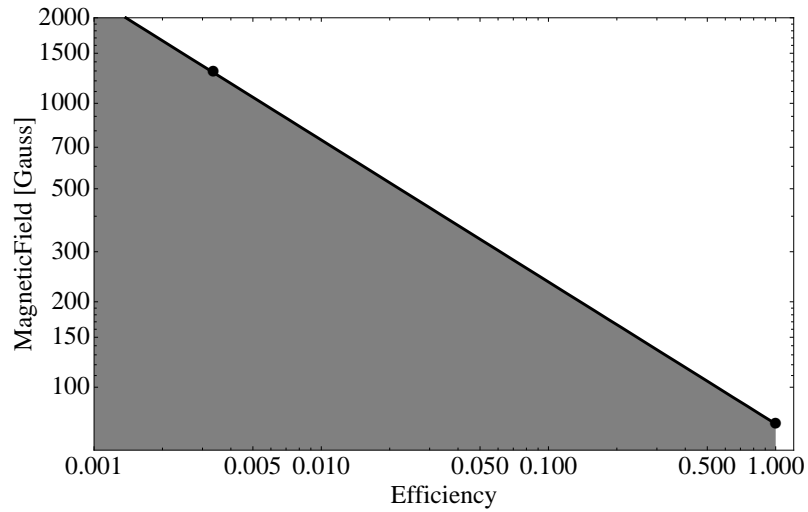


Figure 3.8: Magnetic field intensity versus efficiency of power-to-luminosity conversion; this is derived from Eq. 3.1 for $a = 1$. The shaded area represents the part of the parameter space allowed by the H.E.S.S. upper limit on luminosity. The dots represent two hypothesis: maximum efficiency or equipartition magnetic field.

If the dominant loss is inverse Compton emission, then the maximum energy attained by the accelerated electrons is $E_{e,IC} < 9 \times 10^{14}$ eV.

Also considering a purely hadronic process as p-p interactions, for the production of TeV emission, the energy of the parent particle population will not exceed $E_{p-p} \simeq 10^{13}$ eV.

It can be concluded that this kind of environments cannot be an accelerators of UHECR.

3.5 Conclusions on NGC 1399

Acceleration of charged particles to extremely high energies may take place in SMBH magnetosphere. VHE emission from those SMBH which are low radiating in low-energy band may then be expected either via leptonic or hadronic processes. In order to search this emission the giant elliptical galaxy NGC 1399 was observed by H.E.S.S. in 2005 and 2007. NGC 1399 is not detected in these observations.

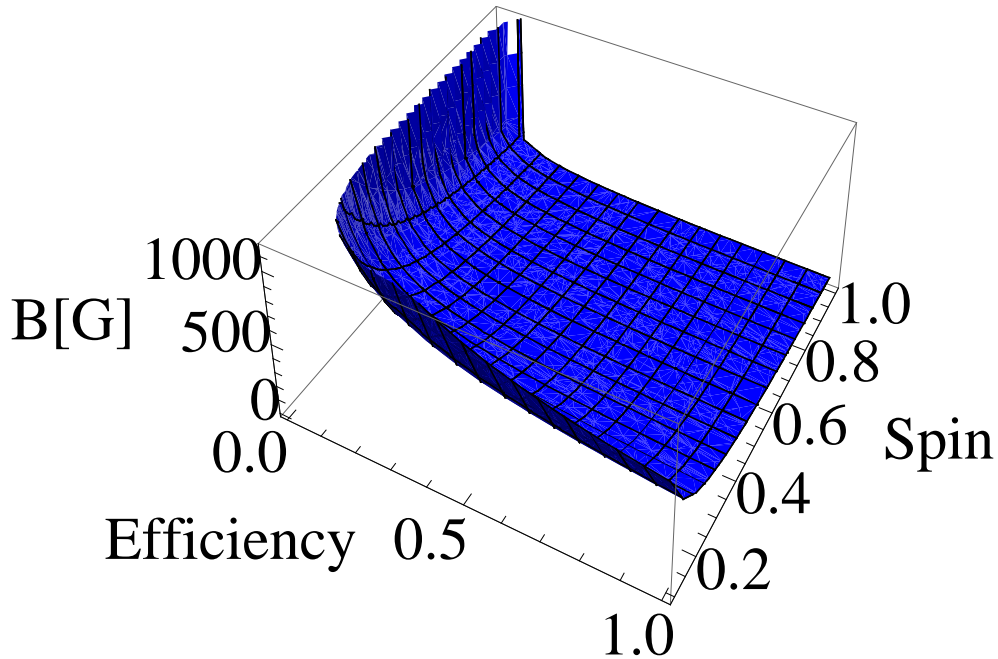


Figure 3.9: Magnetic field intensity versus efficiency of power-to-luminosity conversion versus spin. The part of the parameter space above the plotted curve is not allowed by the result of H.E.S.S. observations.

The non-detection of NGC 1399 gives an upper limit on the value of the circumnuclear magnetic field. The limit on the magnetic field given in Eq. 3.16 comes from the acceleration potential supplied from the spinning SMBH and allows the possibility of VHE emission being produced via proton-proton interactions or IC scattering. It rules out instead curvature emission reaching VHE energies, which require a higher value of the magnetic field. It also rules out the possibility of accelerating UHECR in the system.

The constraint presented here is, to the best of the author knowledge, the tighter one on the value of the magnetic field in the surrounding of a black hole obtained so far.

As NGC 1399 was the best candidate for this kind of study, a drastic improvement in the sensitivity would be required in order to provide tighter constraints on the emission processes and on the strength of the circumnuclear field.

Chapter 4

Stacking Analysis of Passive Systems

As was discussed in the previous chapters, a signal in the VHE domain is expected from passive supermassive black holes. In order to test such predictions the galaxy NGC 1399 was observed, leading to no detection. If there is no variability, a dramatic increment in the livetime of the observations is needed to probe lower fluxes from galaxies candidate to host massive black holes. A stacking analysis is performed using serendipitous data acquired by H.E.S.S. in other extragalactic fields. The results are presented in this Chapter.

4.1 The Motivation for Stacking

Based on published performances of the H.E.S.S. array, the sensitivity scales with the square root of the livetime of the observation (cf Fig. 4.1). The time required to detect a flux f_{expected} is

$$t_{\text{required}} = t_{\text{obs}} \times \left(\frac{f_{\text{obs}}}{f_{\text{expected}}} \right)^2, \quad (4.1)$$

where t_{obs} is the time in which a flux f_{obs} is detected. It can be seen that in order to go deeper in flux by one order of magnitude, the increment in livetime has to be at least of two order of magnitude. Such increment cannot be achieved with

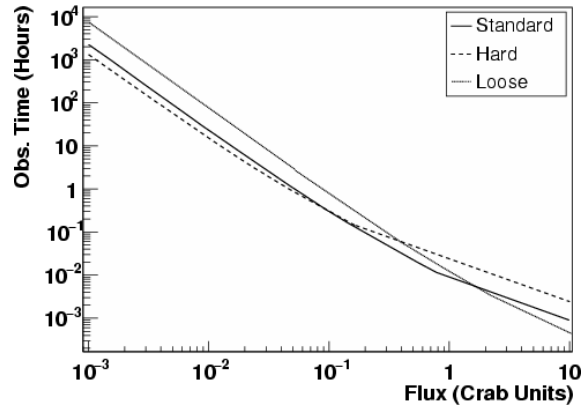


Figure 4.1: From Aharonian et al. (2006b). Sensitivity of the H.E.S.S. array, expressed as the amount of time required to detect a signal at the 5σ level, as a function of the flux of the source, for a source of similar spectral slope to the Crab nebula (for observations at 20° zenith angle, 0.5° offset from the source). Shown are curves for the standard, hard and loose selection cuts.

dedicated observations of a single source but in years. Therefore it is necessary to use a different approach.

A stacking analysis is performed using serendipitous data acquired by H.E.S.S. in the extragalactic fields observed so far. The stacking technique is a standard procedure used to study the statistically averaged properties of a sample of objects whose individual emission would otherwise be below detection threshold. The strength of the method is that the noise of the sample with num objects will be reduced, in comparison to the noise N of the individual source, to N/\sqrt{num} . The stacking method has been applied in different energy bands with rather good outcomes. There are examples from radio astronomy (e.g. White et al., 2007), infrared astronomy (e.g. Dole et al., 2006), X-ray astronomy (e.g. Nandra et al., 2002) and γ -ray astronomy (e.g. Cillis et al., 2004). It is also an interesting method not only for source detection, but also for cosmological studies (see e.g. Cacciato et al., 2009).

4.2 Sample Selection Criteria

The luminosity predicted for a passive SMBH in the VHE band has been presented in Chapter 3:

$$L_\gamma = \xi W_{\max} \sim 10^{45} a^2 (M_9)^2 (B_4)^2 \text{ erg s}^{-1}. \quad (4.2)$$

The first requirement is a high mass of the central black hole in the corresponding galaxy. Therefore large ellipticals are selected from published catalogs. The relevant catalogs will be described case by case in each sample. It has to be noted that the large ellipticals believed to host SMBH are commonly found in the centre of galaxy clusters. Three fields are presented here: the Virgo Cluster field, the Fornax Cluster field and the Coma Cluster field. They are all nearby and rich in large ellipticals.

It is necessary to avoid absorption of a potential emission either by internal or external photon fields (cf. Section 2.4). Thus these objects have to be in the nearby universe, in order to avoid EBL absorption, and to be not surrounded by a strong photon field. It is desirable to select the candidates passive in the NIR (~ 1 eV).

It would be possible also to select the candidates as low luminous in the X-ray domain. The cut on the X-ray luminosity results in a cut in the mass accretion rate: the lower the accretion rate, the smaller will be the contribution of the accretion disk to the absorbing soft photon field. Unfortunately this would also mean that the magnetic energy density transported by the accretion flow would be low, thus reducing the expected luminosity. Because of this argument, two different selection approaches have been used (only in the Virgo field):

- low accreting systems hosting SMBH;
- massive elliptical galaxies hosting SMBH.

4.3 Excess, Significance and Upper Limits

The data were reduced using the standard analysis tools and selection cuts (Aharonian et al. (2006b), standard cuts). The Reflected-Region method (Berge et al., 2007) was used for the estimation of the background. Regions of known VHE γ -ray

emission and regions containing the galaxies in the sample are not considered in the estimation of the background. The significance of an excess for the whole sample is calculated following Eq. 1.2, Li & Ma (1983), knowing the on number of counts N_{ON} and off number of counts N_{OFF} and the parameter α (the ratio between exposure in the ON and OFF region). The number counts N_{ON} are extracted at the galaxy position and the size of the extraction region is 0.11° . If galaxies are closer than 0.2° to each other, only the first encountered galaxy is considered. Indeed, in this case the galaxies are considered independent in position. The samples are usually ordered from the closest to the furthest from the center of the field of view. In the case of no significant excess an upper limit is then calculated using the approach described in Feldman & Cousins (1998), assuming a photon index of $\Gamma=2.6$. Stacked values are derived for the entire sample. The largest amount of observing hours of massive early type galaxies in serendipitous measurements comes from the field observed by H.E.S.S. during the M87 monitoring in the central region of the Virgo cluster (Aharonian et al., 2006a). The livetime relative to each galaxy position is weighted according to the offset from the center of the field of view. The scaling of the livetime follows the scaling of the acceptance of the field (cf. Section 1.2.1).

4.4 The Virgo Sample of Low Accreting SMBH

In the H.E.S.S. field of view centered on the galaxy M87, 8 galaxies hosting low accreting SMBH are present. A system is low accreting whenever its mass accretion rate is smaller than the Eddington limit and it is assumed that a system with a low nuclear X-ray emission hosts a low accreting SMBH. The galaxies are selected from a catalog of low accreting system for which Chandra observations are present (Pellegrini, 2005), along with a catalog of the most massive SMBH (Magorrian et al., 1998). Systems belonging only to the second catalog also present low emission in the X-ray domain. The positions of the galaxies and their parameters are described in Table 4.1. This field was observed for 54 hours (only 4 telescope data until 2008), leading to a total stacked exposure of ~ 250 hours, where the livetime for each position was weighted according to the offset from the center of the field. The testing of

the technical procedure is focusing on this field. The central galaxy, M 87, has been removed from the sample as it is already recognized as a VHE emitter (Aharonian et al., 2006a) where the emitting region might be not directly associated with the central BH.

No excess has been found at the position of any of the single galaxies considered or in the stacked sample. Results for the entire sample are shown in Table 4.2. NGC 4621 was not considered because of its large offset.

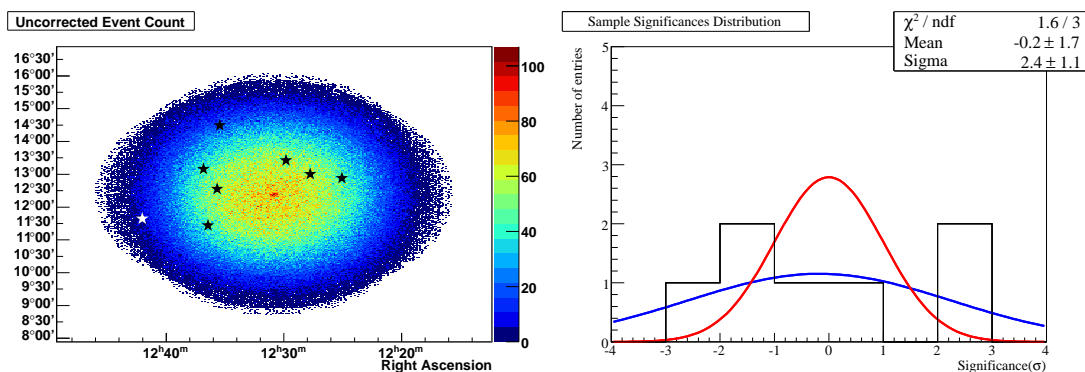


Figure 4.2: **Left:** Position of the galaxies in the field. The leftmost galaxy (NGC4621, white star marker) was not considered because of its large offset. **Right:** Distribution of significances. The blue curve is a gaussian fit to the histogram, while the red curve is the expected distribution of significances for an empty field, for comparison.

The distribution of significances of the sample is not following the expected normal distribution (with zero mean and 1σ , cf Fig. 4.2), but this might just be due to low statistics. Checks on the systematics are presented in Section 4.6.

The stacking procedure can be visualized as the superposition of the same field, but centered on the position of the source candidates. The informations will be obtained from the central bins. For an examples see Fig. 4.3.

From the stacking of the sample results a significance of -0.85σ and an upper limit on the integral flux of $I(> 0.32 \text{ TeV}) < 2.4 \times 10^{-13} \text{ cm}^{-2} \text{ s}^{-1}$ (details in Table 4.2).

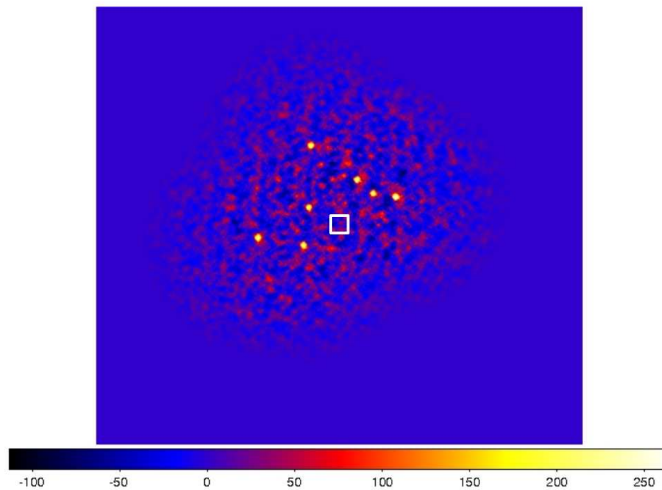


Figure 4.3: Result of the superposition of the Virgo field centered on the position of the galaxy sample (coordinates in Table 4.1). It is possible to see the excess from M87 reproduced 7 times in the field. The informations on the sample are then extracted from the center of the thus obtained field (white square).

4.5 The Cluster Fields of Large Ellipticals: Virgo, Fornax and Coma

4.5.1 The Binggeli Sample in the Virgo Cluster

Large elliptical galaxies (all of the ellipticals not classified as dwarves) were selected in the Virgo cluster field centered on M87. These galaxies have been selected from the Virgo Cluster Catalog (Binggeli, 1985). The distribution of the 16 ellipticals in the field is shown in Fig. 4.4, 9 of which are independent in position. This leads to a total stacked exposure of ~ 400 hours, where the livetime for each position was weighted according to the offset from the center of the field.

Unfortunately no excess has been found at the position of any of the galaxies considered. The distribution of significances presents an apparent shift to negative significances, but this is not significant (the mean is $\sigma_{\text{mean}} = -1.0 \pm 1.2$). Even though the sample is limited, the distribution of significances is consistent with an empty field (cf. Fig. 4.4). From the stacking of the sample results a significance of -2.0σ

and an upper limit on the integral flux of $I(> 0.32 \text{ TeV}) < 1.2 \times 10^{-13} \text{ cm}^{-2} \text{ s}^{-1}$ (details in Table 4.3).

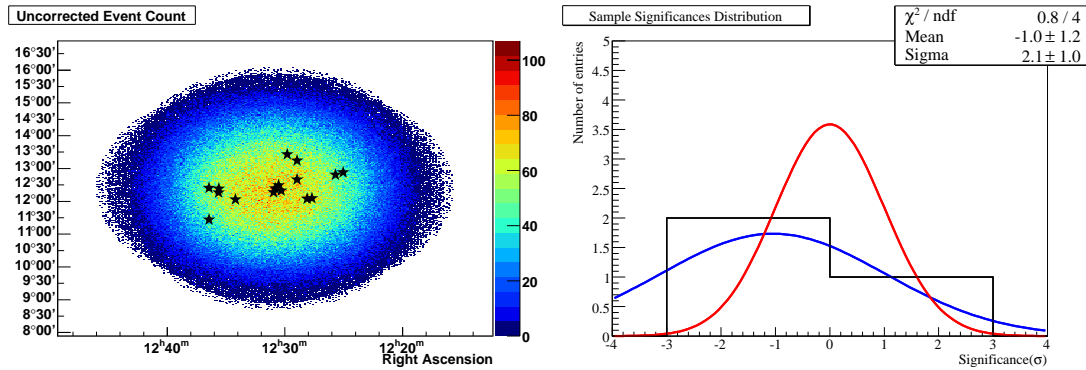


Figure 4.4: **Left:** Position of the galaxies of the Binggeli catalog in the Virgo field (Binggeli, 1985). Only independent galaxies have been considered. **Right:** Distribution of significances for the Virgo sample. The blue curve is a gaussian fit to the histogram, while the red curve is the expected distribution of significances for an empty field, for comparison.

4.5.2 The Pierini Sample in the Coma Cluster

The Coma cluster field was observed for 7.3 hours (only 4 telescope data until 2008) in order to search for point like and diffuse emission in cluster cores (Aharonian et al., 2009d). The distribution of the 37 large elliptical (all of the ellipticals not classified as dwarves) galaxies in the field is shown in Fig. 4.5, 16 of which are independent in position. These galaxies have been selected from the Galaxies morphology Catalog (Pierini et al., 2002). The stacked observation is equivalent to an exposure of ~ 100 hours, where the livetime for each position was weighted according to the offset from the center of the field.

None of the galaxies considered presented a significant excess and the distribution of significances of the sample is consistent with an empty field (cf. Fig. 4.5). From the stacking of the sample results a significance of -0.1σ and an upper limit on the integral flux of $I(> 0.67 \text{ TeV}) < 2.8 \times 10^{-13} \text{ cm}^{-2} \text{ s}^{-1}$ (details in Table 4.4).

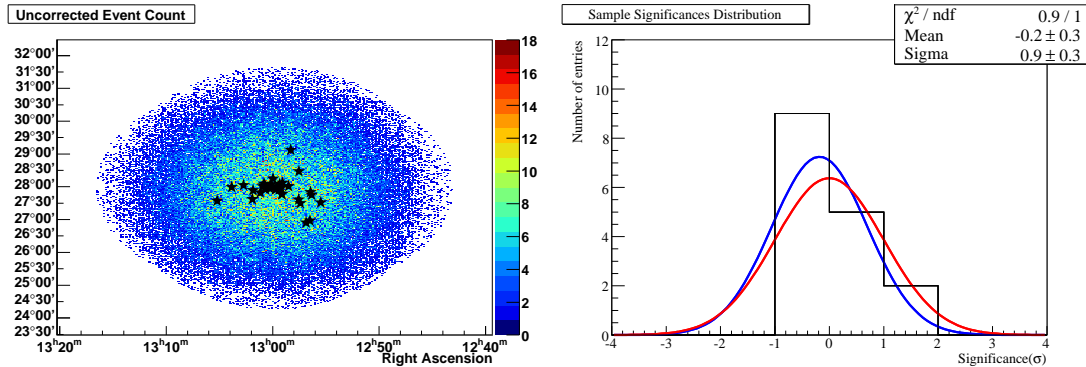


Figure 4.5: **Left:** Position of the galaxies of the Pierini catalog in the Coma field. Only independent galaxies have been considered. **Right:** Distribution of significances for the Coma sample, curves as in Fig. 4.4.

4.5.3 The Ferguson Sample in the Fornax Cluster

The Fornax cluster field was observed for 15 hours (only 4 telescope data until 2008) in order to search for emission from the passive SMBH in NGC 1399 (see Chapter 3). Galaxies in this field have been selected from the Galaxies in Fornax Cluster Catalog (Ferguson, 1989). The distribution of the 10 large elliptical galaxies in the field is shown in Fig. 4.6, 8 of which are independent in position. The stacking analysis corresponds to an exposure of ~ 70 hours, where the livetime for each position was weighted according to the offset from the center of the field. None of the galaxies considered presented a significant excess and the distribution of significances of the sample is consistent with an empty field (cf. Fig. 4.6). From the stacking of the sample results a significance of -0.6σ and an upper limit on the integral flux of $I(> 0.3 \text{ TeV}) < 6.5 \times 10^{-13} \text{ cm}^{-2} \text{ s}^{-1}$ (details in Table 4.5).

4.6 Checks on Statistics of the Fields

In all the cases presented so far, the distribution of significances agrees with the one expected from an empty field although with large uncertainties on the mean and FWHM of the distribution. This is probably due to the very small number of sources in every field. In order to check whether the error is internal to the stacking

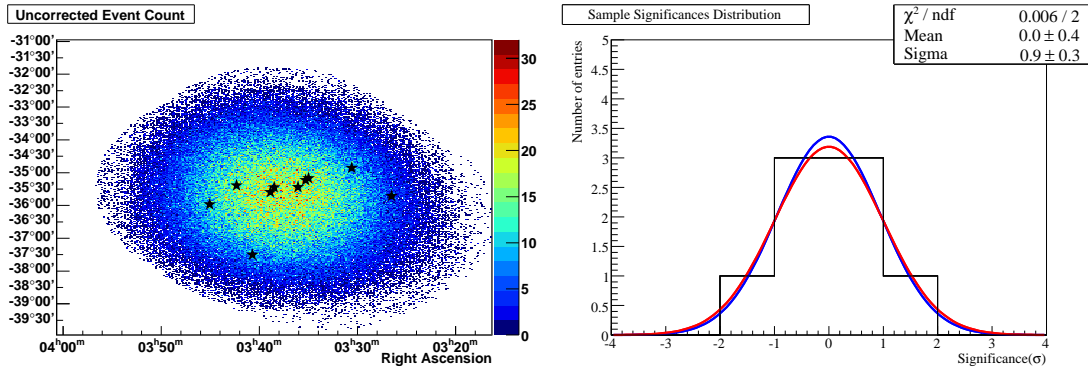


Figure 4.6: **Left:** Position of the galaxies of the Ferguson catalog in the Fornax field. Only independent galaxies have been considered. **Right:** Distribution of significances for the Fornax sample, curves as in Fig. 4.4

procedure or due to low statistics, tests were conducted on samples with increased statistics. The samples are not physically selected, so one expects to reconstruct an empty field distribution of significances. The Virgo field has more observation hours than the others (and also presents the biggest deviation from an empty field hypothesis), therefore it will be used as test field.

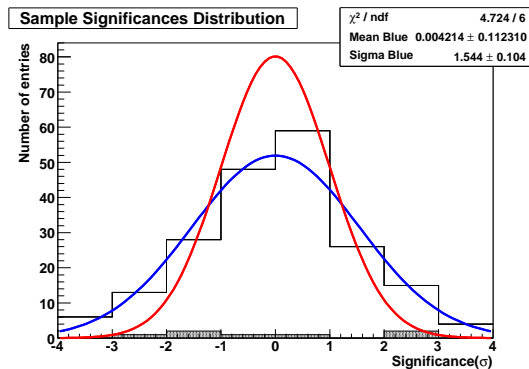


Figure 4.7: Distribution of significances of independent galaxies in the Virgo field. As comparison, overplotted is the distribution of significances of the low accreting systems in the field.

From the Virgo Cluster Catalog (Binggeli, 1985), all the objects with an angular distance from the center of the field $\theta < 2.5^\circ$ were selected. This leads to a sample of 608 objects, but considering only independent positions they are reduced to 204

objects. It can be seen how the distribution of significances resembles the one expected from an empty field (cf Fig. 4.7). However, the best gaussian fit gives a somewhat larger FWHM than expected ($\text{FWHM} > 1$).

In order to check how the FWHM of the gaussian fits changes depending on the sample, some tests are done. The first test will consist in increasing the cut on the angular distance of the inspected position from the center of the field. From Fig. 4.8 it can be seen that the effect becomes smaller and smaller when considering a smaller field of view.

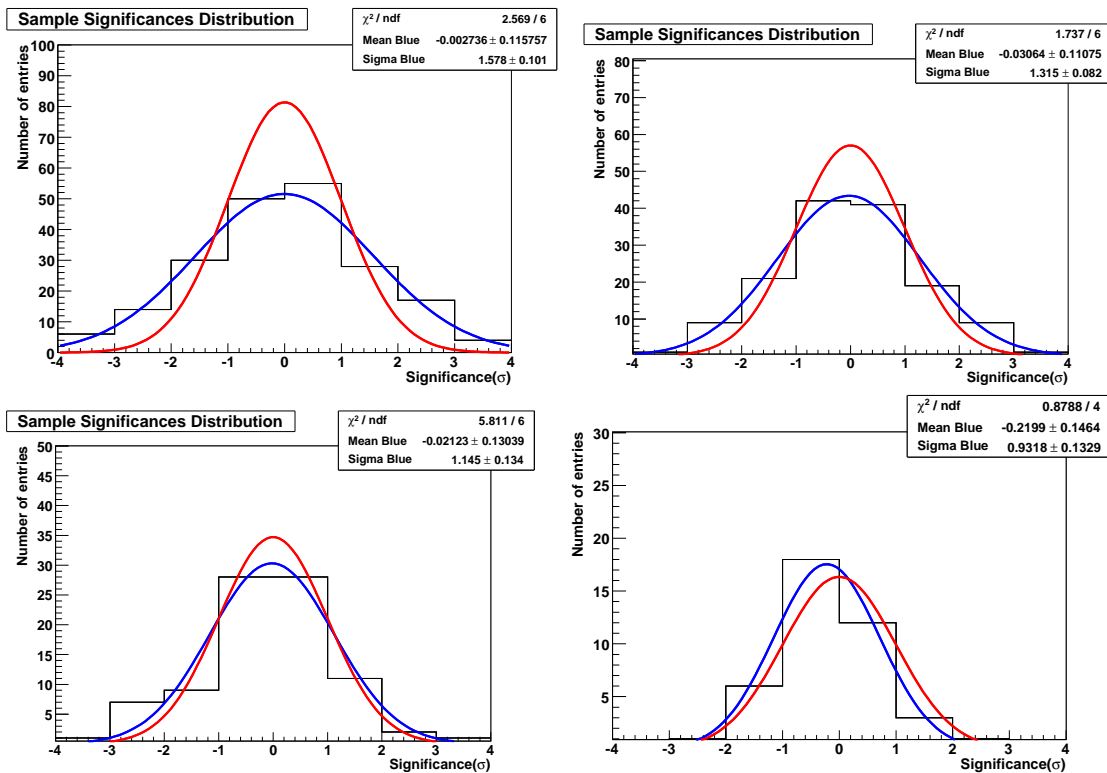


Figure 4.8: Virgo field: $M87 < 2.5^\circ$ (608 objects of which 204 independent); $M87 < 2.0^\circ$ (453 objects of which 143 independent); $M87 < 1.5^\circ$ (306 objects of which 87 independent); $M87 < 1.0^\circ$ (151 objects of which 41 independent)

Another test consists in studying the significance distribution that originates by selecting positions in the sample further away from the center. From Fig. 4.9 it is possible to see that increasing this cut, also the FWHM of the distribution increases.

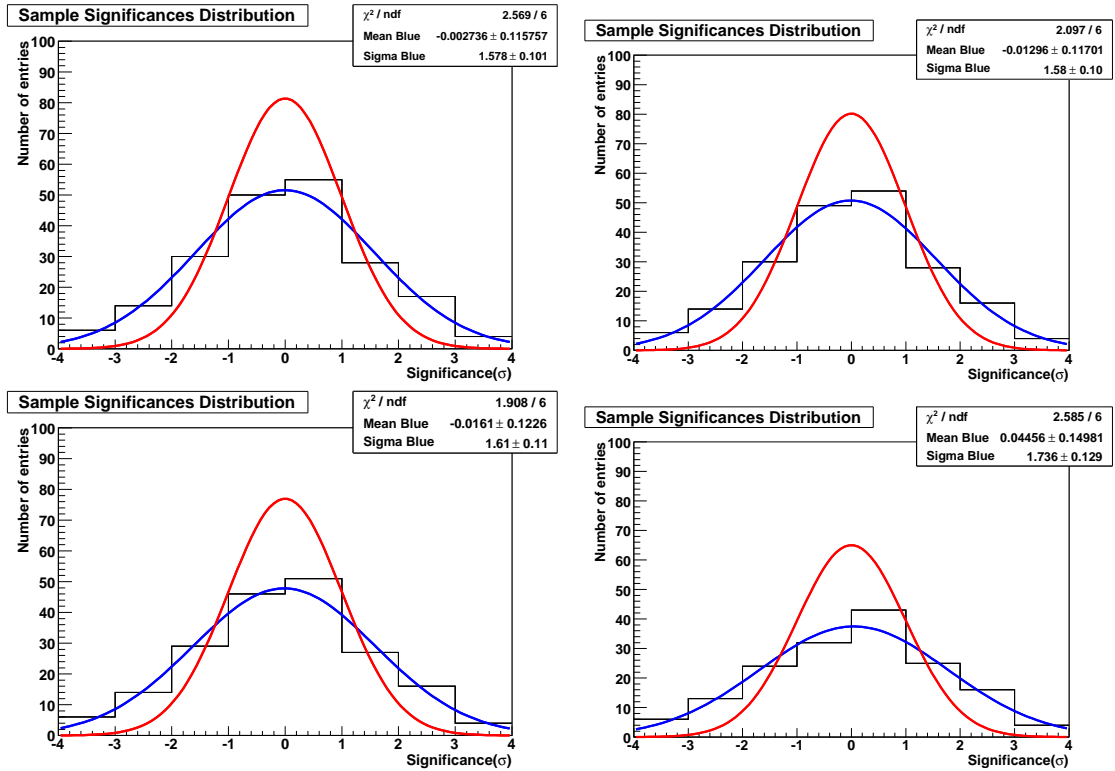


Figure 4.9: Virgo field: $\theta > 0.2^\circ$ (608 objects of which 204 considered); $\theta > 0.3^\circ$ (608 objects of which 201 considered); $\theta > 0.5^\circ$ (608 objects of which 193 considered); $\theta > 1.0^\circ$ (608 objects of which 163 considered).

The same tests were performed in the Fornax field. In Fig. 4.10 is possible to see the outcome (from the Ferguson catalog of galaxies in the Fornax cluster (248 positions, 110 independent) and the Thome catalog of stars (712 positions, 209 independent)). In the case of the Fornax field, the effect is much reduced with respect to what obtained in the Virgo field.

One might then conclude that, in those fields of view with deep exposure, the reconstruction of the acceptance in the outskirts of the field of view deviates from the modelled one. This is not the case in the fields with moderate exposure.

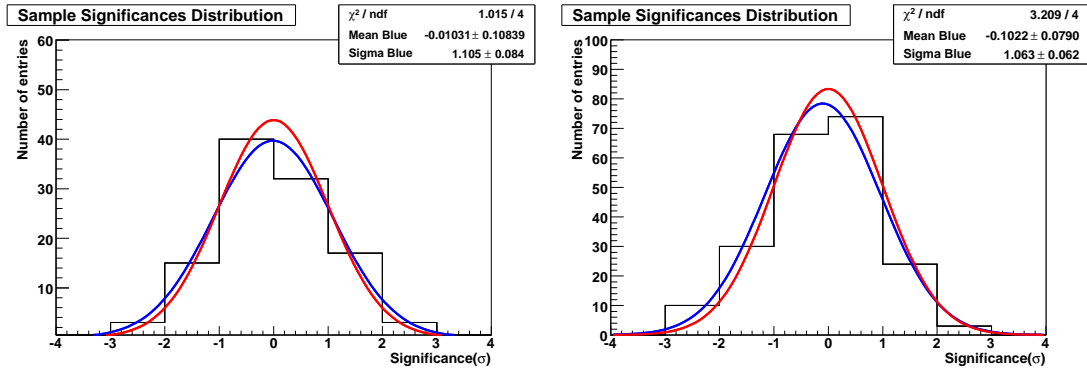


Figure 4.10: Fornax field: Ferguson catalog of galaxies (248 positions, 110 independent) and the Thome catalog of stars (712 positions, 209 independent).

4.7 Implications for UHECR

It can be seen from Fig. 4.11 that the distribution of significances for the three fields presented above is compatible with a gaussian distribution expected from an empty field. Stacking the three samples, weighted for the distance of every field, leads to

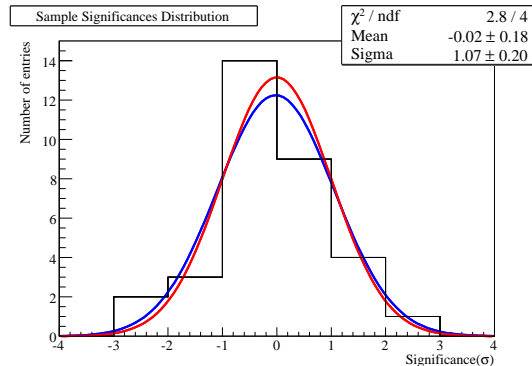


Figure 4.11: Distribution of significances for the 33 galaxies present in the three fields considered above.

an upper limit on the integrated flux of $I(> 0.7 \text{ TeV}) < 1.7 \times 10^{-13} \text{ cm}^{-2}\text{s}^{-1}$.

There have been claims by the Auger collaboration of correlation between Ultra High Energy Cosmic Rays arrival direction and AGN spatial distribution Abraham et al (2007a). The claim is dubious, as shown in Section 2.1.2, however AGN are among the sources that can indeed accelerate particles to UHE (cf. Section 2.1.1

and Hillas (1984)). If this conjecture is correct one would then expect VHE γ -ray emission associated with galactic nuclei. The stacking analysis presented here can therefore be used to constrain this hypothesis. Knowing the stacked γ -ray luminosity allows to estimate the typical luminosity of a UHECR emitter and the relative CR density.

If therefore one assumes that the large ellipticals of the samples investigated here could be related to UHECR acceleration, one would need to conclude that the associate γ -ray luminosity (in the energy range $E = (0.7 - 100)$ TeV) is small, of the order of

$$L_{\gamma} \sim 1.41 \times 10^{41} \left(\frac{D}{50 \text{Mpc}} \right)^2 \text{ erg s}^{-1},$$

where $D = 50$ Mpc has been chosen as the distance of the putative emitter.

4.8 Conclusions

VHE emission is expected from the vicinity of SMBH present at the center of spheroidal galaxies. Data acquired by the H.E.S.S. system of telescopes in the Virgo, Coma and Fornax cluster field have been used in order to detect such signal. No excess has been found at the position of any of the galaxies considered. Moreover a stacking analysis has been performed on the entire sample, resulting in no excess. Assuming that the three samples are homogeneous a part from the distance D to the observer, stacking all the three fields results in a final upper limit of $I(> 0.7 \text{ TeV}) < 1.7 \times 10^{-13} \text{ cm}^{-2}\text{s}^{-1}$ for 33 galaxies. This is consistent with the scaling of sensitivity with time Aharonian et al. (2006b).

GALAXY	RA	DEC	M_{BH}/M_{\odot}	DIST (Mpc)	OFFSET	LIVETIME (hrs)
NGC 4374	12h25m03.74s	+12d53'13.14"	1.6×10^9	18.4	1.55	35.7
NGC 4438	12h27m45.91s	+13d0'32.3"	5.0×10^7	16.1	1.07	47.6
NGC 4473	12h29m48.95s	+13d25'46.1"	3.4×10^8	15.8	1.15	46.3
NGC 4548	12h35m26.58s	+14d29'45.1"	2.8×10^7	19.2	2.43	11.9
NGC 4552	12h35m40s	+12d33'22.9"	4.65×10^8	15.3	1.27	42.7
NGC 4564	12h36m27.01s	+11d26'18.8"	2.53×10^8	15.3	1.71	31.4
NGC 4569	12h36m50.08s	+13d09'45.7"	1.2×10^8	16.8	1.72	31.7
NGC 4621	12h42m2.39s	+11d38'45.1"	2.8×10^8	15.3	2.8	/
ALL						247
NGC 1399	3h38m29.32s	-35d45'0.7"	1.06×10^9	20.3		18.1

Table 4.1: Characteristics of the sample of low accreting systems in the Virgo field

N_{OFF}	N_{OFF}	α (α_{range})	EXCESS	SIGNIFICANCE	LIVETIME hours	THRESHOLD TeV	UPPER LIMIT $\text{cm}^{-2} \text{s}^{-1}$ (% C.F)
13906	475664	0.03 (0.02÷0.04)	-101	-0.85σ	247	0.32	2.4×10^{-13} (0.19)

Table 4.2: Results for the entire sample of passive black holes selected as low luminous in X-ray.

N_{ON}	N_{OFF}	α (α_{range})	EXCESS	SIGNIFICANCE	LIVETIME hours	THRESHOLD TeV	UPPER LIMIT $\text{cm}^{-2} \text{s}^{-1}$ (% C.U.)
22126	578850	0.04 (0.02÷0.06)	-311	-2.0σ	398.3	0.32	1.2×10^{-13} (0.1)

Table 4.3: Stacking results for the Virgo sample. Given are also the range of alpha in the sample. The percentage of the Crab flux (C.U) is calculated above the same threshold.

N_{ON}	N_{OFF}	α (α_{range})	EXCESS	SIGNIFICANCE	LIVETIME hours	THRESHOLD TeV	UPPER LIMIT $\text{cm}^{-2} \text{s}^{-1}$ (% C.U.)
4350	59864	0.07 (0.05÷0.15)	-9.9	-0.1σ	104.1	0.67	2.8×10^{-13} (0.7)

Table 4.4: Stacking results for the Coma sample. Quantities as in Table 4.3.

N_{ON}	N_{OFF}	α (α_{range})	EXCESS	SIGNIFICANCE	LIVETIME hours	THRESHOLD TeV	UPPER LIMIT $\text{cm}^{-2} \text{s}^{-1}$ (% C.U.)
3856	94683	0.04 (0.02÷0.07)	-36	-0.6σ	74.7	0.3	6.5×10^{-13} (0.5)

Table 4.5: Stacking results for the Fornax sample. Quantities as in Table 4.3.

Chapter 5

Detailed Estimate of VHE Emission from Passive SMBH

From studies in the literature, passive systems hosting SMBH are candidate for emission in the VHE domain. Models are discussed and tested in the previous chapters. From H.E.S.S. observations only upper limits have been obtained. It follows that the assumptions in the models explored so far are not fulfilled. Relying on the same acceleration models described in Chapter 2, a more detailed estimation of the radiative power and of the expected energy regime reached by the radiation losses is pursued. The estimates are then compared with the expected sensitivity of the next generation of facilities for γ -ray astronomy.

5.1 Estimating the Magnetic Field Intensity from the Disk-Magnetosphere Connection

H.E.S.S. observation of the passive SMBH in NGC1399 demonstrated that the estimate of Eq. 3.3 ($B \sim 10^3$ Gauss) is not correct. In Chapter 3, the magnetic field intensity was estimated from equipartition among magnetic energy density and accreted gas energy density. The equipartition value can be obtained from

$$\frac{B^2}{8\pi} = \gamma m_e n_e c^2 + m_p n_p c^2, \quad (5.1)$$

where n_e is the electron number density and the proton number density $n_p = n_e/1.2$. If one assumes that the electrons are mildly relativistic $\gamma \sim 1$, then the protons are dominating the energy budget. Plasma densities in the surrounding of SMBH are of the order of $\sim 10^7 \text{cm}^{-3}$.

5.1.1 The Relation between Magnetic Field and Angular Momentum

The first tenet is that the energy of the magnetic field has to originate, in one way or another, from the kinetic energy of the accreting flow. A non-charged rotating black hole cannot sustain a magnetic field on its own (Thorne, Price & Macdonald, 1986). It has thus to be understood the connection between the magnetic field on the magnetosphere of an accreting black hole and the magnetic field at the innermost stable orbit of its accretion disk $B(r_i)$.

Similar to (Kuncic & Bicknell, 2004) the starting point is the equation of the angular momentum in cylindrical coordinates (r, ϕ, z) . The azimuthal component of the momentum conservation equation (Eq. 60 in Kuncic & Bicknell (2004)) is integrated over z and the mass continuity equation (Eq. 38 in Kuncic & Bicknell (2004)) is applied, resulting in:

$$\frac{d}{dr} \left[\dot{M}_a v_\phi r + 2\pi r^2 \int_{-h}^h t_{r\phi} dz \right] = v_\phi r \frac{d\dot{M}_a}{dr} - 4\pi r^2 t_{\phi z}, \quad (5.2)$$

where \dot{M}_a is the mass accretion rate (in g s^{-1}), v_ϕ is the azimuthal component of fluid velocity in the disk, h is the height of the disk and t_{ij} is the magnetic stress tensor, defined as:

$$t_{ij}^B = \frac{B_i B_j}{4\pi} - \delta_{ij} \frac{B^2}{8\pi}. \quad (5.3)$$

The Eq. 5.2 can undergo several simplifications:

- constant mass accretion rate $d\dot{M}_a/dr = 0$;
- $rt_{\phi z} \ll ht_{r\phi}$.

The second condition is only valid in the inner part of the disk, where its height is not negligible if compared to r . Therefore Eq. 5.2 becomes

$$\dot{M}_a v_\phi r + 2\pi r^2 \int_{-h}^h t_{r\phi} dz = \text{const.} \quad (5.4)$$

To estimate the constant, $T_{r\phi}(r_i) = \int_{-h}^h \frac{B_r(r_i)B_\phi(r_i)}{4\pi} dz = 0$ is assumed at the innermost stable orbit, resulting in $\text{const} = \dot{M}_a v_\phi(r_i) r_i$. For convenience the radius is normalized to the gravitational radius $r_g = GM_{\text{BH}}/c^2$, $x = r/r_g$. From

$$T_{r\phi}(x) = -\frac{(GM)^{1/2} \dot{M}_a}{2\pi} \left(\frac{GM}{c^2}\right)^{-3/2} x^{-3/2} \left[1 - \left(\sqrt{\frac{x_i}{x}}\right)\right], \quad (5.5)$$

and from the definition of the integrated stress tensor

$$T_{r\phi}(x) = \int_{-h}^h \frac{B_r(x)B_\phi(x)}{4\pi} dz \sim \frac{B_r(x)B_\phi(x)}{4\pi} 2h, \quad (5.6)$$

the magnetic field intensity can be expressed as

$$B_r(x)B_\phi(x) = \frac{\dot{M}_a c^3}{GM_{\text{BH}}} h^{-1} x^{-3/2} \left[1 - \left(\frac{x_i}{x}\right)^{1/2}\right]. \quad (5.7)$$

Therefore to estimate the magnetic field the height of the disk has to be included. In the internal regions of the accretion disk the radiation pressure is dominating over the gas pressure. The disk height can be written as (from Padmanabhan (2001)):

$$h(x) = 0.75 \frac{\dot{M}_a c^2}{L_{\text{Edd}}} (2r_g) \left[1 - \sqrt{1 - \frac{x_i}{x}}\right], \quad (5.8)$$

where L_{Edd} is the Eddington luminosity. The behavior of the magnetic field intensity as a function of radius is shown in Fig. 5.1. It has to be kept in mind that the second assumption, $rt_{\phi z} \ll ht_{r\phi}$, could be not fulfilled. In that case, it is possible to estimate the $B_\phi(x)B_z(x)$ component of the stress tensor:

$$B_\phi(x)B_z(x) = \frac{\dot{M}_a c^5}{2} (GM_{\text{BH}})^{-2} x^{-5/2}. \quad (5.9)$$

The behavior of the magnetic field intensity as a function of radius in this case is shown in Fig. 5.2. In the limiting case in which $r \sim h$ (believed to be true in case of low accreting sources with optically thin disks), the two estimates in Eq. 5.7 and Eq. 5.9 coincides. Therefore $\sqrt{B_\phi(x)B_z(x)}$ will be used in the following to estimate the magnetic field.

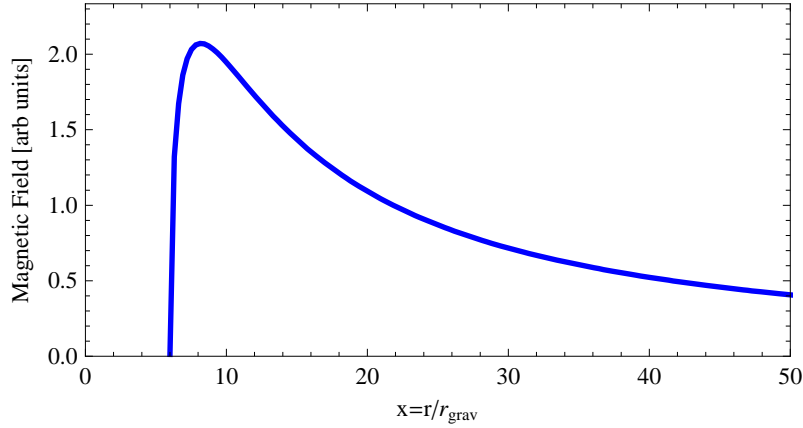


Figure 5.1: Behavior of the magnetic field intensity $\sqrt{B_r(x)B_\phi(x)}$ in the internal regions of the accretion disk, where the radiation pressure is dominating.

5.1.2 The Dependency on the Mass Accretion Rate and Jet Power

The determination of the intensity of the magnetic field, as described above, depends on the value of the accretion rate. This parameter can be obtained in two ways: relating it to X-ray-derived plasma quantities (density ρ_∞ and sound speed $c_{S\infty}$ at infinity); relating it to the power of the jet P_{jet} .

From the classical Bondi accretion theory:

$$\dot{m} = \frac{\dot{M}_a c^2}{L_{\text{Edd}}} = \pi G^2 M_{\text{BH}}^2 \frac{\rho_\infty}{c_{S\infty}^3} \left(\frac{2}{5 - 3\gamma} \right)^{\frac{5-3\gamma}{2(\gamma-1)}}, \quad (5.10)$$

where γ is the polytropic index. From Bicknell & Li (2007)

$$\dot{m} = \frac{\dot{M}_a c^2}{L_{\text{Edd}}} = \frac{4P_{\text{jet}}}{L_{\text{Edd}}} \left(\frac{r_{\text{in}}}{r_g} \right) \left(1 - \frac{r_{\text{in}}}{r_{\text{out}}} \right)^{-1}, \quad (5.11)$$

where r_{in} and r_{out} are the inner and outer radius of the jet at its base, respectively. The second estimate is the one that will be used in the following. It is indeed more closely related to the amount of matter that actually reaches the surroundings of the BH without being blown away by winds. Knowing the power of the jet thus means knowing the mass accretion rate.

The power of the jet P_{jet} can be estimated from Bicknell et al. (1997), solving

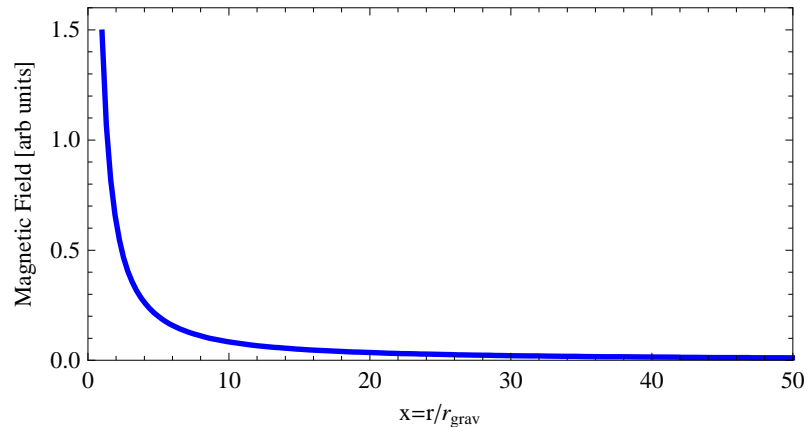


Figure 5.2: Behavior of the magnetic field intensity $\sqrt{B_\phi(x)B_z(x)}$ in the internal regions of the accretion disk, where the radiation pressure is dominating.

the following set of 2 equations in 2 variables.

$$\xi = \frac{(5 - \delta)^3 \zeta^2}{18\pi(8 - \delta)} \left(\frac{P_{jet} t^3}{\rho_0 x_0^5} \right) \quad (5.12)$$

$$P_0(t) = \frac{9}{\zeta(5 - \delta)^2} \rho_0 \left(\frac{x_0}{t} \right), \quad (5.13)$$

where $x_0 = x_h \xi^{1/(\delta-5)}$ and the pressure $P_0 = P_C \xi^{(2-\delta)/(\delta-5)}$. The ratio between the pressure in the hotspot region is ζ times the average lobe pressure and δ is the index of the density distribution. The jet power P_{jet} can thus be estimated knowing the extension x_h of the jet, the non-thermal pressure of the jet P_C and the density of the ambient gas ρ_0 at a fiducial radius x_0 . This estimate is based on a quite firm knowledge of the properties of the jet and on the assumption that the jet is powerful enough to form a bow shock in the termination and to have an hotspot region. This is not often the case in the low luminous sources considered in this work.

An alternative is to estimate the jet power making use of X-ray observations. In this way is possible to resolve the X-ray cavities blown by low power jets. From (Allen et al., 2006)

$$P_{jet} = \frac{4}{3} \frac{\pi}{\gamma - 1} c_s^3 r_w^3 \rho \frac{r_l}{R_c}, \quad (5.14)$$

where the sound speed c_s and the density ρ come from X-ray observations. From X-ray imaging one can derive the length and width of the cavity (r_l and r_w) and

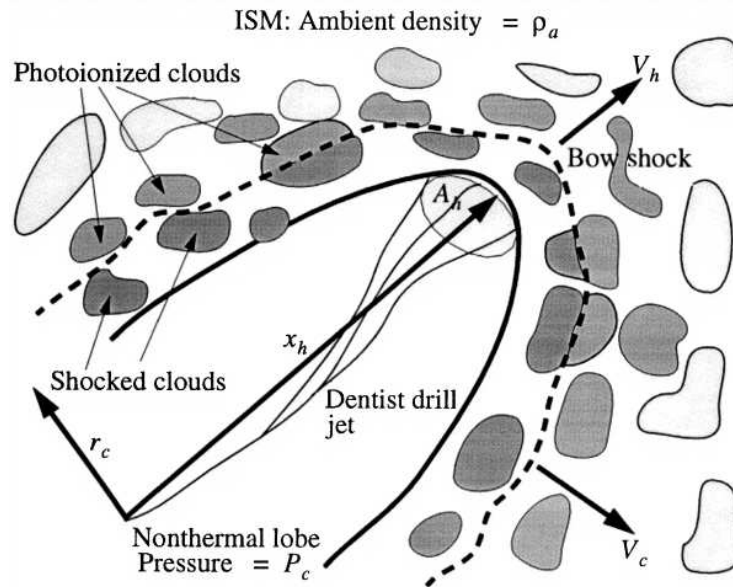


Figure 5.3: From Bicknell et al. (1997), sketch of the configuration. The extension of the jet x_h , the pressure of the lobe P_C and the ambient gas density have to be known in order to estimate the power of the jet P_{jet}

the distance of the cavity from the central BH. In the case of NGC 1399, the two methods for jet power estimation agree but for a factor 2.

5.2 Flux Predictions

One can estimate the gamma luminosity as a part of the total power available from a spinning SMBH:

$$L_\gamma = \xi W_{\max} \sim 10^{45} a^2 (M_9)^2 (B_4)^2 \text{ erg s}^{-1}. \quad (5.15)$$

5.2.1 Curvature Emission and Synchrotron Emission Spectrum from Accelerated Protons and Electrons

If particles are accelerated along the magnetic field lines, the primary radiative loss is curvature emission. From (Berezinskii et al, 1990), the radiation spectrum of curvature emission for a single particle (with Lorentz factor γ) as a function of

frequency ν assumes the form:

$$P(\nu) = \frac{\sqrt{3}q^2}{2\pi R_{\text{curv}}} \gamma \left(\frac{\nu}{\nu_c} \right) \int_{\nu/\nu_c}^{\infty} K_{5/3}(\eta) d\eta, \quad (5.16)$$

where q is the particle charge, R_{curv} is the radius of curvature of the magnetic field lines, $K_{5/3}$ is the modified Bessel function of the second kind and the critical frequency ν_c is:

$$\nu_c = \frac{3}{4\pi} \frac{c}{R_{\text{curv}}} \gamma^3. \quad (5.17)$$

The function $\left(\frac{\nu}{\nu_c} \right) \int_{\nu/\nu_c}^{\infty} K_{5/3}(\eta) d\eta$ is plotted in Fig. 5.4. The total energy loss

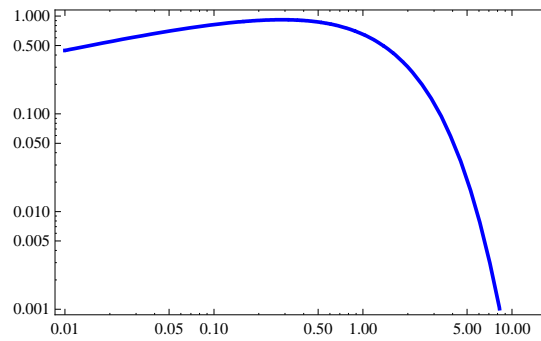


Figure 5.4: $\left(\frac{\nu}{\nu_c} \right) \int_{\nu/\nu_c}^{\infty} K_{5/3}(\eta) d\eta$

integrated in all frequency is

$$\dot{E}_{\text{curv}} = -\frac{2}{3} \frac{q^2 c}{R_{\text{curv}}} \left(\frac{E}{mc^2} \right)^4. \quad (5.18)$$

Equating Eq. 5.18 with the maximum energy gain $\dot{E}_{\text{gain}} = \eta q B c$, the maximum energy for accelerated particle limited by curvature losses is

$$E_{\text{part,curv}} = \left(\frac{3\eta B R_{\text{curv}}^2}{2q} \right)^{1/4} m_{\text{part}} c^2. \quad (5.19)$$

The emission spectrum for a proton of such energy is shown in Fig. 5.5. Using the variable $\nu/\nu_c = x$, it is possible to rewrite all the above equations, especially from Eq. 5.17 will follow

$$x^{-1} = \frac{3}{4\pi} \frac{q^2}{R_{\text{curv}}} \gamma^3 \nu^{-1} \Rightarrow d\gamma = -\frac{1}{3} \left(\frac{4\pi R_{\text{curv}}}{3c} \right)^{1/3} \nu^{1/3} x^{-4/3} dx. \quad (5.20)$$

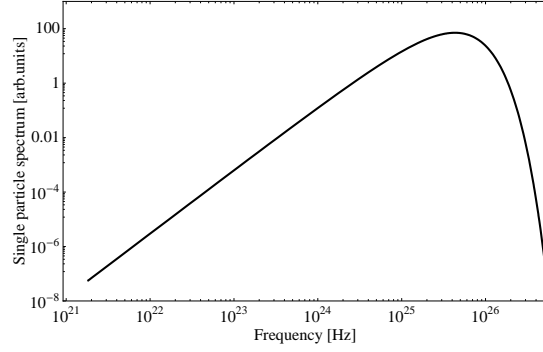


Figure 5.5: Radiation spectrum of a proton of maximum energy in case of curvature losses dominating.

If the distribution of particles follows

$$N(\gamma) = K\gamma^{-a}, \quad (5.21)$$

where K has the dimensions of a number density, then the emissivity is calculated as

$$\begin{aligned} j(\nu) &= \int_{\gamma_1}^{\gamma_2} P(\nu) N(\gamma) d\gamma \\ &= \int_{x_2}^{x_1} dx K \frac{\sqrt{3}q^2}{6\pi R_{\text{curv}}} \left(\frac{4\pi R_{\text{curv}}}{3c} \right)^{\frac{2-a}{3}} \nu^{\frac{2-a}{3}} x^{\frac{a-2}{3}} \int_x^{\infty} K_{5/3}(\eta) d\eta. \end{aligned} \quad (5.22)$$

This is a power-law $j(\nu) \approx \nu^{\frac{2-a}{3}}$. Integrating in the volume, the luminosity per unit frequency is $L(\nu) = \int dV j(\nu)$. The volume is assumed to be a sphere of radius $r = GM_{\text{BH}}/c^2$. The flux per unit frequency will be $f(\nu) = L(\nu)/(4\pi D^2)$, where D is the distance of the source.

The next step is estimate the parameter K . It is possible to calculate the total plasma energy density from $\int_{\gamma_1}^{\gamma_2} N(\gamma) \times \gamma mc^2 = \beta B^2/8\pi$, where the parameter β represents the ratio between gas pressure and magnetic pressure. The parameter K can be calculated also starting from associating a certain fraction of the available power to the resulting emission:

$$\int_{\nu_2}^{\nu_1} L(\nu) = L_\gamma = \xi W_{\text{max}}. \quad (5.23)$$

In the following the latter approach will be used to obtain estimates for emission. For $\xi = 1$ and integration in a range of frequency $\nu = [10^{-5}\nu_c, 10^5\nu_c]$, $K \sim 10^9 \text{cm}^{-3}$. In the Section 5.3.1 the predictions for several objects will be presented.

If there is a component of the magnetic field transversal with respect to the particle trajectories, synchrotron losses would dominate over curvature losses. The frequency spectrum of synchrotron emission assumes the following form, from (Berezinskii et al, 1990):

$$P(\nu) = \frac{\sqrt{3}q^3}{m_{\text{part}}c^2} B \left(\frac{\nu}{\nu_c} \right) \int_{\nu/\nu_c}^{\infty} K_{5/3}(\eta) d\eta. \quad (5.24)$$

The critical frequency is:

$$\nu_c = \frac{3}{4\pi} \frac{qB}{m_{\text{part}}c} \gamma^2 \quad (5.25)$$

and the distribution of particles is assumed to be the same considered in the curvature case,

$$N(\gamma) = K\gamma^{-a}, \quad (5.26)$$

and the emissivity is

$$j(\nu) = \int_{\gamma_1}^{\gamma_2} P(\nu) N(\gamma) d\gamma. \quad (5.27)$$

In analogy with the treatment of curvature emission:

$$x^{-1} = \frac{3}{4\pi} \frac{qB}{m_{\text{part}}c} \gamma^2 \nu^{-1} \Rightarrow d\gamma = -\frac{1}{2} \sqrt{\frac{4\pi m_{\text{part}}c}{3qB}} \sqrt{\nu} x^{-3/2} \quad (5.28)$$

Therefore the emissivity will read

$$j(\nu) = \int_{x_2}^{x_1} dx K \frac{\sqrt{3}q^3}{2m_{\text{part}}c^2} B \left(\frac{4\pi m_{\text{part}}c}{3qB} \right)^{\frac{1-a}{2}} \nu^{\frac{1-a}{2}} x^{\frac{a-1}{2}} \int_{\nu/\nu_c}^{\infty} K_{5/3}(\eta) d\eta \quad (5.29)$$

This is a power-law $j(\nu) \approx \nu^{\frac{1-a}{2}}$.

Predictions are presented in the Section 5.3.1. It has to be reminded that the synchrotron emission suffers from an intrinsic cut-off that does not depend on the magnetic field, but only on physical constants (cf. 2.3.1):

$$E_{\text{part, cut-off}} = \frac{9}{4\alpha_f \eta} m_{\text{part}} c^2. \quad (5.30)$$

5.3 Impact for the Next Generation of γ -ray Observatories

In the previous sections a detailed estimate for the expected emission from passive systems hosting SMBH was presented. In the following, predictions for three objects of particular interest are drawn. The predictions are then confronted with the expected sensitivity of the next generation of γ -ray observatories. As an example, the expected sensitivity for the forthcoming Cherenkov Telescope Array (CTA) is shown, adapted from simulations of possible configurations (Bernlöhr, 2008). In addition, also the sensitivity of the LAT instrument on board of the Fermi satellite are shown¹. The two facilities are chosen because they are or will be the most sensitive instruments in the respective energy band.

5.3.1 Examples: NGC 1399, M87, SgrA*

The resulting spectra for three test objects are presented. First of all, it is mandatory to check the prediction for NGC 1399, the test galaxy observed by H.E.S.S. and whose observations were presented in Chapter 3. Another interesting object is the radio galaxy M87. As described before, this galaxy was detected in the VHE regime, but the nature of the emission and the location of the emitting region are still unclear (Aharonian et al., 2006a). Also the nucleus of the Milky Way Galaxy was detected in the VHE band (Aharonian et al., 2009c). Up to date, there is no consensus on the origin of this emission, but it might be associated with the central black hole, SgrA*.

Two commonly observed distribution are considered:

- a truncated power-law

$$N(\gamma) = K\gamma^{-a}d\gamma, \gamma < \gamma_0;$$

- a power-law with exponential cut-off

$$N(\gamma) = K\gamma^{-a}e^{-\gamma/\gamma_0}d\gamma.$$

¹http://www-glast.slac.stanford.edu/software/IS/glast_lat_performance.htm

For the curvature emission and for both explored particle distribution the limiting energy, γ_0 , will be given by Eq. 5.19. For a distribution of particles following a power-law with exponential cut-off the emissivity will be

$$j(\nu) = \int_{x_2}^{x_1} dx K \frac{\sqrt{3}q^2}{6\pi R_{\text{curv}}} \left(\frac{4\pi R_{\text{curv}}}{3c} \right)^{\frac{2-a}{3}} \nu^{\frac{2-a}{3}} x^{\frac{a-2}{3}} e^{-(x/x_0)^{1/3}} \int_x^\infty K_{5/3}(\eta) d\eta, \quad (5.31)$$

while for the truncated power-law the emissivity is described in Eq. 5.22. The resulting spectra are normalized to the power given by Eq. 5.15. Other important quantities are summarized in Table 5.1. The spectra are presented in the range

Galactic Nuclei	M_{BH} M_\odot	Mass accretion rate \dot{m}	Magnetic Field Gauss	power-law index
NGC 1399	1.06×10^9	6×10^{-4}	40	2.5
M 87	3.0×10^9	1×10^{-2}	80	2.5
SgrA*	3.6×10^6	1.5×10^{-3}	15	2.5

Table 5.1: Parameters used for the derivation of the spectra.

$\nu \in [10^{-4}\nu_c, 10^4\nu_c]$, where ν_c is the critical frequency relative to the cut-off energy.

The level of VHE emission predicted for NGC 1399 would be lower than the expected sensitivity of the next generation of Cherenkov telescopes even for maximum efficiency of power-to-luminosity conversion $\xi = 1$ (cf. Fig. 5.6).

As can be seen from Fig. 5.7, curvature emission in the case of M87 can reach the VHE domain and the fluxes that were indeed detected with the H.E.S.S. array. The proper reproduction of the observed spectrum depends however on the spectral index of the particle distribution.

From Fig. 5.8 is possible to see that curvature emission from the vicinity of the supermassive black hole at the center of our galaxy, SgrA*, does not seem to be feasible. Indeed, in order to fit the the expected energy range and flux, the magnetic field should be of the order of $B \sim 10^4$ Gauss (shown in Fig.5.9).

From Fig. 5.10 it can be seen that synchrotron emission, due to the intrinsic cut-off described in Eq. 5.30, cannot reach the VHE domain and has thus not been investigated further. However, in case of beaming of the emission, also synchrotron emission should play a role.

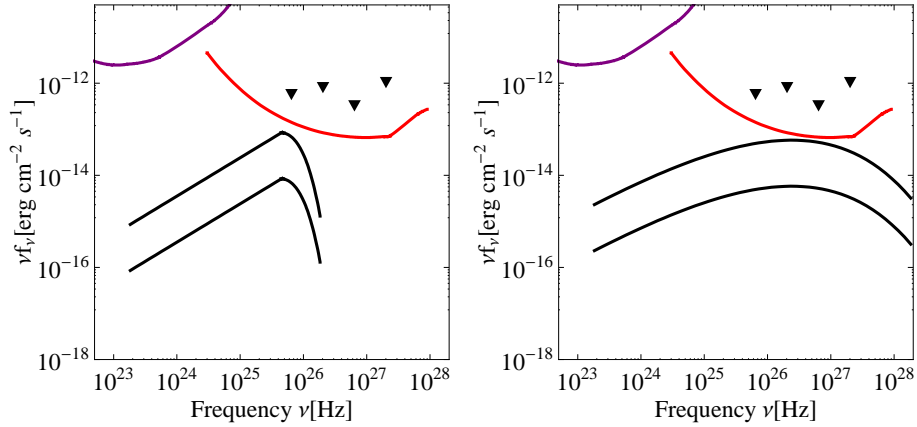


Figure 5.6: Predicted curvature emission for NGC 1399, truncated power-law particle distribution (left) and power-law with exponential cut-off (right). Black solid curves are for efficiency of power-to-luminosity conversion $\xi = 1$ and $\xi = 0.1$ respectively. Purple solid curve is the sensitivity of the LAT instrument on board of the Fermi space telescope for 1 year integration. The red solid curve is the expected CTA sensitivity for a 5σ detection in 50 hours. The black triangles represent the H.E.S.S. upper limits on the object as presented in Chapter 3.

It has to be noted that none the spectra shown here, for any considered object, would be detectable by the LAT instrument in 1 year of integration. Therefore it is not surprising that NGC 1399 did not appear in the Fermi Bright Source list (list of sources with a statistical significance $> 10\sigma$, Abdo et al. (2009)).

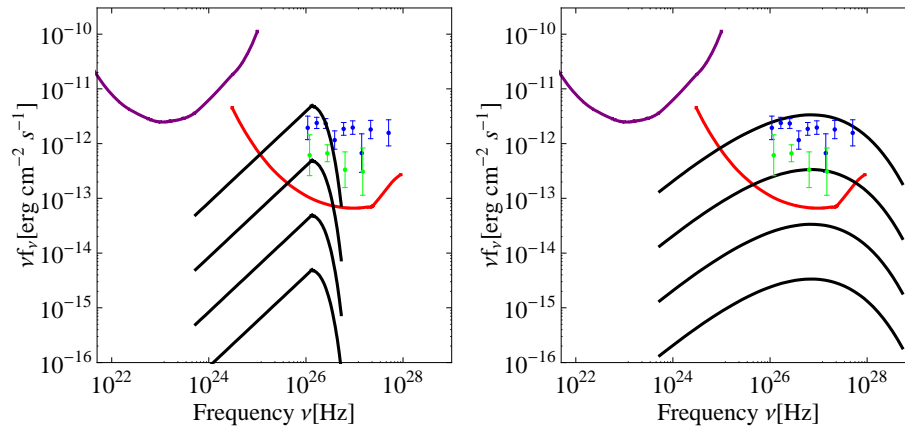


Figure 5.7: Predicted curvature emission for M87, truncated power-law particle distribution (left) and power-law with exponential cut-off (right). Black solid curves are for efficiency of power-to-luminosity conversion $\xi = 1, 0.1, 0.01, 10^{-3}$ respectively. The data points represent the spectrum as seen by the H.E.S.S. Experiment (green: 2004 data; blue: 2005 data; Aharonian et al. (2006a)). Other curves as in Fig. 5.6.

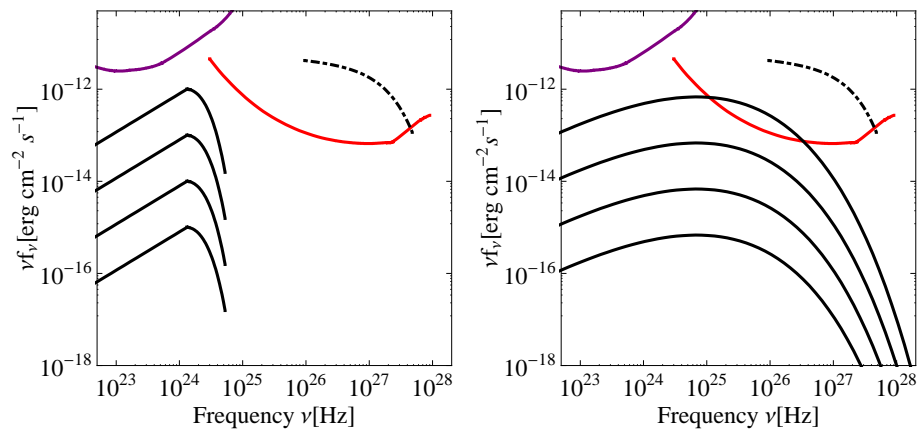


Figure 5.8: Predicted curvature emission for SgrA*, truncated power-law particle distribution (left) and power-law with exponential cut-off (right). Black solid curves are for efficiency of power-to-luminosity conversion $\xi = 1, 0.1, 0.01, 10^{-3}$ respectively. Purple solid curve is the sensitivity of the LAT instrument on board of the Fermi space telescope for 1 year integration. The red solid curve is the expected CTA sensitivity for a 5σ detection in 50 hours. The black dashed line represents the spectrum as seen by the H.E.S.S. Experiment (Aharonian et al., 2009c).

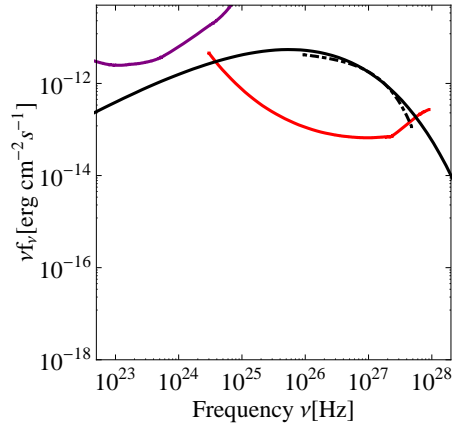


Figure 5.9: Predicted curvature emission for SgrA* for a magnetic field of $B \sim 10^4$ Gauss and an efficiency of power-to-luminosity conversion $\xi = 1$. In this case, the spectrum observed by the H.E.S.S. experiment is reproduced. Purple solid curve is the sensitivity of the LAT instrument on board of the Fermi space telescope for 1 year integration. The red solid curve is the expected CTA sensitivity for a 5σ detection in 50 hours.

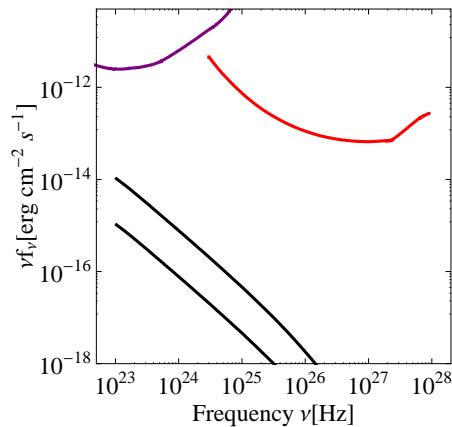


Figure 5.10: Predicted synchrotron emission for NGC 1399. Black solid curves are for efficiency of power-to-luminosity conversion $\xi = 1$ and $\xi = 0.1$ respectively. Purple solid curve is the sensitivity of the LAT instrument on board of the Fermi space telescope for 1 year integration. The red solid curve is the expected CTA sensitivity for a 5σ detection in 50 hours.

Chapter 6

Stacking Analysis of Different AGN Classes

Emission in the VHE regime is expected also from classes of AGN different from the already detected BL Lac objects and the passive nuclei that represent the main class studied in this thesis. The H.E.S.S. project did study some of these classes. The observations for some of the prototypes is presented here. Unfortunately no detection has been obtained so far. The stacking procedure presented in Chapter 4 is a powerful tool in order to study such predicted emission. In the following, a work in progress on this subject is presented. Indeed only the three cluster fields of Virgo, Coma and Fornax are used.

6.1 VHE Emission from Active Galactic Nuclei

Up to now the observation strategies for the major IACTs were strongly biased by the prejudice in favor of HBLs. Irrespective of the preference for jetted, highly beamed AGN with strong X-ray synchrotron emission, other types of AGN may conceivably emit VHE radiation as well. They have not been detected in large numbers, but they have not been searched for either. The prototypical non-HBL VHE emitter, M87, is so much weaker than many VHE detected HBL, that it would not have been detected in about 10h of observation for most of the time. Nonetheless

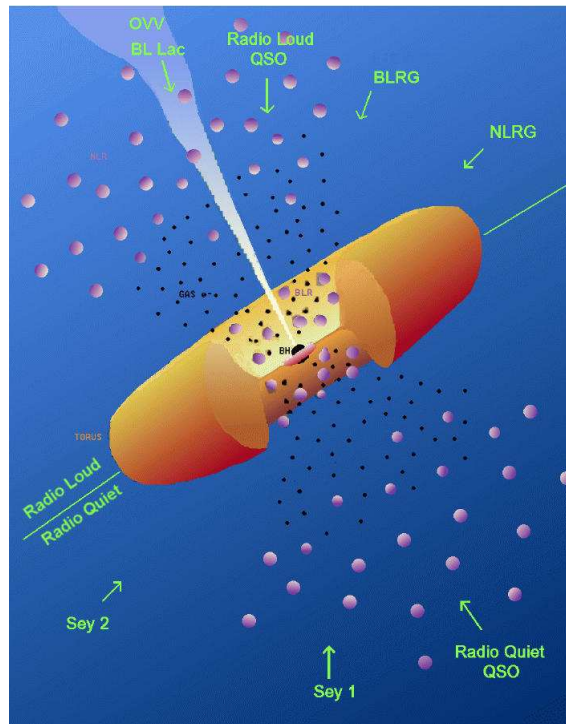


Figure 6.1: Unified model of AGN.

M87 demonstrates that AGN may also be detectable in the VHE band even if they do not present a jet aligned with the observer line of sight and even if their SEDs are not dominated by a bright synchrotron peak in the X-ray band. The jet of M87 is indeed estimated to be misaligned by $\theta \sim 30^\circ$, but from variability arguments, the VHE emission appears nonetheless highly beamed (with a Doppler factor $\delta \sim 100$, Aharonian et al. (2006a)). Also in the case of the radiogalaxy CenA, VHE emission is detected, but the current data cannot differentiate among models as to where the emission is produced (Aharonian et al., 2009a).

AGN scenarios favor VHE emission in other AGN as well. Radio jets are detected even in Seyfert 2 galaxies and they are even more prominent in classical Quasars. Apart from jets there are other efficient particle accelerators, such as the hot spots of FR II galaxies or the dense and fast outflows in AGN with high accretion rates. These winds are much more powerful than outflows in OB associations and could potentially accelerate particles to sufficiently high energies to generate VHE radiation. While some models have been studied quantitatively, most quantitative

assumptions are not known sufficiently well for models to act as guidelines.

The prototypes presented below are the brightest-closest-southernmost representatives of their class. The samples are being chosen from several public catalogs and databases and restricted to a redshift $z < 0.3$ so to remain inside the VHE horizon (cf. Section 2.4.1).

The data were reduced using the standard analysis tools and selection cuts (Aharonian et al. (2006b), standard cuts). The Reflected-Region method (Berge et al. (2007)) was used for the estimation of the background. The stacking procedure is the same described in Chapter 4.

However, due to the very different distances and powers associated to the individual objects, the study presented here can only be seen as an exploratory analysis to reveal an excess. An upper limit on the flux of each sample would not be meaningful.

6.2 Seyfert Galaxies

Seyfert galaxies owe their name to the astronomer Carl Seyfert that identified them in 1943. The main characteristic of these objects are the emission lines recognizable on top of the featureless continuum from the central source. They can be divided in two classes depending on the properties of the detected emission lines. Seyferts Type 1 (Sy1) present both broad and narrow lines, while Seyferts Type 2 (Sy2) present only narrow lines. An important characteristic of the emission lines is that among them it is possible to find also forbidden lines. These are not totally forbidden of course, but rather improbable and they are the signature of low density. This class division is due to the observation angle to the object as can be seen from Fig. 6.1.

Prototypes

Among the Seyferts galaxies visible from the southern hemisphere, the closest and brightest are the nucleus of NGC 3783 (Sy1) and NGC 1068 (Sy2). Unfortunately none of the prototypes exhibit a detectable VHE flux. Because of observational constraints, though, the Sy1 prototype was observed only for ~ 2 hours, therefore the non-detection is not a surprise. From the Sy2 prototype, it seems that ~ 200

hours more of observation would be necessary in order to reach a 5σ detection. The results of H.E.S.S. observations are presented in Table 6.1.

Source	Type	Observation Time (spent,required)	Significance σ	Threshold (Z, Ψ) GeV	UL (C.U%) $\text{cm}^{-2} \text{s}^{-1}$
NGC 1068	Sy 2	(15.15,~ 190)	1.36	270 (24.0,0.5)	2.2×10^{-12} (1.4)
NGC 3783	Sy 1	(2.21,-)	-0.83	320 (33.0,0.5)	1.9×10^{-12} (1.5)

Table 6.1: Summary of the analysis conducted on the prototypes for Seyfert Galaxies.

Stacking Analysis

Seyfert galaxies present in the field of view centered on the Virgo, Fornax and Coma cluster are selected using the SIMBAD public database (SIMBAD, 2008). From the distribution of significances of the 27 selected objects (see Fig. 6.2), it can be seen how none of the objects was detected individually and there is no hint for an excess coming from the entire sample. The significance coming from the 380 hours relative to the 19 stacked Sy1 galaxies is -1.25σ , while it amounts to -1.38σ for the 190 hours relative to 6 Sy2 galaxies (2 galaxies were identified as intermediate type and included only in the sample of the whole class).

6.3 Quasars

Quasi stellar radio sources are a subclass of AGN that exhibit a very strong non thermal emission and appear to be mostly point-like at optical wavelengths. They are usually associated with galaxies at a very high redshift. Therefore this kind of sources is not common inside the VHE horizon. From H.E.S.S. observation of the prototypical quasar 3C 273 (see Table 6.2) no detection was possible and the estimated observing time for a 5σ detection is of the order of ~ 220 hours.

Selecting from the SIMBAD database the quasars type objects in the three studied fields, the total stacked livetime amounts to ~ 250 hours (12 objects), but still

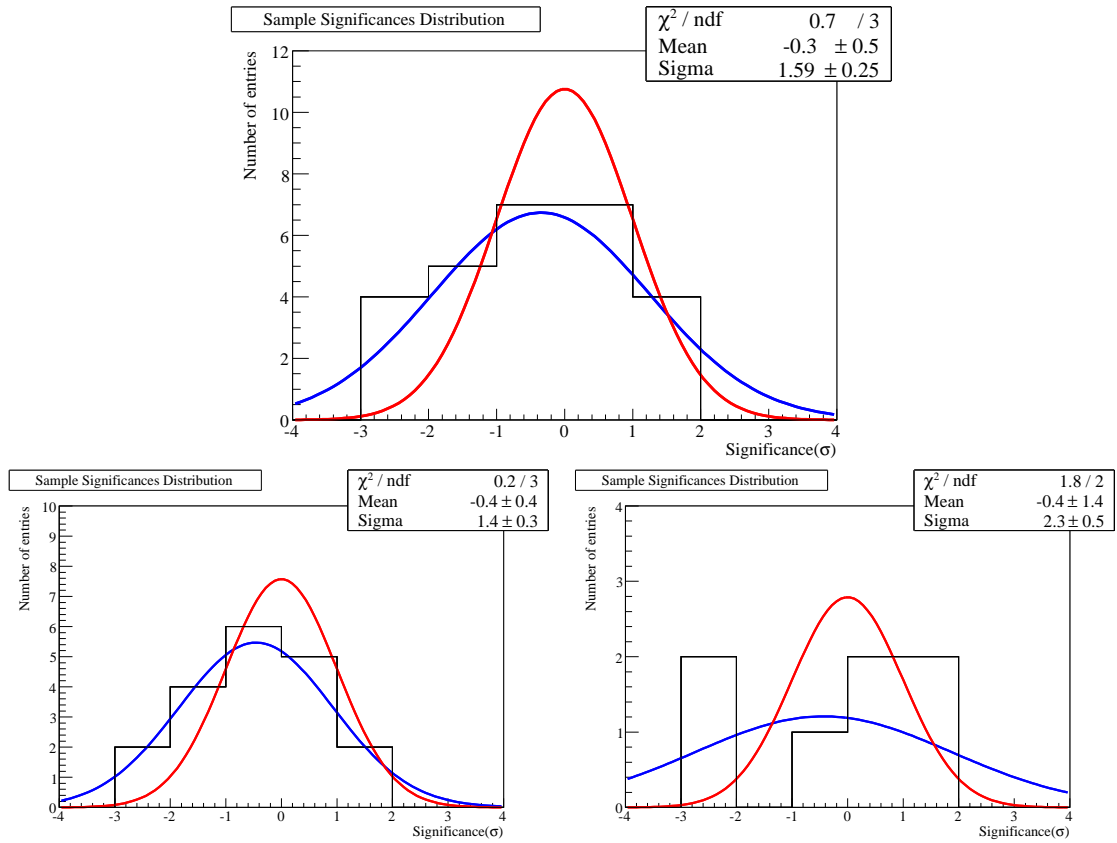


Figure 6.2: **Top:** Distribution of significances for the Seyferts sample. **Bottom left:** Seyferts type 1 subclass. **Bottom right:** Seyferts Type 2 subclass. The blue curve is a gaussian fit to the histogram, while the red curve is the expected distribution of significances for an empty field, for comparison.

Source	Type	Observation Time (spent,required)	Significance σ	Threshold (Z, Ψ) GeV	UL (C.U%) $\text{cm}^{-2} \text{s}^{-1}$
3C273	Quasar	(21.5,~ 220)	1.5	1000 (54.0,0.5)	2.6×10^{-13} (1.1)

Table 6.2: Summary of the analysis conducted on the prototype for QSO.

no sample detection is achieved with a significance of 2.53σ . From Fig. 6.3 it is possible to see how there seems to be an excess with respect to the expected empty field, but this is not significant.

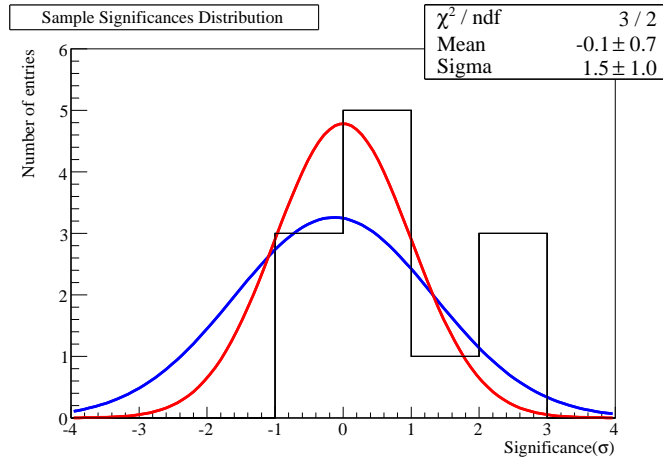


Figure 6.3: Distribution of significances for the Quasars sample. The blue curve is a gaussian fit to the histogram, while the red curve is the expected distribution of significances for an empty field, for comparison.

6.4 Faranoff-Riley Radio Galaxies

The first to present a dichotomy in radio-galaxies based both on power and morphology were Faranoff & Riley (1974). Both kinds of sources exhibit collimated radio jets. FRI galaxies are low-luminous and present the peak of radio emission close to the nucleus. FR II are more powerful, their jets have prominent bright spots and termination lobes. The distinction in power at low radio frequency (e.g. at 178 MHz) is quite sharp, with the threshold being at $P_{178\text{MHz}} \sim 2 \times 10^{25} \text{ W Hz}^{-1}$, but for increasing frequencies the two classes overlap in power. However, a distinction between FRI and FR II can be seen also from the M_R vs $P_{1.4\text{GHz}}$ plane as found by Owen & Ledlow (1994) and studied in Bicknell (1995). This division depends from $\kappa = L_{\text{nt}}/F_E$, where L_{nt} is the non-thermal luminosity of the system and F_E is the jet energy flux. An example is given in Fig. 6.5 (left).

Prototypes

H.E.S.S. observations of the prototypes 3C 120 and Pictor A led to no detection (see Table 6.4). However, one has to keep in mind that 3C120 is the second-best candidate of the class. The best candidates are the giant radio galaxies M 87 and

Cen A that were already detected by the H.E.S.S. telescopes.

Source	Type	Observation Time (spent,required)	Significance σ	Threshold (Z, Ψ) GeV	UL (C.U%) $\text{cm}^{-2} \text{s}^{-1}$
3C120	FRI	(4.95,-)	-1.77	310 (30.3,0.5)	9.0×10^{-13} (0.7)
Pic A	FR II	(18.9,~ 470)	0.98	600 (44.5,0.5)	5.2×10^{-13} (1.0)

Table 6.3: Summary of the analysis conducted on the prototype for non quasars radio-loud galaxies.

Stacking Analysis

Considering the same angular portion of the sky, radio galaxies are not very common in comparison to quasar like objects. Indeed, making a selection in the Parkes Catalog of Radio Sources (Wright & Otrupcek (1990), objects classified as ellipticals, BL Lac type objects and quasars) inside the VHE horizon, only 124 objects remain. These are plotted in Fig. 6.4, where it is possible to see that only three sources of the catalog reside in the three fields studied here. These are NGC 1399 (see Chapter 3), M 87 and M 84 (already studied in the low-accreting sample in Section 4.4). Unfortunately, the Parkes Catalog does not cover well the Coma field. Therefore, the selection of objects for the Coma field comes from the Catalog of radiogalaxies by (Miller & Owen, 2001). Selecting those radiogalaxies in the Coma field that are inside the VHE horizon, 35 galaxies are left. These objects are plotted in Fig. 6.5 (right). It is possible to see how all the objects fall below the dividing line between FRI and FR II. Among the FRI, only those with a radio luminosity $P_{1.4\text{GHz}} > 22\text{W Hz}^{-1}$ were considered as the less powerful ones are not expected to contribute much to the signal but rather hamper the background estimation. Considering this further cut, 12 objects are left corresponding to a sample livetime of 70 hours and a stacked significance of -1σ . The distribution of significance for the individual positions is given in Fig. 6.6.

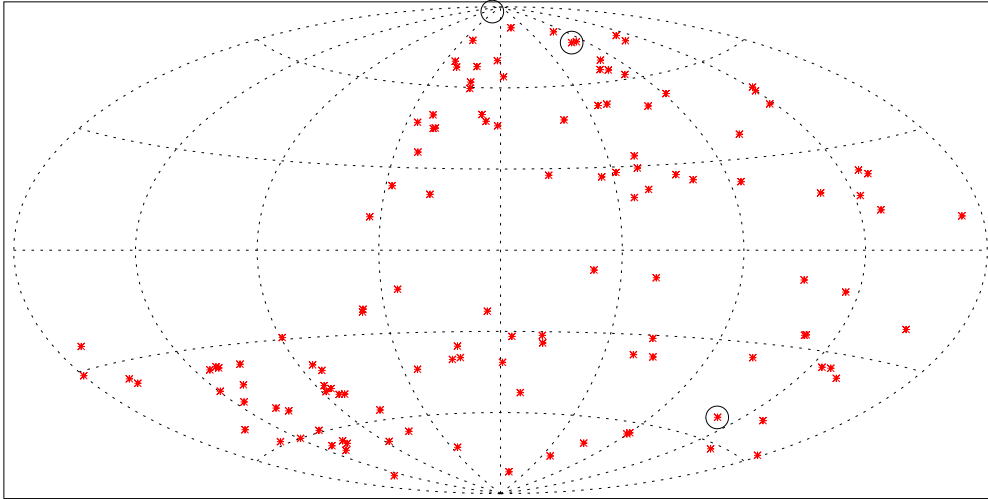


Figure 6.4: Distribution of sources in the Parkes Catalog (Wright & Otrupcek, 1990). Shown are only objects with identification equals to ellipticals, BL Lac type objects and quasars. The three circles represent the H.E.S.S. field of view centered on the clusters Virgo, Coma and Fornax.

6.5 Implications for UHECR

None of the studied sample of AGN presented an excess of VHE emission, either from the individual sources or from the stacked sample. However, one can connect this result with the expected VHE emission from a UHECR source. From the UHECR spectrum (Fig. 6.7), Katz et al. (2009) calculated the UHECR energy production rate as $J_0 \sim 7.6 \times 10^{43} \text{ erg Mpc}^{-3} \text{ yr}^{-1}$, assuming a power-law scaling of the CR production rate with redshift and energy. In order to translate this into the expected power of a single source, the density of sources n_s has to be known. From studies on the anisotropy of the UHECR sky and small scale clustering, $n_s \sim 10^{-4} \text{ Mpc}^{-3}$ (Cuoco et al., 2008). Therefore, the average power released in the form of UHECR

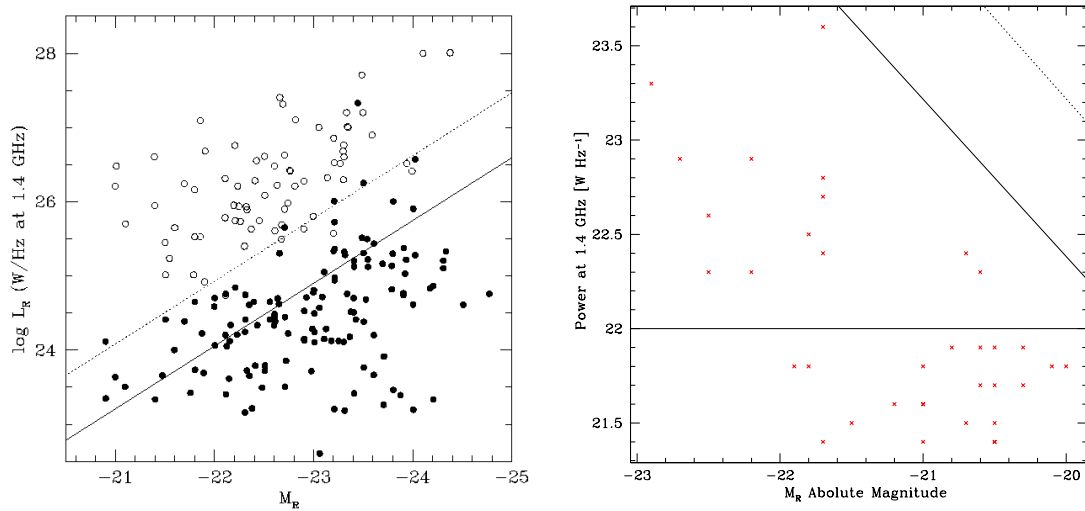


Figure 6.5: **Left:** Plotted are the data from (Owen & Ledlow, 1994) with model predictions from (Bicknell, 1995). The solid and dotted line correspond to $\kappa = 1$ and $\kappa = 0.1$ (see text). **Right:** Objects from the radio catalog by (Miller & Owen, 2001) in the Coma field. Thin lines as in left figure. Thick solid line represent the cut in luminosity adopted here.

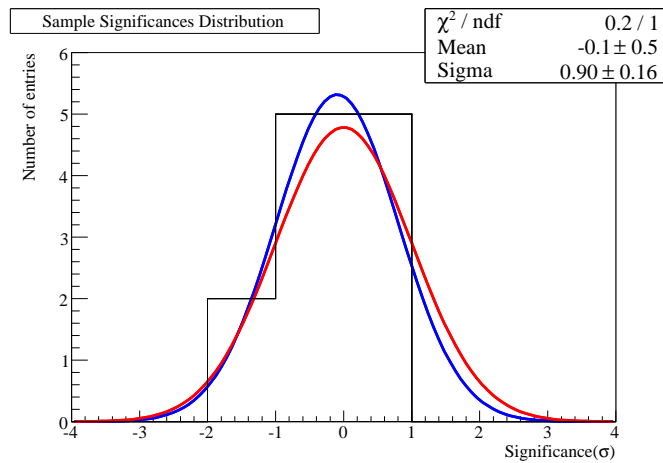


Figure 6.6: Distribution of significances for the Coma radiogalaxies sample. The blue curve is a gaussian fit to the histogram, while the red curve is the expected distribution of significances for an empty field, for comparison.

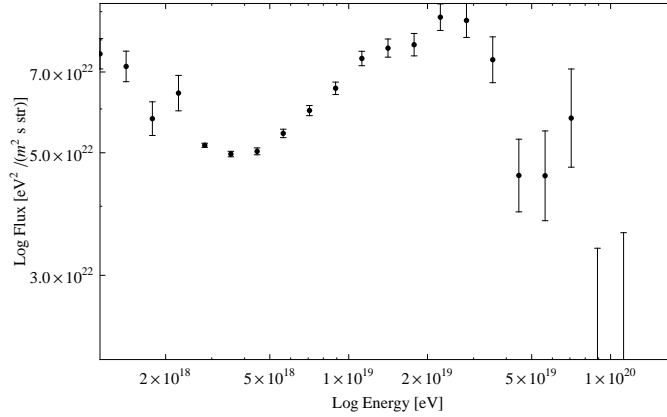


Figure 6.7: Energy spectrum of the UHECR as detected by the PAO (see Yamamoto et al. (2007)).

by a single source can be written as:

$$L_{\text{CR}} \sim 2.4 \times 10^{40} \left(\frac{n_s}{10^{-4} \text{Mpc}^{-3}} \right)^{-1} \text{erg s}^{-1}. \quad (6.1)$$

The sensitivity of the observations of individual objects presented in this chapter are of 1% percent of the Crab Nebula flux for the best exposed objects (i.e. in the Virgo field.) This correspond to

$$F_{\gamma} (0.5 - 10) \text{ TeV} \sim 1.4 \times 10^{-12} \text{erg cm}^{-2} \text{s}^{-1}, \quad (6.2)$$

enabling the H.E.S.S. system to detect an UHECR source with a γ -ray luminosity equals to the power in Eq. 6.1 out to a distance of roughly $D \sim 12$ Mpc.

None of the sources of the samples above is as close at 12 Mpc, so it is not surprising that no individual detection as been obtained, underlining the need for the stacking approach. Unfortunately, no detection arises even from the stacking approach.

Chapter 7

Outlook & Conclusions

In the previous chapters it was described how VHE emission is expected from the vicinity of SMBH. A powerful tool to study this emission is the H.E.S.S. system of telescopes, but unfortunately no detection has been obtained so far from objects that do not belong to the blazar class. Those objects are however expected to be detected from the forthcoming generation of IACTs. It is therefore interesting to explore the problems that could be studied in case a detection is obtained. For example, the lightcurve could provide us with insights on the acceleration mechanisms and the environment of the SMBH. Indeed, as particles are moving relativistically and acceleration is happening in the vicinity of the SMBH, relativistic effects on the lightcurve must be considered. In this chapter is presented a work ongoing on this subject. In addition, conclusions from the previous chapters are summarized.

7.1 Outlook: Relativistic Effects on VHE Emission from the Vicinity of SMBH

Most of the acceleration and emission processes explored in this work, happen in the close vicinity of a SMBH. Even though the forthcoming generation of IACTs might detect VHE emission from systems associated with passive SMBH, their expected angular resolution will not allow to determine the location of the acceleration region. Nevertheless, if the emission happens close to the SMBH, there will be relativistic

signatures on spectra and lightcurves because of the gravitational potential from the SMBH.

Hence, it is assumed here that the emission is arising from a blob emitting very close to the Schwarzschild radius of the black hole, whose gravity effects must be taken into consideration. Moreover, as the blob is moving at relativistic velocity, this has to be taken into account when calculating time intervals. In the following dt is the time unit in the laboratory frame (the observer) and dt' will be the one in the comoving frame of the blob. The blob is considered as point-like for the time being and it is assumed to start emitting and moving at constant velocity v at R_0 . All primed quantities refer to the reference frame comoving with the blob.

The time interval will be dilated for the blob. One time dilation comes from the special relativity Lorentz transformation, while another time dilation comes from the Shapiro delay. Therefore in the lab frame:

$$\Delta t = \frac{1}{\sqrt{1 - \left(\frac{v}{c}\right)^2}} \frac{1}{\sqrt{1 - \frac{R_S}{R}}} \Delta t' = g(t) \Delta t' \quad (7.1)$$

The function $g(t)$ is a monotonically decreasing function of time, this behavior is shown in Fig. 7.1.

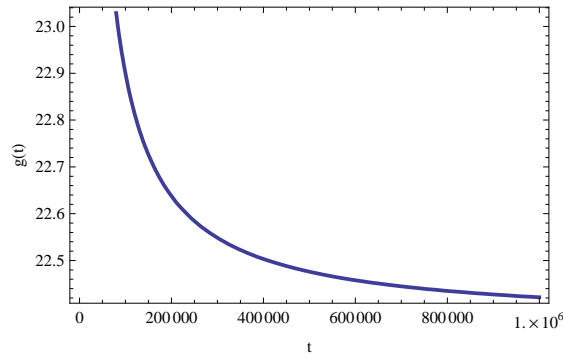


Figure 7.1: Function $g(t)$

The initial radius R_0 is chosen as the marginally bound orbit $r_{mb}(a)$ for a Kerr black hole with spin parameter $a = 0.95$, where $a = J/J_{\max}$ and $J_{\max} = GM/c$ is the maximum angular momentum per unit mass. In Fig. 7.2, the dependency of this characteristic radius to the spin parameter is shown (red curve) along with other

characteristic radii as the the marginal stable orbit, the photon sphere and the inner and outer event horizon. In the present case $r_{mb}(0.95) = 1.5R_S$.

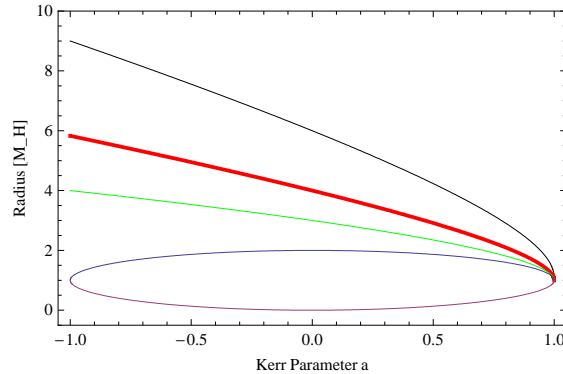


Figure 7.2: Black Hole characteristic radii. Radius definition and dependencies taken from (Camenzind, 2007). Shown are the marginal stable orbit (black), the marginally bound orbit (red), the photon sphere (green) and the inner (purple) and outer (blue) event horizon.

7.1.1 Example: Effects on Triangular Pulses

In order to explore the effect described above on lightcurves, a simplified shape for the pulse will be assumed. Indeed, here it is assumed that the pulse has a triangular and symmetrical shape defined by:

$$tr(x) = A - |x - x_s|, \quad (7.2)$$

where x_s locates the peak of the pulse and A its amplitude (an example is given in Fig. 7.3 (left)).

Following 7.1, because of relativistic effects, the pulse will now assume the function $tr(x) = A - g(x)|x - x_s|$, leading to a disruption of the symmetry of rise time t_r and decay time t_d . Indeed it can be found that $t_d > t_r$. This is easily demonstrated, because of the decreasing function $g(x)$ (see Fig. 7.1), from the fact that $tr(0) < tr(2x_s)$. The effect on a triangular pulse is shown in Fig. 7.3 (right). It has to be noted though, that in order for the effect to be visible in the plot, the time time span of the pulse had to be chosen as very long. Another effect that can be

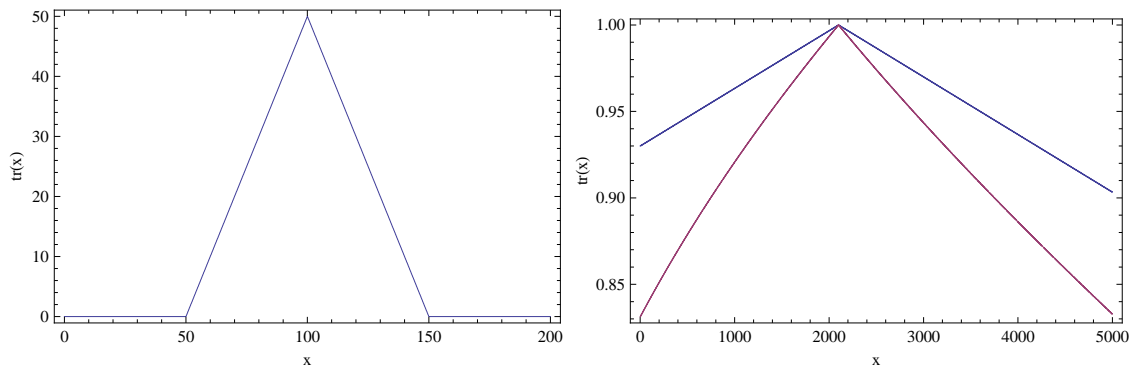


Figure 7.3: **Left:** Example of a triangular pulse with $x_s = 100$ and $A = 50$. **Right:** Example of relativistic effects on a triangular pulse. The blue curve is the emitted pulse, while the purple one is the observed pulse. Values on the axes are in arbitrary units, but both pulses have been scaled in the same amount.

recognized is the fact that both rise and decay time in the lab frame will appear shorter than in the comoving frame. This is exactly what one would expect because of Eq. 7.1. The same effect can be seen in the superposition of multiple symmetrical pulses (cf. Fig. 7.4).

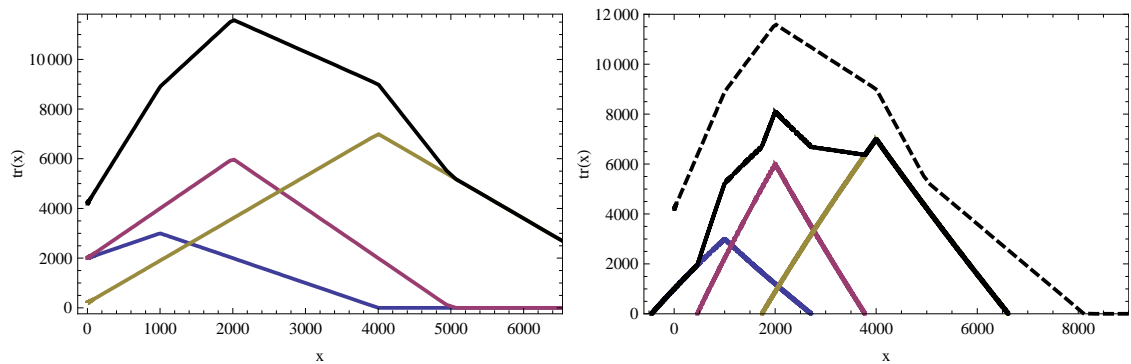


Figure 7.4: **Left:** Example of superposition of triangular pulses. In black the sum of the three individual pulses. **Right:** Observed pulses (emitted assumed to be the ones shown in the left figure). The green curve represents the superposition of the three observed pulses, while in black is overplotted the superposition of the emitted symmetrical pulses for comparison.

7.1.2 Example: PKS 2155-304

The HBL (High Peak BL Lac object) PKS 2155-304 underwent a spectacular outburst in July 2006, reaching a significance of $\sim 170\sigma$ in three runs. Thanks to this exceptional photon statistic, the H.E.S.S. collaboration could extract a minute-scale lightcurve in which is possible to recognize five bursts (see Fig. 7.5). The lightcurve of PKS 2155-304 is given in (Aharonian et al., 2007). There is stated:

“The generalized Gaussian shape from Norris et al. (1996) is used to characterize these bursts, where the burst intensity is described by:

$$I(t) = A \exp[-(|t - t_{max}|/\sigma_{r,d})^\kappa],$$

where t_{max} is the time of the bursts maximum intensity (A); σ_r and σ_d are the rise ($t < t_{max}$) and decay ($t > t_{max}$) time constants, respectively; and κ is a measure of the bursts sharpness. The rise and decay times, from half to maximum amplitude, are $\tau_{r,d} = [\ln 2]^{1/\kappa} \sigma_{r,d}$. A peak finding tool, using a Markov chain algorithm (Morhac 2000), selected five significant bursts. The corresponding positions initialized the t_{max} of a χ^2 fit of a superposition of an identical number of bursts plus a constant signal to the data, where all parameters are left free.”

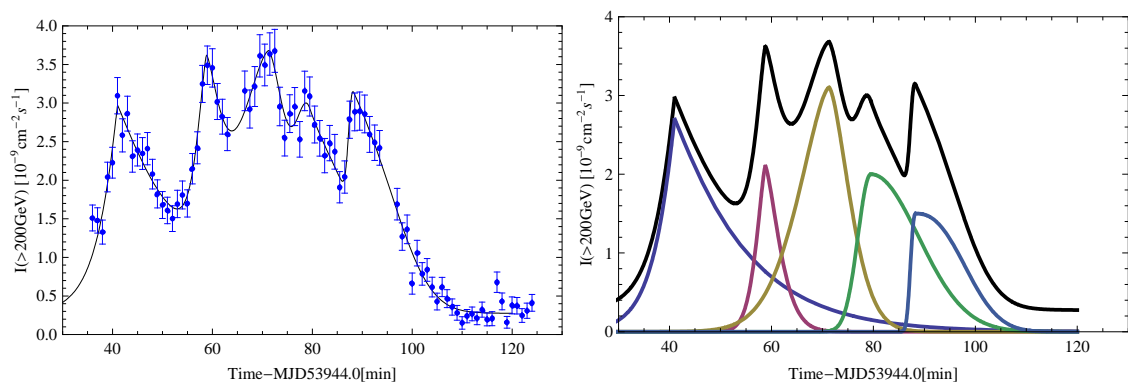


Figure 7.5: PKS 2155-304 lightcurve. **Left:** Integral flux above 200 GeV vs time. The data are binned in 1 minute intervals. Data points and curve as given in (Aharonian et al., 2007). **Right:** Decomposition of the lightcurve in five bursts from parameters in Table 7.1 and their sum (black solid curve).

t_{\max} [min]	A [$10^{-9} \text{ cm}^{-2} \text{ s}^{-1}$]	τ_r [s]	τ_d [s]	κ
41.0	2.7 ± 0.2	173 ± 28	610 ± 129	1.07 ± 0.20
58.8	2.1 ± 0.9	116 ± 53	178 ± 146	1.43 ± 0.83
71.3	3.1 ± 0.3	404 ± 219	269 ± 158	1.59 ± 0.42
79.5	2.0 ± 0.8	178 ± 55	657 ± 268	2.01 ± 0.87
88.3	1.5 ± 0.5	67 ± 44	620 ± 75	2.44 ± 0.41

Table 7.1: The results of the best χ^2 fit of the superposition of five bursts and a constant to the data shown in Figure 7.5. The constant term is $0.27 \pm 0.03 \times 10^{-9} \text{ cm}^{-2} \text{ s}^{-1}$ ($1.1 I_{\text{Crab}}$).

The analysis on the variability timescale constrains the size of the emission region down to $\sim 10^{-2} R_S$, where $R_S \sim 3 \times 10^{14} \text{ cm}$ is the Schwarzschild radius of the black hole ($M_{\text{BH}} \sim 10^9 M_\odot$) in PKS 2155-304 (Aharonian et al., 2007). One characteristic of the lightcurve of the flare is that all the bursts show a deviation from symmetry. As quantified in Table 7.1, the decay time scale in every pulse is longer than the rise time scale. This asymmetry resembles the skewing of the triangular pulse described in previous section. Therefore, the same exercise of the previous section is repeated on the functions that describe the pulses. The aim is to uncover the relativistic effects, if present. The bursts will be now described by:

$$I(t) = A \exp \left[- \left(g^{-1}(t) |t - t_{\max}| / \sigma_{r,d} \right)^\kappa \right]. \quad (7.3)$$

This will have the effect of decreasing both rise and decay time, but the decay time will be more affected (remember the decreasing behavior of $g(t)$). This goes in the direction of a more symmetrical pulse in the frame of the blob, but still the decay time will be longer than the rise time. However, when the maximum energy of the particles is constrained by the energy loss time scale, one would expect symmetrical pulses with equal rise and decay time scale. The reconstructed emitted pulses and their sum are shown in Fig. 7.6 and Fig. 7.7.

Obviously, the conclusion drawn from this study are to be viewed as a preliminary step. Indeed, this was only meant as an exploratory study on the relativistic effects

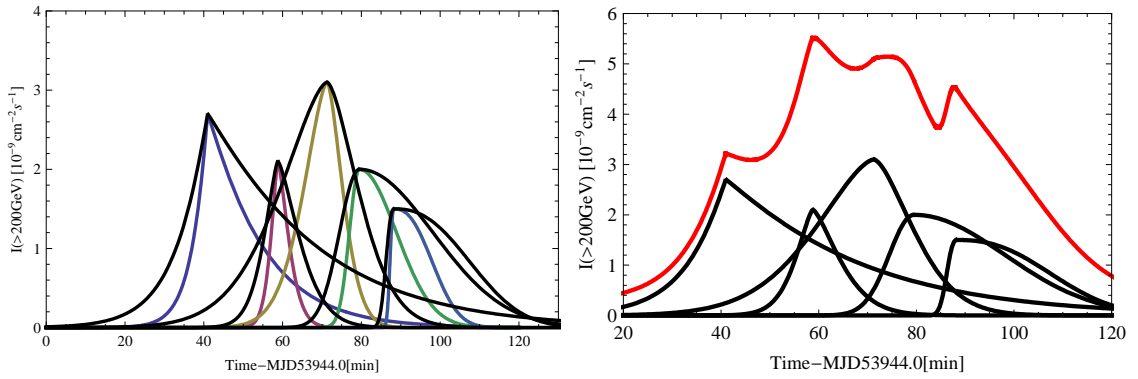


Figure 7.6: **Left:** Colored pulses as in Fig. 7.5. In black the reconstructed emitted pulse from Eq. 7.3. **Right:** Reconstructed emitted pulses and their sum (in red).

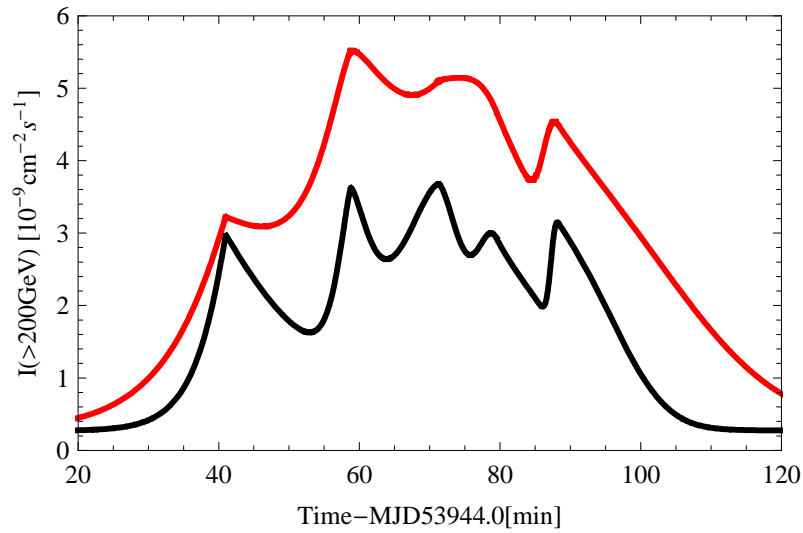


Figure 7.7: Comparison of the observed lightcurve of PKS2155-304 (in black) and the reconstructed one (in red).

on the geometry of the pulses. Moreover, the approach presented here considers either a single blob moving, or more blobs moving at the same speed. Therefore it would be interesting to study the parameter space of velocities, amplitudes and peak times.

7.2 Thesis Conclusions

In this work a search for signal in the VHE domain from passive galactic nuclei has been presented. Throughout the thesis, data obtained with the H.E.S.S. array of Cherenkov Telescopes are used.

This research is motivated by the fact that acceleration of particles up to UHE is possible in the vicinity of supermassive black holes and VHE emission is expected to be associated with those objects. Acceleration models and radiation losses in the vicinity of SMBH were summarized in Chapter 2. From simple assumptions (for details refer to Section 3.1), the VHE flux is expected to exceed the sensitivity threshold of the present generation of Cherenkov telescopes. H.E.S.S. is the most sensitive of the present generation of Cherenkov telescopes (for details see Chapter 1). The main focus of observations is on a class of galactic nuclei that are underluminous at low photon energies. The underluminosity facilitates the produced VHE emission to escape the source without being absorbed by internal photon fields.

In order to search for VHE emission, observations of the nearby giant elliptical galaxy NGC 1399 were conducted with the H.E.S.S. array. No detection arises from the ~ 20 hours of collected data, but it was nonetheless possible to derive constraints on the strength of the magnetic field in the vicinity of the SMBH and on the maximum energy that the accelerated particles can reach. Assuming that the SMBH of $M_{\text{BH}} = 10^9 M_{\odot}$ in NGC 1399 is maximally spinning and that the power from the potential drop supplied by the black hole can be converted in VHE luminosity, a limit on the magnetic field, $B < 74$ Gauss, can be obtained. This is the tightest empirical constraint on the strength of the magnetic field of a SMBH. These results were presented in Chapter 3.

Because of the non-detection of the best candidate NGC 1399, another analysis approach has to be used. The sensitivity of the H.E.S.S. array scales with the square of the observational time, therefore a substantial increment in the observational lifetime would be required in order to probe lower fluxes. This is not easily achievable with the current generation of Cherenkov Telescopes. In order to fulfill the time requirement, data already obtained with the H.E.S.S. telescopes in the framework

of other projects were used.

The H.E.S.S. array observed the central field of the Virgo cluster in order to study the VHE emission from the giant radiogalaxy M87. In addition, also the central region of the Coma cluster was observed with the H.E.S.S. array in order to investigate VHE emission from cluster cores. Both the Virgo cluster and the Coma cluster are rich in large ellipticals that are commonly believed to host SMBH. Therefore a stacking analysis was pursued exploiting the data collected in these two fields along with the data collected on the Fornax cluster (in the framework of observations of NGC 1399). Objects similar to NGC 1399 were selected in the three clusters and the signal from their position was stacked. Unfortunately no detection was obtained by means of the stacking approach, leading to an upper limit on the flux of the stacked sample. This results in an upper limit on the luminosity of the typical object, $L_\gamma \sim 1.41 \times 10^{41} (D/50\text{Mpc})^2 \text{ erg s}^{-1}$. These results were presented in Chapter 4.

The same three cluster fields were analyzed in order to search for VHE emission from different classes of AGN. Indeed, in several type of AGN efficient particle acceleration regions are present, such as relativistic jets and their hot spots. Unfortunately this search led to no detection. It has to be noted that the samples in each class are not extensive, as the analysis has been focusing only on an average of 15 objects for each sample. Therefore this has to be regarded to as a preliminary search. The data are presented in Chapter 6.

With the stacking analysis on passive galactic nuclei being unsuccessful in detecting a VHE signal, it is interesting to see what one can expect from the observational facilities of next generation. In Chapter 5 a detailed modeling of the expected flux and spectrum of the emission was carried out. The aim was to check the behavior of the emission in the case of realistic particle distributions. It is shown that in the case of curvature losses dominating, the expected signal is close to the sensitivity threshold of the forthcoming CTA observatory.

It is interesting to see which kind of investigations one might carry out, if a detection is obtained. The angular resolution of Cherenkov telescopes cannot resolve the emitting region. Indeed, for most of the extragalactic VHE sources one can

derive the extension of the VHE emitting region from variability arguments, but not its location. If the emitting region is located in the vicinity of the SMBH, the best way to prove this is to detect a signature of relativistic effects due to the SMBH gravitational potential. A simple analysis of the geometrical effects on pulse shape is presented in Section 7.1.

Although no new class of VHE emitters was established by the research presented in this thesis, important constraints on the physical parameters of the investigated sources could already be obtained. Moreover, the detailed predictions given in Chapter 5 are promising for the detection of passive SMBH with the forthcoming generation of Cherenkov arrays (e.g. CTA).

Bibliography

- Abdo, A. A. et al. 2009, *Astrophys.J.Suppl*, 183, 46
- Abraham, J. et al. (Pierre Auger Collaboration) 2007a, *Science* 318, 938
- Abraham, J. et al. (Pierre Auger Collaboration) 2007b, *Astroparticle Physics* 29, 188
- Aharonian, F. 2004, *Very High Energy Cosmic Gamma Radiation*, World Scientific Publishing
- Aharonian, F. 2000, *New Astronomy*, 5, 377
- Aharonian, F. et al. 2002, *Phys Rev D*, 66b, 3005
- Aharonian, F. et al. (H.E.S.S. Collaboration) 2006a, *Science*, 314, 1424
- Aharonian, F. et al. (H.E.S.S. Collaboration) 2006b, *A&A*, 457, 899
- Aharonian, F. et al. (H.E.S.S. Collaboration) 2006c, *Nature*, 440, 1018
- Aharonian, F. et al. (H.E.S.S. Collaboration) 2007, *ApJ*, 664L, 71A
- Aharonian, F. et al. (H.E.S.S. Collaboration) 2009a, *ApJL*, 695, L40-L44
- Aharonian, F. et al. (H.E.S.S. Collaboration) 2009b, *Astron. Astrophys.* 495, 27-35
- Aharonian, F. et al. (H.E.S.S. Collaboration) 2009c, arXiv:0906.1247v1, *A&A* in press
- Aharonian, F. et al. (H.E.S.S. Collaboration) 2009d, arXiv0907.0727T, *A&A* in press

Albert, J. et al. 2008, *Science*, 320, 1752

Aliu, E. et al. (MAGIC Collaboration) 2009, *ApJ*, 692L, 29A

Allen, S. W. et al 2006, *MNRAS*, 372, 21A

Atoyan, A. M. & Nahapetian, A. 1989, *A&A*, 219, 53A

Behera, B. & Wagner, S. 2009, 31st ICRC Proceedings

Berezinsky, V. et al 1994, *Phys. Letter B*, 325, 136

Berezinskii, V.S., Bulanov, S.V., Dogiel, V.A., Ptuskin, V.S., 1990, *Astrophysics of Cosmic Rays*, ed. V. L. Ginzburg (Amsterdam: North-Holland)

Berge, D. 2006, PhD Thesis

Berge, D. et al. 2007, *A&A*, 466, 1219

Bernlöhr, K. 2008, AIPC, 1085, 874B

Bicknell, G. V. 1995, *ApJS*, 101, 29B

Bicknell, G. V. et al 1997, *ApJ*, 485, 112B

Bicknell, G. V. & Li, J. 2007, *Ap&SS*, 311, 275

Binggeli, B. et al. 1985, *AJ*, 90, 1681B

Blumenthal, G. R. & Gould, R. J. 1970, *Rev. Mod. Phys*, 42, 237

Boldt, E. & Gosh, P. 1999, *MNRAS*, 307, 491

Cacciato, M. et al, 2009, *MNRAS*, 394, 929C

Camenzind, M. 2007, *Compact objects in astrophysics* (Springer)

Cillis, A. N. et al. 2004, *ApJ*, 601, 142

Cuoco, A. et al. 2008arXiv0809.4003C

Dole, H. et al. 2006, A&A, 451, 417

Erber, T. 1966, Rev Mod Phys, 38, 626

Faranoff, B. L. & Riley, J. M., 1974, MNRAS, 167P, 31F

Feldman, G. J. & Cousins, R. D. 1998, Phys. Rev. D, 57, 3873

Ferguson, H. C. 1989, AJ,98, 367

Ferrarese, L. & Merritt, D. 2000, ApJ, 539, L9

Gebhardt, K. et al. 2000, ApJ, 539, L13

Gebhardt, K. & Thomas, J. 2009, arXiv:0906.1492v1

Goldreich, P. & Julian, W. H. 1969, ApJ, 157, 869

Hardcastle, M. J. 2009, MNRAS, 393, 1041H

Hess, V. 1912 Phys.Zeitschr. 13, 1084

Hillas, A. M. 1984,ARA&A, 22, 425H

Hillas, A. m. 1985 in International Cosmic Ray Conference, vol. 3, 445

Hirose, S. et al. 2004, ApJ, 606, 1083

Hirovani, K. & Okamoto, I. 1998, ApJ, 497, 563H

Houghton, R. C. W. et al. 2006, MNRAS, 367, 2

Istomin, Y. N. & Sol, H. 2009, Ap&SS, 321, 57I

Kafatos, M. & Leiter, D. 1979, ApJ, 229, 46

Katz, B., Budnik, R. & Waxman, E. 2009, JCAP, 03, 020

Killeen, N. E. B. 1988, ApJ, 325, 180K

Killeen, N. E. B. & Bicknell, G. 1988, ApJ, 325, 165K

Kormendy, J. 2009, ApJS, 182, 216K

Kuncic, Z. & Bicknell, G. 2004, ApJ, 616, 669

Levinson, A. 2000, Phys. Rev. Let., 85, 912

Li & Ma 1983, ApJ, 272, 317

Loewenstein, M. et al. 2001, ApJ, 555, L21

Magorrian, J. et al. 1998, AJ, 115, 2285

Mastichiadis, A. & Protheroe, R. J. 1990, MNRAS, 246, 279

Merrit, D. & Ferrarese, L. 2001, MNRAS, 320, 30

Miller, N. A. & Owen, F. N. 2001, ApJS, 134, 355M

Mücke, A. & Protheroe, R. J. 2001, APh, 15, 121

Nandra, K. et al. 2002, ApJ, 576, 625

Neronov, A., Semikoz, D. & Tkachev, I., arXiv:0712.1737

Neronov, A. & Aharonian, F. 2007, ApJ, 671, 85

Neronov, A. et al. 2004, J. Exp. Theor. Phys., 100, 656

Nolan, S. et al. 2008, ICRC....3.1009N

O'Connell, R. W. et al. 2005, ApJ, 635, 305

Owen, F. N., & Ledlow, M. J. 1994, in ASP Conf. Ser. 54, The Physics of Active Galaxies, ed. G. V. Bicknell, M. A. Dopita & P. J. Quinn (San Francisco: ASP)

Padmanabhan, T. 2001 Theoretical Astrophysics, Volume II (Cambridge University Press)

Paolillo, M. et al. 2002, ApJ, 565, 883

Pellegrini, S. 2005, ApJ, 624, 155

- Pierini, D. et al. 2002, MNRAS, 332, 422P
- Rees, M. J. 1984, ARA&A, 22, 471
- Richstone, D. et al. 1998, Nature, 395, A14
- Rieger, F. M. & Mannheim, K. 2000, A&A, 353, 473
- Rieger, F. M. & Aharonian, F. A. 2008, A&A, 479, L5
- Rowell, G. P. 2003, A&A, 410, 389R
- Rybicki, G. B. & Lightman, A. P. 1979, Radiative Process in Astrophysics (John Wiley & Sons)
- Sadler, E. M. et al. 1989, MNRAS, 240, 591
- Schlickeiser, R. 2002, Cosmic Ray Astrophysics, Springer
- Schlickeiser, R. 1996, A&AS, 120C, 481S
- Schneider, D. P. 2007 AJ, 134, 102S
- Shurkin, K. et al. 2008, MNRAS, 383, 923
- Sikora, M. et al. 1987, ApJ, 320, 81
- SIMBAD, Centre de Donnes astronomiques de Strasbourg
- Skrutskie, M. F. et al 2006, AJ, 131, 1163S
- Slane, P. & Wagh, S. M. 1990, ApJ, 364, 198
- Stawarz, L. & Kirk, J. G. 2007, ApJ, 661, L17
- Swordy, S. P. 2001, Space Science Review, 99, 85
- Temi, P. et al. 2005, ApJ, 622, 235
- Thorne, K. S., Price R. H. & Macdonald, D. A. 1986, Black Holes: The Membrane Paradigm (New Haven: Yale University Press)

Veron-Cetty, M. P. & Veron, P. 1996, ESOSR, 17, 1V

Veron-Cetty, M. P. & Veron, P. 2006, A&A, 455, 773

Volonteri, M. et al. 2007, ApJ, 667, 704

White, R. L. et al. 2007, ApJ, 654, 99

Wright, A. & Otrupcek, R. 1990, PKS C 0W

Yamamoto, T. et al., 2007 ICRC07

http://www.auger.org/technical_info/pdfs/icrc2007/0707.2638v1.pdf

Acknowledgments

First of all I want to thank my supervisor Prof. Stefan Wagner. Much of what I have learned in these years is thanks to his patience and to the lengthy discussions he always found the time for. And especially thanks for pushing me to always ask despite my shyness.

Thanks to Prof. John Kirk and to Prof. Max Camenzind for being in my IMPRS committee and always providing helpful insights during our meetings. Thanks to Prof. Kirk also for accepting to be the second referee for my thesis.

Thanks to Prof. Geoff Bicknell that helped me to gather a better understanding of galactic nuclei when he visited here at the LSW and when I visited Mount Stromlo Observatory (thanks for having me there!).

Thanks to Prof. Matthias Bartelmann for agreeing to take part in my exam.

Thanks to Priv.D. Christian Fendt for all the energy he puts into IMPRS issues. I acknowledge support from the International Max Planck Research School (IMPRS) for Astronomy & Cosmic Physics at the University of Heidelberg.

Thanks to all the people that helped me throughout this long journey. Let's start with people in my "*work-life*". Thanks to the past and present HESS people. Especially a big thanks to all my group colleagues: Steffie and Thomas, it was very nice sharing the office with you; Marcus, Bagmeet, Dimitrios, Gerd, Sarah, Matthias and also the "newbie" Eva. Thanks you all for creating such a nice atmosphere and for helping me out with technical/scientific/burocratic problems. Thanks to all the people at the LSW.

Thanks to the LifeSocks&Co. for making my life here so colorful. Cla, really, thanks! I think about you as my big sister now. You always gave me support, a

shoulder to cry on and a cow to eat (meaning the ice cream of course). Giu! you accepted me as a friend from the moment I arrived and you enriched my life here. Heidelberg is not the same without you girls, but luckily the tons of mails do their job. Thanks to Isabel: I am so lucky to call you friend, because you value friendship so much. Thanks to Viviana that is always super busy, but always finds time for me. We'll go to Berlin sooner or later! Thanks to Matteo for his being always always so nice and for being always at ease in every situation. Thanks to Vivì and Olga for the girls-night and for sharing so much. Thanks to all the people that in these years made it worth getting out of the couch every once in while (and you know how lazy I am!): Brian, Massimo, Baybars (Barabba), Giovanni, Ale, Sara, Jamie . . . and many more! My lovely flatmates! Thanks to Gisella for being one of the sweetest person I ever met and make me feel so good when I am at home (and outside!) and thanks to Teresa for standing my geekiness and lazyness. Thanks to my dear friend Farid for everything I've learned of myself through you. Thanks to Marcello and Ros, for always having a smile for me and thanks to Chris that always finds a flattering word to improve my mood. Thanks to Lisa that managed to make my stay in Namibia really nice (I am not at my best there . . .). Thanks to Bagmeet for being such a nice colleague, but also a friend that can stand me during conferences, and thanks for bringing Swapna in our lives too. Thanks guys for all the travels we shared. Thanks to all the IMPRS of all sizes and ages (old, new, mini, micro, the ghost ones . . .). I could try to list all the people I have met in Heidelberg in these 3++ years, but I'll end up forgetting many. I just want to say that somehow all of you helped me in being happy here.

Thanks to all my friends back in Italy for being my safe shelter. It's really good to know that every time I go back I will see so many friendly faces. Especially my lovely "astronze": Laura, source of endless energy, Nico that didn't forget me even though I write so little, and all the other ladies.

Finally a big thanks to my family. Mamma e babbo, mio fratello Germano e la sua Monia. Che dire? Mi avete sempre lasciato fare quello che più mi aggrada, fidandovi di me senza riserve. E in questi tre anni mi avete coccolato senza fine ogni volta che mettevo piede a casa. Dai, diciamo che un po' me lo merito ;), però grazie un bel po'!!!!